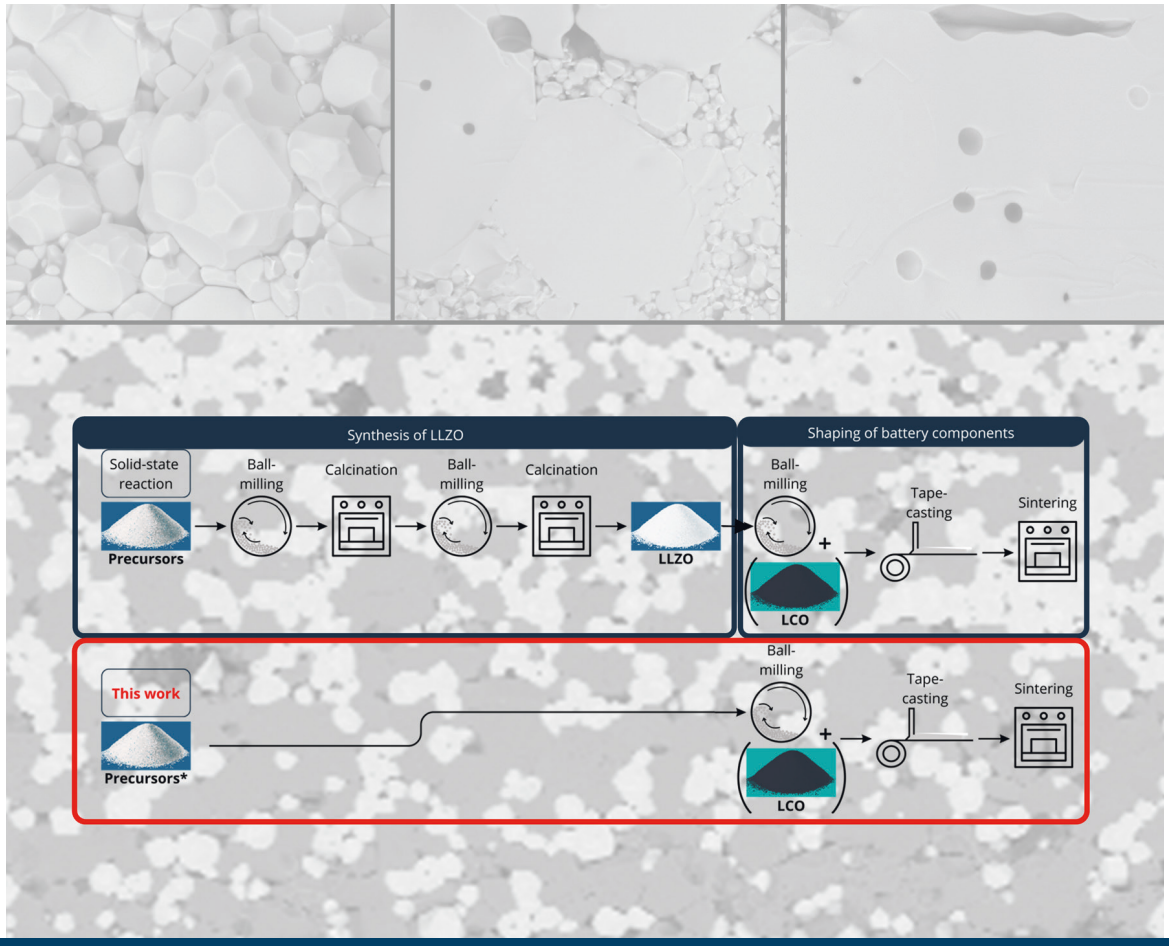

Oxide-based All-Solid-State Batteries for and from Recycling Processes

Vivien Mirjam Kiyek

Energie & Umwelt / Energy & Environment
Band / Volume 656
ISBN 978-3-95806-806-3

Mitglied der Helmholtz-Gemeinschaft

JÜLICH
Forschungszentrum

Schriften des Forschungszentrums Jülich
Reihe Energie & Umwelt / Energy & Environment Band / Volume 656

Forschungszentrum Jülich GmbH
Institute of Energy Materials and Devices (IMD)
Werkstoffsynthese und Herstellungsverfahren (IMD-2)

Oxide-based All-Solid-State Batteries for and from Recycling Processes

Vivien Mirjam Kiyek

Schriften des Forschungszentrums Jülich
Reihe Energie & Umwelt / Energy & Environment Band / Volume 656

ISSN 1866-1793 ISBN 978-3-95806-806-3

Bibliografische Information der Deutschen Nationalbibliothek.
Die Deutsche Nationalbibliothek verzeichnet diese Publikation in der
Deutschen Nationalbibliografie; detaillierte Bibliografische Daten
sind im Internet über http://dnb.d-nb.de abrufbar.

Herausgeber und Vertrieb:	Forschungszentrum Jülich GmbH Zentralbibliothek, Verlag 52425 Jülich Tel.: +49 2461 61-5368 Fax: +49 2461 61-6103 zb-publikation@fz-juelich.de www.fz-juelich.de/zb
Umschlaggestaltung:	Grafische Medien, Forschungszentrum Jülich GmbH
Druck:	Grafische Medien, Forschungszentrum Jülich GmbH
Copyright:	Forschungszentrum Jülich 2025

Schriften des Forschungszentrums Jülich
Reihe Energie & Umwelt / Energy & Environment, Band / Volume 656

D 82 (Diss. RWTH Aachen University, 2024)

ISSN 1866-1793
ISBN 978-3-95806-806-3

Vollständig frei verfügbar über das Publikationsportal des Forschungszentrums Jülich (JuSER)
unter www.fz-juelich.de/zb/openaccess.

Abstract

All-Solid-State Batteries (ASSB) are considered to be one of the most promising future battery technologies due to the prospect of increased safety and energy density. ASSB can be categorized into three main classes: Polymers, Sulfides and Oxides, which are the focus of this work. Ceramic oxides, among others, are suitable to replace current liquid electrolytes of Lithium-ion batteries (LIBs), with the advantage of being the only solid electrolyte ($Li_7La_3Zr_2O_{12}$, LLZO) that is stable to Li metal. Li metal as an anode material provides a higher energy density in the battery and can overcome the foreseeable limits of liquid electrolytes. In addition, ceramic oxide solid electrolytes increase safety due to the high thermal stability of ceramic materials. Disadvantages of LLZO are the high processing cost and energy requirements, leading to high embodied energy due to the multiple long calcination times at high temperatures. Also, LLZO production requires raw materials beyond Li, Co, Ni and Mn, which are well-known from the cathode materials in LIBs. Notably, Ta, and Ga are listed as critical raw materials. This is one of the main reasons why recycling is important for both current LIBs and future ASSB batteries. The current EU directive requires a recycling rate of 70% of complete batteries in 2030, while individual materials such as Co, Ni, should have recycling rates of up to 90%. In the present work, a cost- and energy-efficient direct recycling route for LLZO components is developed via re-lithiation of LLZO waste materials by adding a Li source during heat treatment. Abnormal grain growth as a possible result of sintering LLZO tapes under Li excess is analyzed, and the responsible mechanism is investigated and explained. It is demonstrated successfully that sintering with Li_2CO_3 is able to re-lithiate degraded LLZO: Similar behavior to freshly synthesized LLZO separator material is observed, while the critical current density (CCD) is even increased to 0.75 mA cm^{-2}, exceeding the recently reported values for tapes made from freshly synthesized LLZO powder in a comparable process. This re-lithiation route therefore represents the first successful approach to a direct recycling of LLZO components, able to save time and cost as well as to preserve the embodied energy in the LLZO.

The second part of the thesis addresses the high process cost and energy consumption of LLZO synthesis. Here, a new process route is developed, where tape casting of precursors powder of LLZO leads to the formation of LLZO *in-situ* during the sintering step. The application of this process onto both the separator and the composite cathode, a special designed cathode for example for oxide-solid-state batteries, is then evaluated. The composite cathode with LCO-LLZO shows highly promising behavior as the Co-ion diffusion, a disadvantage of co-sintering of already pre-synthesized LLZO powder mixtures, that is very hard to avoid, is suppressed in this new process. Although Al-ion diffusion still occurs, the general properties of the composite cathodes, such as density and flatness are very promising. For the LLZO separator, Ta doping and Ga doping with the new process route were investigated. Both result in a low-density tape, however, density can be tuned by adding pre-synthesized LLZO particles to the slurry. These findings can hence be used as well to create a porous-dense-porous

LLZO layer with the new process, as the porous LLZO framework represents an interesting approach for zero-strain electrode layers. Finally, a recycled precursor material is used in the new process, which shows first good results for an LLZO separator tape. This suggests that the new process is applicable also for recycled raw material, although further process fine-tuning is required. As a result, the overall process time is reduced by 65%, while individual steps are reduced by more than 98%. This translates into a reduction of the overall throughput time from 40 hours oven time at the highest temperature (with sintering 45 hours (LLZO) or 42 hours (LCO-LLZO)) to only 5 hours (LLZO) or 2 hours (LCO-LLZO) at the highest temperature, a significant advantage for industrial upscaling. Also, energy input is considerably reduced as the majority of the energy-intensive heat treatment steps are saved (80%). This reduction in time and energy demand ultimately reduces the production cost of LLZO.

Kurzfassung

Festkörperbatterien gehören zu den vielversprechendsten zukünftigen Batterietechnologien, da sie im Vergleich zu anderen Technologien eine höhere Sicherheit und Energiedichte aufweisen. Festkörperbatterien können in drei Kategorien unterteilt werden: Polymere, Sulfide und Oxide, wobei die vorliegende Arbeit auf letztere fokussiert. Keramische Oxide eignen sich insbesondere, um den Flüssigelektrolyten aus Lithium-Ionen-Sekundärbatterien (LIBs) zu ersetzen. Ein Vorteil davon ist, dass $Li_7La_3Zr_2O_{12}$ (LLZO) als einziger Festelektrolyt gegenüber Lithium-Metall stabil ist. Ein Einsatz von Li-Metall mit einer höheren Energiedichte als Anode ermöglicht eine Substitution Li-Ionen-Sekundärbatterien, die absehbar an ihre Grenzen kommen werden. Zudem weisen keramische, oxidische Festelektrolyte eine hohe thermische Stabilität auf, wodurch die Sicherheit der Batterie erhöht wird. Allerdings sind LLZO mit hohen Prozesskosten und einem hohen Energieverbrauch durch mehrere, lange Kalzinierschritte bei hohen Temperaturen verbunden. Des Weiteren erfordert die Produktion von LLZO die Verwendung zusätzlicher Rohmaterialien über die Materialien Li, Co, Ni und Mn hinaus, die bereits durch ihren Einsatz in Kathoden in LIBs bekannt sind. Zusätzlich werden Ta und Ga als kritische Rohmaterialien eingestuft. Dies ist einer der Hauptgründe, sich mit Recycling zu beschäftigen, sowohl für LIBs als auch für Festkörperbatterien. Die aktuellen Richtlinien der EU besagen, dass Batterien bis zum Jahr 2030 zu mindestens 70 % recycelt werden sollen, während einzelne Materialien wie Co und Ni Recyclingraten von 90 % aufweisen müssen. Im Rahmen dieser Arbeit wurde deshalb eine kosten- und energieeffiziente direkte Recyclingroute für LLZO-Batteriekomponenten entwickelt. Hierbei wurde LLZO-Prozessabfall durch einen Lithiierungsschritt, der während des Sinterns zusammen mit einer Li-Quelle erfolgt, recycelt. Anormales Kornwachstum kann während des Sinterns von LLZO-Folien durch die zusätzliche Li-Quelle auftreten. Der zugrundeliegende Mechanismus wurde in diesem Zusammenhang analysiert und beschrieben. Des Weiteren konnte erfolgreich demonstriert werden, dass die Zugabe von Li_2CO_3 während des Sinterns ein Re-lithiieren von LLZO ermöglicht. Die LLZO-Separator-Folien aus recyceltem Material wiesen ein ähnliches Verhalten auf wie die Folien aus frisch synthetisiertem LLZO, wobei eine kritische Stromdichte (engl. critical current density CCD) von 0,75 mA cm^{-2} festgestellt wurde, die sogar höher ist als die veröffentlichten Werte aus frisch synthetisiertem LLZO-Pulver und einem ähnlichen Prozess. Der Re-Lithierungsprozess stellt eine erfolgreiche Methode dar für das direkte Recycling von LLZO-Batteriekomponenten, wodurch Zeit und Kosten eingespart werden können. Zudem geht die gespeicherte Energie in LLZO nicht verloren.

Der zweite Teil der Arbeit befasst sich mit den hohen Prozesskosten und dem hohen Energieverbrauch der LLZO-Synthese. Ein neuer Prozess wurde entwickelt, in dem Edukte in Pulverform im Folienguss genutzt werden, um danach während des Sinterns *in-situ* LLZO herzustellen. Der Prozess wird sowohl in Separatoren als auch in Kompositkathoden getestet, eine spezielle Art Kathode für Oxid-Festkörperbatterien. Im Rahmen des Prozesses wird die Co-Ionen-Diffusion in LCO-LLZO

Kompositkathoden erfolgreich unterdrückt, welche sonst einen großen Nachteil für zusammen gesinterte Kompositkathoden aus fertig synthetisiertem LLZO-Pulver darstellt. Dennoch lässt sich eine Al-Ionen-Diffusion beobachten, andere Eigenschaften der Kompositkathode wie Dichte und Flachheit der Folie überzeugen jedoch. Im Rahmen des neuen Prozesses wurden Untersuchungen zu Ta- und Ga-Dotierungen bei LLZO-Separatoren durchgeführt. Beide Dotierungen resultieren in Folien mit geringer Dichte, wobei eine Beeinflussung der Dichte durch vor-synthetisierte LLZO-Partikel möglich ist. Die Resultate legen nahe, dass auch porös-dicht-poröse LLZO-Folien mit dem neuen Prozess hergestellt werden können, wobei das poröse LLZO-Gerüst ein vielversprechendes Ergebnis zur Vermeidung von internen Spannungen in Elektrodenschichten sein könnte. Schließlich werden auch recycelte Edukte im neuen Prozess eingesetzt, die erste vielversprechende Ergebnisse für LLZO-Folien zeigen. Der neue Prozess ist demnach auch für recyceltes Material anwendbar, wobei jedoch noch eine Optimierung erforderlich ist. Ein Ergebnis aus dem neuen Prozess ist eine eingesparte Prozesszeit von 65 %, während einzelne Schritte sogar 98 % Zeit einsparen. Dies impliziert eine Reduktion der Ofenzeit bei Hochtemperatur-Prozesschritte (inklusive Sintern) von 45 Stunden (LLZO) bzw. 42 Stunden (LCO-LLZO) auf 5 Stunden (LLZO) bzw. 2 Stunden (LCO-LLZO) und stellt einen signifikanten Vorteil für Industrien dar. Infolgedessen wird auch der Energieverbrauch erheblich reduziert, da der Großteil (80%) der energieintensiven Hochtemperaturschritte eingespart wird. Letztendlich führt diese Reduktion von Zeit und Energieaufwand zu einer Reduktion der Herstellungskosten von LLZO.

Content

List of abbreviations

ASSB	–	All-Solid-State Batteries
BSE	–	Back-Scattered Electrons
CCD	–	Critical Current Density
DFT	–	Density Functional Theory
EBSD	–	Electron Backscatter Diffraction
EDX	–	Energy-Dispersive X-Ray Spectroscopy
EIS	–	Electrochemical Impedance Spectroscopy
ESLR	–	Early-Stage-Lithium Recovery
FIB-SEM	–	Focused-Ion-Beam Scanning Electron Microscopy
ICP-OES	–	Inductively Coupled Plasma Optical Emission Spectrometry
ICSD	–	Inorganic Crystal Structure Database
IEA	–	International Energy Agency
LIB	–	Lithium-Ion Battery
LLZO	–	$Li_7La_3Zr_2O_{12}$
LLZO:Ta	–	$Li_{6.5}La_3Zr_{1.6}Ta_{0.4}O_{12}$
LLZO:Ta,Al	–	$Li_{6.45}Al_{0.02}La_3Zr_{1.6}Ta_{0.4}O_{12}$ / $Li_{6.45}Al_{0.05}La_3Zr_{1.6}Ta_{0.4}O_{12}$
LLZO:Ga	–	$Li_{6.4}Ga_{0.2}La_3Zr_2O_{12}$
µCT	–	Micro X-Ray Computer Tomography
PEO	–	Poly-ethylene-oxide
PMMA	–	Polymethylmethacrylat
SEI	–	Solid Electrolyte Interface
SEM	–	Scanning Electron Microscopy
SSR	–	Solid-State Reaction
Tof-SIMS	–	Time-of-flight Secondary Ion Mass Spectroscopy
XRD	–	X-Ray Diffraction Analysis

1 Introduction

With the Paris Agreement in 2015[1], where nations declared to substantially reduce global greenhouse gas emissions, the public awareness for the transition to a more sustainable energy system increased and it became a field of action for governments around the world. For the first time, this agreement outlined clear and tangible goals and parameters for a global energy transition. First effects of this push to a more sustainable energy system, among others, are for example the increasing numbers of electric vehicle car sales.[2] Along with the increasing demand for electric vehicles comes an increasing demand for battery production. The International Energy Agency (IEA) stated in their "World Energy Outlook Special Report 2024", that the level of battery manufacturing capacity tripled in the past four years (until 2023), and with already 70% of them having reached final investment decision, they would be able to produce 8 TWh of battery capacity per year by 2030.[3] Whilst conventional Li-Ion batteries (LIBs) are still improved in terms of performance and production costs, they are projected to reach their energy density limits within the foreseeable future.[4] Additionally, safety aspects must be addressed, as the few large fire incidents related to Li-ion batteries are drawing large media coverage and public attention. To improve both aspects, All-Solid-State Batteries (ASSBs) are a promising new concept, especially when the use of solid electrolytes enable Li-metal as anode to improve energy density. Whilst Li-metal in conventional Li-ion batteries has severe safety risks, especially oxide-ceramic electrolytes have the potential to significantly increase the safety of Li-metal based cells. Particularly the garnet type $Li_7La_3Zr_2O_{12}$ (LLZO) is intrinsically safe as it is the only solid electrolyte material chemically stable towards Li metal. However, one of the major challenges of future oxide battery systems is the high processing cost and energy demand of oxide ceramics. It is therefore necessary to develop new processing routes with minimized energy input and processing time to foster broad industrial implementation.

This increasing demand for batteries in turn increases the demand for battery raw materials. The list of critical raw materials displays several chemical elements which are essential for the use of commercial Li-Ion batteries but also in future battery technologies, such as cobalt, gallium, tantalum, and lithium.[5] In reaction to the criticality of the raw materials, the EU specified requirements for their recycling in the EU recycling Directive from 2023[6]: Recycling efficiencies for lithium-based batteries are required to reach 65% by 2025 (70% by 2030) and material recovery targets are at 90% for cobalt, copper, lead and nickel and 35% for lithium by end of 2025. Furthermore, the use of recycled materials in new batteries is now enforced with a minimum percentage of 16% for cobalt, 85% for lead, 6% for lithium and 6% for nickel from 2031 on.[6] Both points make clear that a successful recycling strategy needs to be evaluated also for new technologies to reach the clear goals set for 2030. Already established industrial recycling at Umicore or ACCUREC[7] uses different recycling approaches for LIBs, such as mechanical, pyrometallurgical or hydrometallurgical routes.[7] During battery recycling, additional risks are associated with the application of high energy density batteries and especially Li-metal anodes, such as thermal runaway during cell disassembly. Even though thermal runaway risks are reduced for ASSBs, recycling processes are not yet established due to the large amounts of cell concepts and materials.

LLZO for example has a lot of valuable materials such as La, Zr, Ta, and Ga to recycle[8], but processing is cost-and energy-intensive. In particular, the embodied energy of sintered oxide ceramics is high and research needs to find recycling strategies towards a direct recycling that allows to refurbish the waste material to minimize re-synthesis and re-processing cost of various battery components.[9–12]

The work presented here addresses strategies for both, reducing the high energy demand and production costs as well as recycling of oxide-ceramic based ASSBs. An investigation of a direct recycling of solid electrolyte LLZO process waste material is performed and furthermore an alternative to the energy- and time-intensive LLZO synthesis is suggested: a simple, fast and energy-efficient one-step *in-situ* LLZO formation process.

2 All-Solid-State battery – Materials, Synthesis, Recycling

The Global report by IEA has highlighted the growing demand for LIBs in the automotive sector.[2] In 2023, the demand increased to 750 GWh, a rise by 40% compared to 2022. The main factor for this increase is the growth of electric passenger car sales.[2] With these numbers in mind, it is important to look at advanced battery development to meet the needs of the market and develop more sustainable and safe high-energy batteries. With the increase in battery production, different battery materials are further expected to become a bottleneck and may even become or are already critical resources.

The present chapter will therefore provide background information about the current and future state of battery technology and its recycling. In the following three subchapters, first Li-ion batteries and their working principle will be summarized; then ASSBs as a promising alternative to LIBs will be introduced and last current recycling strategies will be presented.

2.1 Current status of Li-Ion Batteries

LIBs are the commercially available secondary batteries that are most commonly used in today's portable electronic devices and electric and hybrid electric vehicles.[13] In response to increasingly competitive demand, car manufacturers, battery manufacturers and investors are exploring new opportunities in mining of critical raw materials, but also in new developments in battery technology.[14]

2.1.1 Operation principle of a battery

A battery is an energy storage device and should provide high energy storage density, low environmental impact and high safety. Although there are different types of batteries, such as irreversible redox batteries (primary batteries) like commercial Zn or Li-Ion batteries, only rechargeable batteries (secondary batteries) will be considered in this work.[15] In secondary batteries, such as LIBs, the redox reaction is reversible and a cell can be charged and discharged several times. Once the battery reaches its end of life it should then either be recycled or used for a second life application. LIBs which shall be

discussed in the following as the most important current battery type, belong to the secondary batteries. Their working principle and the reversible redox reduction behind it will be summarized below.

Within the scope of this work, a battery is defined at cell level design to eliminate the influence of different packaging, cell-housings and multi-stacks that play a role in most market-ready battery applications. At cell level, a battery consists of current collectors, two electrodes, one positive and one negative, a separator and an electrolyte. An electrochemical redox reaction resembles the basic principle of batteries, where the mobile ion (in this case Li^+) is oxidized at the anode (negative electrode) and reduced at the cathode (positive electrode) of lower electrochemical potential. During discharge, oxidation occurs at the negative electrode (anode) and reduction occurs at the positive electrode (cathode). The electrons e^- move from the negative electrode to the positive electrode, resulting in an electrical current *I*. Ion movement is opposed to electron movement. During charging, the electrochemistry is reversed, which can be achieved by applying an external voltage. During charging and discharging, the charge carriers, in this case Li ions, are transported in the liquid electrolyte. The principle of a Li ion battery is shown in **Figure 2.1.1**.[16]

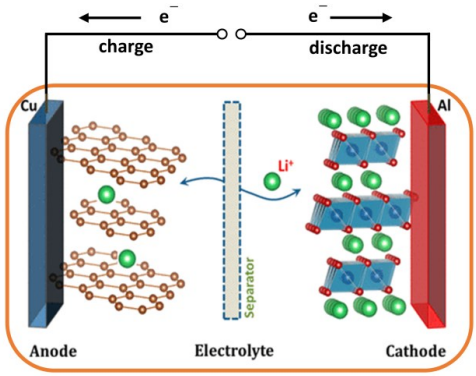

Figure 2.1.1: Working principle of a commercial Li-Ion Battery during charge and discharge. Reprinted (adapted) with permission from [17]. Copyright 2024 American Chemical Society.

The first commercial LIB was developed by Sony in 1991 and the idea is still used in commercial LIBs to date.[18] The following cell structure is used up to date: Graphite is used as anode material, a system of polyvinylidene fluoride (PVDF) with lithium bis(trifluoromethanesulfonyl)imide (LiTFSI) or lithiumhexafluorophosphate ($LiPF_6$) in ethylene carbonate (EC) and dimethyl carbonate (DMC)[19] as liquid electrolyte and $LiCoO_2$ (LCO) as cathode material. The anode and cathode redox reactions during discharge are shown below on the graphite and LCO materials[16]:

$$x\ LiC_6 \rightleftharpoons Li_{1-x}C_6 + x\ Li^+ + x\ e^- \qquad \textbf{Eq. 2.1}$$

$$Li_{1-x}CoO_2 + x\ Li^+ + x\ e^- \rightleftharpoons LiCoO_2 \qquad \textbf{Eq. 2.2}$$

2.1.2 Challenges in Li-Ion Batteries

Although LIBs reach energy densities of up to 770 W h L^{-1} and 260 W h kg^{-1}, they might soon reach their potential limit.[20] To further expand these limits, battery research has to explore new anode and cathode materials or completely new battery concepts to match the demand for increased energy densities. One option to increase energy density in a LIB is a change in the anode and cathode concept, for example using Si or Li as anode and $LiFePO_4$ (LFP) or $Li[Ni_{1-x-y}Co_xMn_y]O_2$ (NCM) as the cathode material.[21] Nanostructured silicon has a theoretical-specific capacity of 4200 mAh g^{-1} [22]. Dahn *et al.* explored composites of C/Si to improve performance.[23] Deng *et al.* studied nanostructures based on iron and copper, which have a higher capacity as graphite.[24,25] On the cathode site, LCO and LFP are commonly used due to their high cycle life (>500 cycles), although LFP has a poor electronic and ionic conductivity compared to LCO, besides its cheap materials.[26] A feature that all commercially available LIBs have in common is the use of a liquid organic electrolyte. Its low flash point around 150 °C sparked widespread criticism about its flammability, especially against the news coverage of large fires related to LIBs.[4]

2.2 Current development of All-Solid-State Batteries

In the present sub chapter, the evolution from LIBs to a new battery concept, called All-Solid-State Batteries will be introduced in more detail, including the structure of ASSBs and the material candidates that may be used for the respective components. Starting with the advantages of ASSBs over LIBs and the material requirements for ASSBs, the following will then address the solid electrolyte and LLZO as a promising option with its synthesis and challenges next, before moving on to the cathode material with a focus on LCO and composite cathodes.

2.2.1 From Li-Ion batteries to All-Solid-State Batteries

Previous research has suggested Li metal as an anode, as it is one of the most promising materials due to its very high capacity (3,860 mA h g^{-1}) and very low standard negative electrochemical potential (−3.040 V).[27] Changing the anode to a higher capacity material, especially in the case of Li metal, will require higher safety requirements to be met though. The main problem with Li metal anodes in the past was the instability of the electrolyte, leading to a decomposition and the growth of Li dendrites causing a short circuit, ultimately leading to temperature spikes inducing a thermal runaway and therefore increasing the safety hazards.[18] With this safety aspect in mind, anode material had been changed to the

much safer graphite material in LIBs. Today, researchers have come up with a different concept to make use of the significant advantages of Li metal anodes: The main idea is to replace the liquid electrolyte by a solid electrolyte. These so-called All-Solid-State Batteries (ASSBs) are predicted by the automotive industry to be already in use in cars by 2025.[28] The solid electrolyte is supposed to be less inflammable, decreasing the safety risk, even when using a Li metal anode. The use of Li metal as anode material and the solid electrolyte material itself increase the volumetric and gravimetric energy density by up to 50% (80%) compared to liquid LIBs[29–31], promising huge advantages of ASSB over current battery technologies. There are various approaches using solid electrolytes, with two main groups: Inorganic solids (crystalline, glass or glass-ceramic) and organic solid polymers, which will be presented in sub chapter 2.2.3. In addition, the dispersion of nanoparticles (solid) in liquids is referred to as a semi-solid electrolyte.[4]

2.2.2 Design of All-Solid-State Batteries

Building upon the idea of a solid electrolyte developed in the above section, a possible structure of a solid-state oxide-based battery is shown in **Figure 2.2.1**. Cu and Al layers as current collectors are fixed onto the anode and cathode outsides respectively. The anode consists of pure metallic Li, and is electrically separated from the cathode by $Li_7La_3Zr_2O_{12}$ (LLZO), a highly researched solid electrolyte, which can work as separator for solid-state batteries. The separator thickness is only 10 µm in this case to increase the gravimetric density of the cell, as its only function is to separate the electrodes. As cathode material, a combination of the active material *e.g.* LCO and a solid electrolyte are shown as an example here, called mixed cathode or composite cathode. The interfaces between the respective layers are of particular importance in ASSBs: On the one hand, geometric contact of 2 rigid bodies represents a technical challenge by itself, on the other hand also the chemical stability must be ensured.

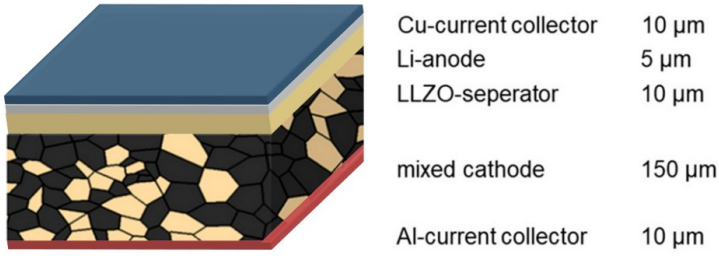

Figure 2.2.1: Possible structure of an All-Solid-State battery from top to bottom with a metallic Li anode, a solid electrolyte and a cathode material adapted from [32] is licensed under CC BY 4.0 (https://creativecommons.org/licenses/by/4.0/).

The solid electrolytes that replace the previously used liquid electrolytes are expected to suppress dendrite growth (a high safety risk in LIBs[33]) and low coulombic efficiency on the Li anode side.[29,34,35] On the other hand, low separator thickness is preferable as thicker separator layers decrease the

gravimetric density. To prevent Li penetrating through the separator whilst minimizing layer thickness, high homogeneity, and mechanical rigidity of the solid electrolyte material is required. Lastly, the layer thickness and mechanical stability also has impact on the processability of the materials which is a precondition for industrial application. The requirements of a solid electrolyte in contrast to LIBs are (1) chemical stability to electrodes, (2) low interfacial resistance of the solid electrolyte-electrode interface (3) easy processability and (4) low thickness in an application as separator.

2.2.3 The solid electrolyte

As introduced in section 2.2.2, solid electrolytes in an ASSB need to fulfill a range of requirements which can be achieved with different types of materials. The first sub section will therefore present the available solid electrolyte material choices before moving on to LLZO as the material of interest in the present work. Its structure, dopants and synthesis will be explained in detail before outlining the challenges related to the use of LLZO as a separator in ASSBs.

Material options for solid electrolytes

The change from liquid electrolytes to solid electrolytes gives room for new materials of two different classes: inorganic solids, such as sulfides and oxides, while solid organic materials are usually polymers. Each class has its own advantages and disadvantages.[36] A wide variety exists also among the inorganic solid electrolytes, for example various oxide solid electrolytes such as garnet[37–39], NASICON[40], perovskite[41], and anti-perovskite[42] have been intensively investigated.[38] Research is also focusing on hybrid solutions either by adding a liquid electrolyte (most commonly only a few drops) to the cell or by combining two solid electrolytes (most commonly a polymer with one of the two others).[36] The spider diagram in **Figure 2.2.2** summarizes the advantages and disadvantages of each group and will be discussed in more detail below. The hybrid concept, which combines a polymer and an inorganic fraction, shows an overall good performance in each category. In the following section, a short overview of polymers, oxides and sulfides will be introduced, as the building blocks of an ASSB cell.

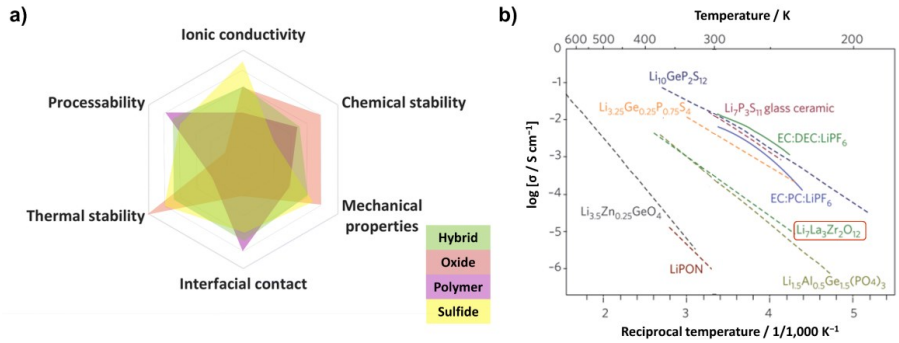

Figure 2.2.2: a) Spider diagram of oxides, sulfide and polymers and their corresponding advantages and disadvantages, adapted from reference [36], used with permission of Royal Society of Chemistry, from [36], 2024; permission conveyed through Copyright Clearance Center, Inc. and **b)** different electrolyte materials with its ionic conductivity, adapted from reference [4] reproduced with permission of SNCSC.

The key property for a solid electrolyte is its ionic conductivity: The higher the ionic conductivity in the solid electrolyte, the better. At room temperature, the ionic conductivity continuously increases from polymers (especially without ionic salt additive) over oxides to sulfides, leading to a high ionic conductivity of 12 mS cm^{-1} for some materials.[43–45] The ionic conductivity as a function of temperature is given in **Figure 2.2.2** for various solid electrolyte materials.[4] Another important factor for a battery component is chemical stability. In this respect, sulfides are the worst performers, whereas the chemical stability of polymers and oxides is higher.[44] For example, LLZO as an oxide material is stable against Li metal,[46] a major advantage over the other materials due to the previously mentioned excellent performance of Li metal in terms of capacity and electrochemical potential. On the contrary, sulfides show a chemical reaction with water in the air, forming the toxic H_2S gas.[45,47] The processing costs of oxides are quite high though, due to the high energy required during the processes, whereas sulfides and even more so polymers have a better processability.[36] Thermal stability, however, is high for oxides: synthesis temperatures above 1000 °C mean that the material is also stable at such temperatures. Sulfides have a slightly lower thermal stability, whilst most polymers already degrade at temperatures above 300 °C.[36] Finally, the interfacial contact is high for polymers, medium for sulfides and low for oxides, due to the solid structure of oxides or ceramics, while polymers are more soft.[36,44] Summarizing all parameters per each material class, one can state that sulfides have a high ionic conductivity but low chemical stability, examples are $Li_{10}GeP_2S_{12}$ or $Li_7P_3S_{11}$. Polymers have low ionic conductivity at room temperature but high processability and interfacial contact, *e.g.* poly-ehtylene-oxide $P(EO)_{12}$-LiTFSI, where LiTFSI enhances the ionic conductivity, and oxides have high chemical and thermal stability but high processing costs, *e.g.* LLZO or $Li_{3.5}Zn_{0.25}GeO_4$. This thesis will focus on oxide materials for a more detailed analysis. Polymers and sulfides will not be discussed in detail except for some recycling approaches focusing on each technology.

One of the main reasons for the use of solid electrolytes, apart from safety, is to increase the energy density. Some of the solid electrolytes have the advantage of enabling a high voltage cathode, increasing the operating voltage to 5 V increasing the energy density. In addition, an even higher energy density can be achieved using Li metal as an anode material. Another central performance feature of a future

battery is how quickly it can release its stored energy, the so-called power density. Rapid charging and discharging in a battery requires high currents, which could lead to thermal hotspots, a risk in LIBs but not in future solid-state batteries due to their higher thermal stability.[4] A reasonably high ionic conductivity in the solid electrolyte is still required to meet the requirements of thick cathodes.[48] The bottleneck of a high-power density cell is the solid electrolyte/electrode interface, which will be discussed later in section 2.2.4. LLZO is one of the promising materials, which fulfil all requirements mentioned above. It has a sufficient high ionic conductivity, especially for a ceramic material, and a high thermal stability. In addition, it is chemically stable against Li metal, although current challenges of Li dendrite growth, high processing costs and high energy requirements are still to overcome. Due to these promising properties, LLZO will be the focus of all following analyses.

Structure of LLZO

The garnet-type structure $Li_7La_3Zr_2O_{12}$ (LLZO) as selected solid electrolyte in this work was first synthesized in 2007 by Murugan *et al*., and was then very quickly implemented in battery systems.[49] There are two different crystal structures in LLZO, a tetragonal structure which is stable at room temperature and changes to a cubic structure at 645 °C.[50] LLZO is found in a garnet-like structure consisting of 8-fold coordinated LaO_8 dodecahedra (24c), 6-fold coordinated ZrO_6 octahedra (16a) and Li ions. These Li ions partially occupy tetrahedral sites LiO_4 (24d) and octahedral sites LiO_6 (48g or off-centered 96h).[51,52] Placing both in a loop creates a three-dimensional network of lithium diffusion paths.[52] It has been found that the octahedrally coordinated Li ions are mobile, while Li ions on tetrahedral sites appear to be immobile.[53] With increasing number of Li ions depending on the amount of Li in the LLZO, the Li-Li repulsive interaction destabilizes the octahedral sites and increases the mobility of the Li ions.[54] This can be seen in the ionic conductivity of the two structures, which differ by two orders of magnitude, with an ionic conductivity of 10^{-6} S cm^{-1} for the tetragonal structure and 10^{-4} S cm^{-1} for the cubic structure at room temperature without any dopants. This value is promising, although other solid electrolytes may have even higher conductivities.[55,56] A garnet-type structure of LLZO is depicted in **Figure 2.2.3**.

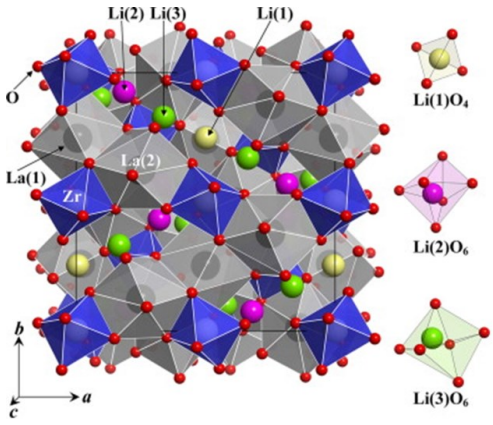

Figure 2.2.3: LLZO crystal structure in a garnet-like structure reprinted from [57] with permission from Elsevier.

Modifying the ionic conductivity with dopants in LLZO

LLZO in its cubic structure has a promising ionic conductivity already in its pristine form, but can be further modified by various dopants which shall be discussed in the following section.

Even the first LLZO synthesis had an unintentional and therefore unknown doping with Al ions, due to sintering in commonly used alumina crucibles, which stabilizes the cubic structure at room temperature.[58,59] There are three different sites, where dopants can be located, the Li site, the La site and the Zr site. Al ions are known to occupy the Li site leading to a typical ionic conductivity of 2×10^{-4} S cm^{-1}.[60] Another typical dopant for Li sites are Ga ions, which further increase the ionic conductivty to 2×10^{-3} S cm^{-1}, still stabilizing the cubic structure at room temperature.[61–65] A third, less commonly used dopant would be Fe ions, but this has not been extensively researched.[66] A major disadvantage of Ga doping, which leads to a high ionic conductivity compared to the other dopants, is its instability towards metallic Li.[61] Metallic Li for anodes is one of the reasons for exploring solid oxide electrolytes, as it increases the energy density in batteries due to its high specific capacity and low electrochemical potential compared to conventional anode materials.[27,67] Besides the Li site also the Zr site in LLZO can be doped to achieve high ionic conductivity with any of the following dopants: Ta, Sc, Nb, Y, W, Gd, Mo, Sb, and Te.[68,69] In this work only Ta doped LLZO is analyzed as it has a promising high ionic conductivity of 1×10^{-3} S cm^{-1}.[55] The other mentioned dopants have ionic conductivities that can be as high as the Ta dopant of 2×10^{-3} S cm^{-1}.[55] Doping La sites is also possible but not evaluated in this work. Typical dopants on the La sites are Rb, Ba, Ca, Ce and Nd. Co-doped LLZO with Ca and Nb for example reaches an ionic conductivity of 9.5×10^{-4} S cm^{-1}.[70]

Whilst multiple dopants exist for LLZO, this work will focus on the following three dopants: Al, Ga, and Ta. Here, Al and Ta are also used as co-dopants in LLZO, which allows to stabilize the cubic structure at room temperature and increases the ionic conductivity.

Synthesis of LLZO

After determining the dopants of the LLZO which are used in the following work, it is necessary to evaluate how LLZO is synthesized and further processed. For high-quality LLZO separators, thin, flat and dense layers need to be produced.

To manufacture a final battery component, a powder synthesis, a shaping and a final sintering step are usually required. There are several approaches to synthesize LLZO, most commonly as powder. Depending on the subsequent process to shape the battery components, synthesis varies between a solid-state reaction or wet chemical technique.[38] A solid-state reaction (SSR) involves a chemical reaction from simple oxides to complex oxides or other materials.[71] It allows the preparation of large volume batches.[71] Usually, the process requires long calcination times at high temperatures of 900 °C or more, as well as several milling steps to increase homogeneity and reduce particle size as smaller particles are more reactive.[71] These steps not only add time but also increase energy consumption of the whole process.[72,73] Ball milling of the mixed oxide precursor materials is generally used to obtain fine particles with homogeneous elemental distribution, required for high-quality LLZO. Another synthesis approach besides a solid-state reaction would be a sol-gel process, which requires at least 500 °C as calcination

time after sol-gel synthesis to produce cubic LLZO powder.[73,74] In addition to sol-gel processes, LLZO can also be synthesized by flame-spray pyrolysis.[75,76] Sol-gel synthesis, spray pyrolysis, co-precipitation, and solid-state reaction all showed successful LLZO formation, although ionic conductivities vary.[72,77–80] The precursor selection depends on the synthesis process and may vary even between similar processes.

An understanding of the formation of LLZO is furthermore a prerequisite to follow the experimental route that is presented in this work. Depending on the precursors, the synthesis route and the doping of the LLZO, the formation of the intermediate phases differs. With oxide precursors, intermediates are already formed at low temperatures, such as $La_2O_2CO_3$ at 200 °C[81] and $La_2Zr_2O_7$ above 400 °C[82]. At higher temperatures, the precursors, such as La_2O_3, ZrO_2 and Li_2CO_3 coexist with the intermediates until LLZO is formed.[82] The temperature at which LLZO forms varies, but is usually around 700 °C to 800 °C. When Li_2CO_3 is used as a precursor, its melting point (713 °C) leads to a decrease of La_2O_3 and ZrO_2 and an increase of the $La_2Zr_2O_7$ phase, therefore, the subsequent formation of LLZO.[82] Rao *et al*. suggested that LLZO formation is observed above 800 °C,[82] while Geng *et al*. already found the LLZO phase at 680 °C.[81] Another study shows in more detail the different phase formations from 600 °C to 1000 °C.[83] They also report LLZO phase formation at 720 °C, again with Li_2CO_3 the melt phase initializing the reaction. Here, not only $La_2O_2CO_3$ and $La_2Zr_2O_7$ are present in addition to the precursors, but also the Li_2ZrO_3 phase. $La_2Zr_2O_7$ has its maximum at 800 °C, however, after a dwell time of 60 minutes at constant temperature, LLZO formation had reached its maximum at the same temperature. Chen *et al*. also investigated two different dopings, Al and Zn.[83] Both show additional intermediate phases: $LaAlO_3$ and $Li_{0.5}La_2Al_{0.5}O_4$ were found for Al-doping and a Zn-O phase for Zn-doping. For Al-doping, the $La_2Zr_2O_7$ phase maximum was shifted to 780 °C, while the $La_2Li_{0.5}Al_{0.5}O_4$ phase has its maximum above 750 °C and decreases with the formation of LLZO:Al.[83] A different approach to the investigation of LLZO and LLZO:Al has been taken by Košir *et al*. who also investigated the difference between a solid-state reaction and a sol-gel process.[84] Again, $La_2Zr_2O_7$ is the main intermediate phase next to the precursors, while Li_2ZrO_3 is only seen for the LLZO:Al doped solid electrolyte. Similarly, $La_2Li_{0.5}Al_{0.5}O_4$ and $LaAlO_3$ are intermediate phases. Comparing solid-state reaction and sol-gel processes the maximum of LLZO formation is shifted to lower temperatures than 1000 °C as for the solid-state reaction. It also explains the appearance of $La_2Zr_2O_7$ as one of the major secondary phases in impure LLZO.

Processing of LLZO

Once the LLZO powder has been synthesized, a shaping process is required to produce the battery components. The primary goal is to create a thin and dense separator layer that completely covers the electrode and prevents the cell from shorting out. Three different groups of ceramic shaping methods exist: Casting, plastic processing or pressing.[85] This translates into equivalent approaches to the design of separators[72]: 1) thin films on a substrate to minimize the thickness of the separator itself, either by PLD (pulsed laser deposition)[86,87] or ALD (atomic layer deposition)[88], 2) free-standing thick films of several tenth of micrometers[89] or 3) the use of bulk materials[90]. A new approach is also being developed – 3D networks.[39] The idea behind this structure is to achieve a finely distributed ionic conducting phase, *e.g*. with fibers, which can be implemented in a rigid or soft structure depending on the needs of the

battery. Furthermore, these structures can also be used to maximize the surface area to volume ratio of the interface of a separator|electrode interface.[91] Based on this new development, it has even been possible to maximize the surface area of both electrodes, with a thin separator layer in between, creating a three-layer structure of porous, dense, and porous LLZO.[92]

Several approaches exist for thick films, ranging from about 10 micrometers to several hundred micrometers.[93] Spin or dip coating can be used with an additional substrate, resulting in films with a high range of thickness, suitable for a solid electrolyte. A free-standing process would be dry-pressing millimeter-thick pellets.[72] A uniaxial press is filled with powder, obtaining a green pellet, which can be cut into smaller slices after sintering. However, even after polishing, the thickness is several hundred micrometers, and the only purpose of these pellets is the usage in research.

Another shaping approach is screen-printing or tape-casting[94], a widely used industrial tool, which results in large, films with a minimum thickness of 10 µm after drying. The tape-casting process is the central method for the shaping of battery components in this work. Slurry based on the ceramic powder was used to create flat films, large in x- and y- direction with a height of <10 µm up to several mm in z-direction.[93] These large sheets are suitable not only for thin separator tapes, but also composite cathodes can be cast with a higher thickness to increase the active material loading.

One of the first processed ceramic layers produced via tape-casting was described in 1947 by Howatt *et al.* for thin capacitor sheets.[95] The tape casting process can be described using the following five steps: 1. Slurry preparation, 2. Tape-casting; 3. Drying; (4. Organic removal; 5. Sintering), resulting in sintered sheets with only ceramic inside. Typically, a blade is used in a specific height (gab bar) over a conveyer belt with a foil as carrier. Over the length of the table, the tape can dry, either in air or using an additionally heating. A scheme of a tape-casted bench can be seen in **Figure 2.2.4**.

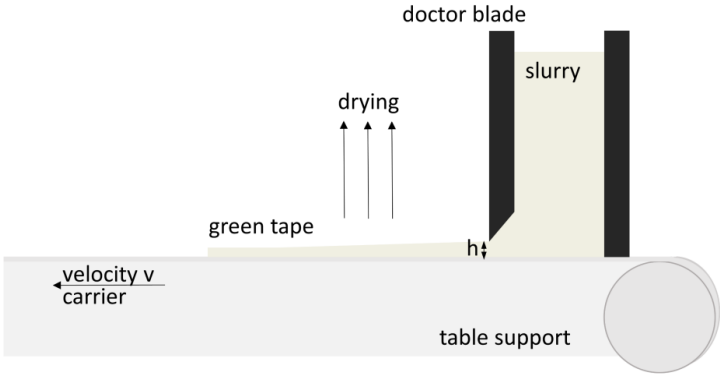

Figure 2.2.4: Example of a tape-casting bench with a doctor blade, slurry and a conveyer, adapted from [93].

The slurry consists of the ceramic powder, a binder, solvent and additives, which will be mixed and sometimes degassed before tape-casting on the foil.[96] Basis of the slurry is a stable suspension, depending on the surface of the particles used in the process. The used solvent, binder, plasticizer and powder have interdependent influences on the resulting slurry. A good slurry prevents the tape from

defects: Those defects can be foaming, cracking during curing, brittleness, curling during curing, poor surface quality of the tape, de-wetting marks and stress marks or cracking during sintering.[96]

The slurry highly depends on the used materials, whereas the tape in turn is strongly influenced by the characteristics of the slurry including viscosity. Two central parameters with an influence on the slurry are the particle size distribution (PSD) and particle morphology. It is of high interest that the particle size distribution is optimized to fit the organics used in the final slurry. The dispersant is used for de-flocculation of the particles and minimizes agglomeration by stabilizing the primary particles. The binder in the slurry is used to bind the particles in the green foil in a continuous matrix. The solvent used needs to be chemically stable in combination with the powder and have sufficient vapor pressure. Vapor pressure is important for a defect-free drying phase. Furthermore, the solvent influences the viscosity of the slurry, and for safety, environmental and economic reasons, it should be a non-toxic, cheap solvent. Additionally, additives are normally added for an optimal slurry. Plasticizers of type I are in direct reaction with the binder and sometimes the dispersant, whereas type II plasticizers react between the binder material and the ceramic particles. Here, the additive enhances the rheological behavior, so particles and polymer can move during drying time and prevent cracks.[96]

Sintering of LLZO

Sintering as the step after the shaping is important for ceramic powder for several reasons: It increases the density of the tapes (shrinkage) as well as forms cohesive grains, resulting in higher ionic conductivity of the LLZO as well as a stabilization of thin tapes. Different definitions of sintering exist in literature but they usually have in common, that particles with a basic body shape undergo a chemical transport mechanism by heat treatment, which leads to a shrinkage based on filling of pore volume in the body. The main driving force of sintering is to reach a system with minimal free enthalpy. Particles have a high surface to volume ratio and therefore high surface energy, which can be used at high temperatures to maximize material transport. For sintering, three different driving forces existing: pressure, chemical reactions and curvature of free surfaces. The mechanism behind the sintering is the diffusion of atoms and vacancies, which can occur when defects are present in the lattice. There are six different mechanisms of diffusion such as surface and lattice diffusion to transport material to the contact areas.[97,98] Vapor transport and surface diffusion lead to coarsened sintering necks but not higher density. Density can be improved by diffusion at the grain boundaries and lattice diffusion from the grain boundary. In amorphous parts of the solid, plastic flow can also happen. A summary of the different sintering mechanisms that can take place is given in **Figure 2.2.5**.[98,99]

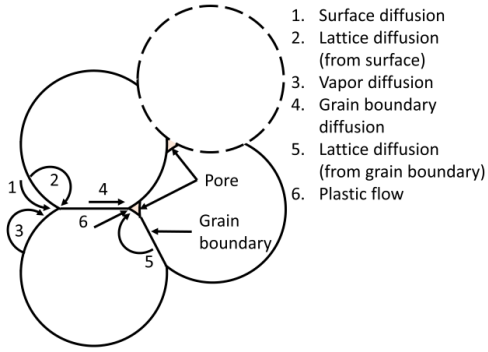

Figure 2.2.5: Scheme of different diffusion steps during sintering adapted from [98].

Sintering processes are separated into three stages: First an interparticle neck forms, each particle has a high amount of contacts and the sintering necks reach nearly 40-50% of a particle radius, while the ceramic is shrinking of 3-5 vol%.[99] During this step, pores are formed which are filled in the second stage, where the highest shrinkage of the ceramic takes place. As soon as the pores are closed, no degassing can happen anymore, the relative density reaches ~90%.[98,100] Further densification is not always possible. Only mobility of the pores can yield higher densification, furthermore, in polycrystalline solids, grain boundary growth interferes with densification. Usually Oswald ripening takes place, getting rid of small particles in favor of increasing the size of bigger particles.[98,100,101]

Next to the conventional sintering approach explained above, there are many more sintering techniques. Here, only one different mechanism will be highlighted as it will be part of the discussion later on. Usage of a melting phase can also lead to high densification (liquid sintering).[102] As mentioned above a molten transcend phase can enhance the density of a body, which is called liquid phase sintering. With only 25-30 vol% of liquid, increasing rearrangement and enhanced matter transport lead to a higher densification.[98] Usually, liquid phase sintering exhibits internal forces through capillary interactions, making external pressured induced forces unnecessary.[102] Either the second phase starts melting or forming at higher temperatures a eutectic. Nevertheless, effects such as temperature and time amongst other having still a high influence on the density. One major advantage of a liquid phase sintering would be the result of faster sintering. Due to the enhanced atomic diffusion, the capillary attraction gives a fast densification, and furthermore reduces the interparticle friction helping a fast rearrangement of the solid. One major disadvantage is the overuse of the liquid phase resulting in shape distortion and thicker amorphous grain boundaries. Due to the enhanced speed in sintering, it is less predictable than solid state sintering.[102] If the liquid phase is not uniformly distributed, it can create localized regions of enhanced grain growth, leading to abnormal grain growth. For example, it can be difficult to control the amount and distribution of the liquid phase, which can lead to uneven densification and poor microstructure. Additionally, the liquid phase can react with the solid phase, leading to changes in composition and properties.[102]

In all cases, sintering takes place to further densify the ceramic green battery component. High energy inputs are required for high temperatures and long sintering times.[72] Next to conventional sintering, there

are different sintering techniques. A combination of pellet pressing and sintering simultaneously is employed by FAST/SPS (Field-Assisted-Sintering Technology / Spark-Plasma Sintering),[103] where the powder is heated under pressure, much faster than in a conventional furnace, resulting in high-density pellets.[104] On the other hand, ultra-fast high-temperature sintering (UHS) reduces the sintering time to as little as 10 s.[105] The table displays the short name of the synthesis route, the precursors, the calcination temperature, and subsequent battery component forming process with the resulting thickness and ionic conductivities of the solid electrolytes:

Table 2-1: Summary of LLZO synthesis in different approaches with precursors, calcination temperature and the following process for battery component with resulting thickness and ionic conductivity of the solid electrolyte.

Synth.	*precursors*	*Calcination temp. [°C]*	*Shaping process*	*Sintering [°C, h]*	*Thickness [µm]*	*Grain size [µm]*	*Ionic cond. [mS cm^{-1}]*	*Ref.*
SSR	LiOH, La_2O_3, ZrO_2, Al_2O_3	850 + 1000	Dry pressing	1200, 30	n.r.	n.r.	0.31 (25 °C)	[72]
SSR	Li_2CO_3, La_2O_3, ZrO_2, Al_2O_3	1100	Dry pressing	1100, 6 argon	300 - 400	n.r.	0.3–0.4 (25°C)	[106]
SSR	LiOH, La_2O_3, ZrO_2, Al_2O_3	850 + 1000	Tape-casting	1175, 10	50 - 240	n.r.	0.39 (25 °C)	[107]
SSR	LiOH, La_2O_3, ZrO_2, Al_2O_3	850 + 1000	Tape-casting	1175, 4	150	3 – 8 [a]	0.15 (25 °C)	[108]
SSR	LiOH, La_2O_3, ZrO_2, $CaCO_3$, Nb_2O_5	900	Tape-casting	1050, 1	70-14-70 35-14-35	< 10 [a]	n.r.	[92]
Sol-Gel	Li-, La-, Zr-acetylacetonate	600 / 800	Dry pressing	1100, 6-15 1200, 2-12	n.r.	5 – 10 [a]	0.24–0.67 (25 °C)	[109]
Sol-Gel	$LiNO_3$, $La(NO_3)_3$, Zr(OH7C3) n-propanol	450 + 1000	Dry pressing	1000, n.r. 40 MPa hot-pressed	n.r.	0.26	0.4 (25 °C)	[110]
Solution	Li_2CO_3, $La(OH)_3$, $[ZrO_2]_2CO_2{\times}H_2O$, $GaCl_3$	650	Dry pressing	1000, 4	n.r.	3	0.35 (25 °C)	[64]
CP	$La(NO_3)_3$, Li_2CO_3, $Zr(NO_3)_3$, NH_4HCO_3	850	Dry pressing	1150-1200, 20	n.r.	> 10	0.2 (25 °C)	[111]
CP	$La(NO_3)_3$, $Li_2C_2O_4$, $Zr(NO_3)_4$, $Al(NO_3)_3$,	900	FAST/SPS	800-1000, 3min, 10 MPa	n.r.	n.r.	0.33 (25 °C)	[112]
NSP	$La(NO_3)_3$, $Al(NO_3)_3$, $Zr(C_5H_7O_2)_4$, $LiNO_3$,	900	FAST/SPS	950, 10 min 50 MPa	n.r.	0.5 - 3	0.3 (25°C)	[113]
UHS	Li_2CO_3, La_2O_3, ZrO_2, Al_2O_3, Ta_2O_5	n.a.	Dry pressing	1500, 10 s (UHS)	n.r.	6.5- 10.5	0.1 (25°C)	[105]
FSP	$LiO_2CCH_2CH_3$, alumatrane, La- and Zr-isobutyrate	n.a.	casting	1090-1100, 1 N_2	22 - 73	2.4	0.2 (25 °C)	[75]
RS	$La_2Zr_2O_7$	850 °C	Dry pressing	1100, n.r.	n.r.	n.r.	0.4 (25 °C)	[114]

[a] = from SEM extracted, n.r. = not reported, n.a. = not applicable, SSR = Solid-state reaction, CP = co-precipitation, NSP = nebulous spray pyrolysis, UHS = Ultra-Fast-High-Temperature Sintering, FSP = Flame-spray pyrolysis, RS = reactive sintering

Summarizing the above, it can be said that LLZO synthesis and processing it into a functional separator usually requires a long process with variable steps often including high energy consumption due to several furnace treatments during the entire process. This leads to high cost and high energy requirements to synthesize LLZO, the processing afterwards not yet included. Sintering at high temperatures (usually above 1000 °C) include another long high temperature sintering step. This represents a significant challenge for industrialization as cost and energy requirements should be as low as possible.

Challenges of LLZO

Initially there was consensus that LLZO was stable in air, but more recent studies have found that LLZO undergoes a surface reaction with humidity and CO_2, depending on the time of exposure.[38] The Li_2CO_3 that is formed affects the interfacial resistance of LLZO and minimizes the ionic conductivity due to the low wettability of Li on the carbonate covered surface.[115,116] The surface contamination can be explained by a Li^+/H^+ exchange where H_2O reacts with the LLZO to form LiOH and this further reacts with the CO_2 in air to form Li_2CO_3, which is mainly found on the surface and at grain boundaries.[116] Furthermore, Wen *et al*. suggested that the lattice expansion is related to the Li^+/H^+ exchange, but is reversible and cubic LLZO can be recovered.[117] The equations of the chemical reaction are as following:

$$Li_7La_3Zr_2O_{12} + xH_2O \rightarrow Li_{7-x}H_xLa_3Zr_2O_{12} + xLiOH \qquad \textbf{Eq. 2.3}$$

$$Li_7La_3Zr_2O_{12} + xCO_2 \rightarrow Li_{7-2x}La_3Zr_2O_{12-x} + xLi_2CO_3 \qquad \textbf{Eq. 2.4}$$

To prevent the formation of Li_2CO_3, LLZO could be stored and handled in an inert atmosphere. However, since production takes place in air and sometimes prevention is not possible, it is also possible to remove the formed Li_2CO_3. Two main ideas are considered to remove Li_2CO_3 contamination on the surface: either by mechanical polishing (dry or wet) of the surface, which is only possible for pellets that are mechanically stable, or by thermal treatment.[115] The above reaction is reversible at temperatures above 500 °C and therefore a heating step can be performed to remove the Li_2CO_3. Another way would be to use the Li_2CO_3 contamination in a direct reaction with *e.g.* Co_3O_4 to form LCO surrounding the LLZO particle.[118] Although researchers tend to minimize the surface contamination in air to Li_2CO_3, Grissa *et al*. recently showed the dependence of Li^+/H^+ exchange on stripping and plating during CCD measurements and thus the protonated phase of LLZO is of importance.[119]

Furthermore, the effect of different dopants on either the ionic conductivity or the processing of LLZO needs to be considered. While dopants not only influence the ionic conductivity and support the stability of the cubic phase at room temperature, they also have some influence on the synthesis, especially the sintering itself, which is visible in the resulting microstructure. For example, abnormal grain growth has been reported for Ga and Al dopants.[120,121] Abnormal grain growth can affect mechanical properties and grain boundary properties and is usually difficult to control, as discussed later. Yamazaki *et al*. reported enhanced grain growth to several hundred microns due to a Li-Ga-O liquid phase formed by the addition of Ga dopant from 3 mol% in LLZO:Ta. Not only is grain growth enhanced, but pores of several micrometers are also retained in the grains, suggesting rapid grain growth. With 5 mol% Ga_2O_3 addition

they achieved an ionic conductivity of $1.1 \cdot 10^{-3}$ S cm^{-1} and with 2 mol% addition a critical current density of 0.8 mA cm^{-2}. The main advantage of LLZO:Ga is the high ionic conductivity of $2.0 \cdot 10^{-3}$ S cm^{-1} [61], while the main disadvantages are the high cost and the chemical instability towards Li metal. Li *et al*. not only demonstrated the instability of LLZO:Ga towards metallic Li, but also suggested a way to overcome this problem by adding SiO_2 to form a Li_2SiO_3 glass phase.[61] Chen *et al*. doped LLZO with Al and Ga in different ratios and found that as soon as Ga-ions are used as dopant, the grains start to grow larger, and again isolated closed pores are found [120]. In LLZO:Al without Ga-doping, the grains are typically between 5 – 20 µm in size and no abnormal grain growth is observed. A liquid phase is presented as reason for the larger grains.[122] Contrary to these findings, Kim *et al*. found Al segregation at grain boundaries, suggesting a preference for Al dopant at 96h sites. They also found abnormal grains with an average size of 167 µm.[123] Liu *et al*. took a different approach by using Nb and Ta co-doping in LLZO to see the influence of a dopant with a lower melting temperature than ZrO_2, although the melting temperature is still above the sintering temperature.[68] They report a change in grain shape and an increase in grain size up to 22 µm, depending on the amount of dopant used.

In summary, beyond its high production cost and energy requirements, LLZO brings not only challenges during synthesis, with dopants influencing the processability of LLZO, especially during sintering, but further LLZO is not stable in air. The Li^+/H^+ exchange plays a large role in the LLZO synthesis and further processing as it takes place in air. These topics need to be addressed in order to realize the great potential of LLZO as a separator material.

Challenges at the interface LLZO|anode

In addition to the manufacturing of LLZO, its doping and instability toward air, the interface of the solid electrolyte with anode remains another challenge. One of the many problems is the high interfacial contact resistance due to solid-solid contact, resulting in low cell performance. The aforementioned LLZO separators are also known for Li dendrite growth.[124] Initial suggestions for the cause of Li dendrite growth were the low density of the separators, with Li growing in the pore, leading to a short circuit in a full cell.[125] After the LLZO films/pellets were dense and Li dendrite still occurred, it was suggested that either surface cracks or poor wetting of the lithium metal, and therefore only local contact, created sites for nucleation and dendrite growth.[126] It is now suggested that the electronic conductivity of LLZO, which is thought to be low, causes Li dendrite growth.[127] Although it is not clear how to fully explain Li dendrite growth, it has been successfully demonstrated that LLZO is stable against Li metal up to 1 mA cm^{-1} at room temperature in a symmetric cell.[128]

In contrast to Li dendrite growth, the second problem with the Li metal anode is the wetting of Li on LLZO. This is again visible in high interfacial resistances, making it difficult to distinguish between the two cases. The wetting of Li on the LLZO surface could be improved by adding a small amount of liquid electrolyte to the interface.[129] However, most researchers would like to stick to a full solid-state battery, so lithium metal alloys are also used to overcome the wetting problem. For example, a Li-Al alloy has been introduced as an interfacial layer between LLZO and Li, increasing the wetting ability of the solid electrolyte.[130]

The interfacial resistance between LLZO and the anode, due to contamination by Li_2CO_3 or due to poor wetting of Li on the LLZO surface, is high compared to liquid electrolytes in LIBs. In addition, Li dendrite growth is still a problem in most of the synthesized LLZO solid electrolytes. Although some of the problems have been addressed, there are still open issues to be resolved in order to improve the performance of LLZO in a cell. On the other hand, the LLZO interface to the cathode side has similarly high interfacial resistances, although different problems occur. Due to the complexity of composite cathodes and the interface challenges of LLZO to the cathode site, a detailed analysis is given in the following sub-section.

2.2.4 The cathode active material in composite cathodes

This chapter will first evaluate different cathode active materials, followed by the synthesis and processing of composite cathodes with a special focus on LCO and LLZO, and the potential challenges occurring in composite cathodes.

Possible cathode active materials in composite cathodes

A cathode active material has to fulfil several tasks to be suitable for a battery system. Firstly, it should have a high potential vs. Li/Li+ and a high Li ion capacity. Combining the high capacity with a high voltage (around 4 V) results in a high energy density. In addition, the material should be capable of reversible lithiation and de-lithiation with high structural stability and minimal volume change during charging/discharging. Furthermore, not only is a high Li ion capacity required, but the material must also be a good electronic conductor to enhance the electrochemical reaction at all interfaces between the active material and the electrolyte. From a production and recycling point of view, the material should be environmentally friendly, cost effective, available in large quantities around the world and easy to recover without side reactions.

Several cathode active materials are commonly used in batteries, especially in commercial LIBs. These include olivine $LiFePO_4$ (LFP), spinel $LiMn_2O_4$ (LMO), and $Li[Ni_{1-x-y}Co_xMn_y]O_2$ (NCM), $Li[Ni_{0.8}Co_{0.15}Al_{0.05}]O_2$ (NCA), and $LiCoO_2$ (LCO), each as layered cathode material. Since LFP comes in an olivine structure, the diffusion pathway is limited to a one-dimensional diffusion mechanism, contrary to the two-dimensional diffusion mechanism in layered transition metal oxides and the three-dimensional diffusion mechanism in spinels.[131,132] The capacity and operating voltages for each of these materials are summarized in **Figure 2.2.6**.

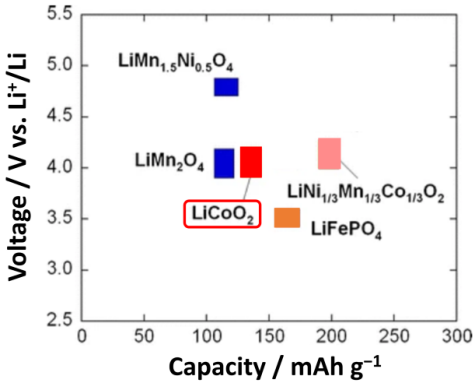

Figure 2.2.6: Promising cathode active material with their voltage and capacity ranges in LIBs. Adapted from [133], reproduced with permission from Springer Nature.

Furthermore, due to their low ionic conductivity and to achieve high active loading in the cathodes, the cathode active material is paired with a solid electrolyte for All-Solid-State cells, as a composite cathode. Since the solid electrolyte is fixed to an LLZO separator in this work, the cathode active material should have an interconnected framework within the LLZO in order to have ionic and electronic conductivity across the full thickness of the cathode. In addition, due to the use of LLZO and its high sintering temperature requirement above 1000 °C, a comparable thermal stability to LLZO is required. Ren *et al*. investigated the stability of LFP, NMC and LCO against LLZO and found that LFP reacts with LLZO at 500 °C.[134] Besides, LCO is said to be more stable up to temperatures of 1050 °C, than NMC, which reacts at 700 °C.[135–137] Due to the intercalation and de-intercalation the cathode material experiences volume changes. In the different cathode active materials introduced above the volume changes are as high as ~6.8% for LFP[138], ~3.4% for NMC[139], ~5.9% for NCA[139] and ~2% for LCO.[140]

In this work LCO will be used as cathode active material in the composite cathodes together with LLZO.

Structure of LCO

LCO as the cathode material of interest in the present work has also been the most commonly used cathode active material for commercial LIBs. It crystallizes in a layered oxide structure with a high potential of 4.4 V - 3.8 V vs Li/Li^+ and was introduced by Goodenough *et al*.[141] LCO can occur in different phases, but the one synthesized at high temperatures is considered to be the most suitable. It has rhombohedral symmetry (*Rm*3), a high theoretical specific capacity, low self-discharge and good cycling performance.[142,143] Although LCO has a high theoretical specific capacity of 274 mAh g^{-1},[144] not all Li can be depleted from the structure for stability reasons.[140,145] Only 50% of the theoretical capacity can be accessed as the remaining Li ions are necessary to stabilize the LCO structure. The CoO_2 layers would repel each other if the differently charged Li ions were removed from between the layers destroying the beneficial structure.

It is also worth mentioning that LCO is criticized in commercial use due to its high health risk (carcinogenic) and the ethical issues of mining Co in the world, besides the fact that Co is listed as

critical raw material.[146] However, as it is still the most commonly used cathode material and suitable for combination with LLZO, it will also be investigated in the following work.

Synthesis and Processing of composite cathodes

LLZO and LCO as the chosen materials for the composite cathode can be processed together. Composite cathodes made from ceramic materials are not easy to produce. Nevertheless, various methods of synthesis have been explored over the years, resulting in numerous publications.[147] The established processes developed can be summarized in three different categories: Either the composite cathode is deposited as a film on a dense ceramic LLZO pellet,[148] or LLZO and cathode active material powder are co-sintered in a pre-forming step to a suitable battery component,[149] or the composite cathode is produced *in-situ* in an already existing LLZO framework.[150] A completely different approach was used by Yang *et al*. where the LLZO was coated with LCO by a reaction of the Li_2CO_3 on top of the LLZO particles and Co_3O_4 added.[118]

All the different methods have some advantages and disadvantages, but they all have the use of a pre-synthesized LLZO, either as a powder or as an already sintered framework in common. The deposition of the films can be accomplished as cathode active material and composite cathode by either pulsed laser deposition[122,151,152], sputter deposition[153,154], or sol-gel deposition[155], and require a much lower synthesis temperature for LLZO of around 700 °C.[156] The disadvantage of this method is the limitation to low thicknesses, resulting in a low active material loading, which negates the need for battery materials with high energy density. Co-sintering of LLZO and LCO powders makes it possible to produce thick cathodes in the battery system with sufficiently high active material loading. A variety of different shaping and sintering approaches are used to produce dense composite cathode materials, either on LLZO pellets by screen or ink printing[157,158] or as a free-standing structure.[159] Half cells of a separator and the composite cathodes have also been processed by field-assisted sintering (FAST/SPS)[103] and composite cathodes on pellets or free-standing composite cathodes have been densified either by conventional sintering[159,160]or photonic sintering.[157] A major drawback of the co-sintering approach is the high temperature required for densification, which leads not only to the diffusion necessary for sintering but also to a certain interdiffusion of the material, resulting in secondary phases with undesirable properties.[161] Besides the interdiffusion, also the chemical and electrochemical stability, the volume changes during charge/discharge and undesirable side reactions represent challenges that are still under investigation for a good composite cathode microstructure.[147,162]

Challenges in composite cathodes

Besides the above-mentioned challenges during synthesis of a composite cathode, further issues arise for a full cell assembly and a working battery. These need to be addressed to reach and excel the performance of batteries that are currently on market.

In a composite cathode, two materials with different lattice sizes are co-sintered or in close contact. Due to the brittleness of the all-ceramic composite cathodes, even small volume changes, induced from intercalation and de-intercalation lead to crack formation, resulting in contact loss with higher resistances and finally to mechanical degradation of the cell during the first cycle. Mücke *et al.*

investigated the anisotropic expansion along the crystal axes, however, and found that the crystallographic orientation of the grains in the microstructure play a crucial role and can minimize crack formation.[162] In addition to this major problem, interdiffusion also takes place between the solid electrolyte and the cathode active material, even though LCO is the most stable cathode active material at high temperatures compared to LLZO.[134] Interdiffusion and its effect on cycling performance will be briefly discussed in the following sub-section. Composite cathode processes involve the creation of a conductive interface between the solid electrolyte and the cathode active material. The sintering of the ceramic materials is driven by diffusion, which may include interdiffusion between the cathode active material and the solid electrolyte. This interdiffusion may result in a poor interface between the solid electrolyte and the cathode active material, which could lead to a high interfacial resistance, resulting in poor cell performance.[147] On the other hand, there are two other failures during cycling that lead to high degradation of the cell. The mechanical failure and the chemical failure, again including interdiffusion of ions. For each problem, different investigations have been carried out in the literature. Cell designs of $LiMn_2O_4$ and LLZO or Li|LLZO|LFP have been analyzed, resulting in 94% capacity retention after 20 cycles and 85% after 100 cycles, respectively.[163,164]

Zhu *et al*. performed a first-principle study of the LCO-LLZO interface and found that LLZO has a decomposition energy of −1 and −39 meV for Li_1CoO_2 and $Li_{0.5}CoO_2$, respectively.[165] The first reported Li|LLZO|LCO cell with a poor capacity of only 15 μAh cm^{-2} was published three years after the first report of LLZO. [166] Low capacity and high degradation have led to intensive study of the LLZO-LCO interphase, particularly at elevated temperatures. The results of these studies vary, probably depending on the synthesis and dopants used. For example, Uhlenbruck *et al*. and Tsai *et al*. found that LLZO:Ta and LCO are stable up to 1085 °C and at 1050 °C, respectively.[158,167] Although Raman measurements were used to investigate the stability of the latter, the same method showed a new peak at 658 cm^{-1} after a heat treatment at 700 - 900 °C, indicating a change of structure and creation of a new phase.[134] Tsai *et al*. also found that LLZO:Ta prevents interdiffusion, while LLZO:Al leads to highly resistive tetragonal LLZO phases.[158] Similar tetragonal phases were found by Park *et al*. due to cross-diffusion.[155] The interdiffusion of Al ions from a direct interface of LCO sintered on a LLZO pellet was investigated by TEM and EDS measurements already at 700 °C.[155] Furthermore, Kim *et al*. investigated the interface of LCO-LLZO, where a reaction layer of La_2CoO_4 of 50 nm was formed during the synthesis process.[122] These results indicate that the LLZO-LCO interface indeed represents the main challenge for capacity density limitation and degradation of LLZO-LCO composite cathodes. On the other hand, they provide the foundation for future process optimization to produce composite cathodes with higher quality.

Loss of performance and rapid degradation of cells can have either chemical or mechanical causes. Ihrig *et al*. showed the diffusion of Al-ions into LLZO during cycling with calculations assuming that the Al-ions will be present on the Li sites in LCO. Furthermore, they proved that the degradation can thermally be reversed.[149,168] On the other hand, Tsai *et al*. showed a microstructural failure due to volume changes during (de)intercalation leading to high capacity degradation.[158] However, this cell had a much higher initial capacity of 1.5 mAh cm^{-2} at a current density of 50 μA cm^{-2} but after 100 cycles, the cell only retained 30% of its initial capacity. There are many ways in which researchers have tried to overcome the problems, either by using a mixed conductive layer at the interface with the cathode material,[169] a Nb interlayer as a modification of the interface of LLZO and cathode active material[152],

an additional polypropylene layer for protection,[170] or a $Li_{2.3}C_{0.7}B_{0.3}O_3$ (LCBO) interface between LLZO and LCO, which improved the cycling stability to 88% after 100 cycles, although they also used some modification with Li_2CO_3 on the LLZO and LCO side.[171] To some extent, all these studies use an additional layer between LLZO and LCO to avoid direct contact, proving that cell degradation can be minimized but not neglected. A completely different approach is shown by Ohta *et al*. who, instead of an additional interfacial layer, added a sintering additive (Al_2O_3 and Li_3BO_3) to reduce the sintering temperature to 790 °C, preventing the interdiffusion at high temperatures.[172] This is interesting as liquid phases typically promote interdiffusion.[102]

All-Solid-State Batteries with LLZO as solid electrolyte and LCO as active material are a promising and safe alternative for future battery technologies. Nevertheless, major problems are still limiting industrial application. The synthesis of LLZO is cost-expensive and requires high energy. On the other hand, composite cathodes have major performance issues, due to crack formation in the oxides and interdiffusion of different elements. Several of these problems will be addressed in the present work.

2.3 Recycling of Li-Ion Batteries

The previous two sub-chapters introduced the Li-Ion battery and the All-Solid-State battery, whereas here the focus will be on the recycling of these battery types. Given that All-Solid-State Batteries are still on a lab scale level and only a few are about to enter industrial production at present, recycling in industry is focused on LIBs. After an introduction to recycling in general, a brief discussion is provided of the various existing processes in LIBs. Subsequently, a short overview of recycling approaches in ASSBs is presented.

In LIBs, various valuable materials are being used. The seven most recycled components are graphite and Cu (foil) for the anode side and Co, Ni, Mn, Li, and Al (foil) for the cathode side. This applies to a typical design where NMC is used as the cathode active material. In the case of LCO as the cathode active material, Ni and Mn can be excluded from this list. The Global EV Outlook (2023) by the International Energy Agency[14] investigated the supply of Li, Co and Ni in comparison to the demand for these resources. While the supply of each material in 2022 was greater than the demand again, the crisis in 2021 demonstrated that for all of the above, demands can exceed supply already today. This intensifies the general scarcity of supply relative to demand, particularly with increasing demand in the future. For example, sufficient quantities of Li are available today, but forecasts indicate that recycling will be necessary if the deposit is not to be exhausted entirely.[173] Some forecasts even suggest that at least 90% of the Li must be recovered in order to manage the Li deposits in a sustainable manner.[174] A study from 2013 already predicted that Ni and Co would reach their global mining limits if battery production increased.[175] Recycling also promotes the sustainable production of electrical energy by using closed-loop material cycles, which can be enhanced by developing appropriate recycling technologies.[47] The EU directive follows the suggestions by clarifying clear goals of recycling by 2030, such as recycle batteries in total by 70%.[6]

Recycling strategies in general can be divided into direct recycling and indirect recycling. The latter can be further divided into three distinct categories, which can be combined with each other: high-temperature treatment (pyrometallurgical)[47,176], medium-temperature thermal treatment (pyrolysis)[177] and leaching instead of thermal treatment (hydrometallurgical)[7,47,177]. The following section will provide a more detailed description of each of these three types, explained by means of the example of LIBs.

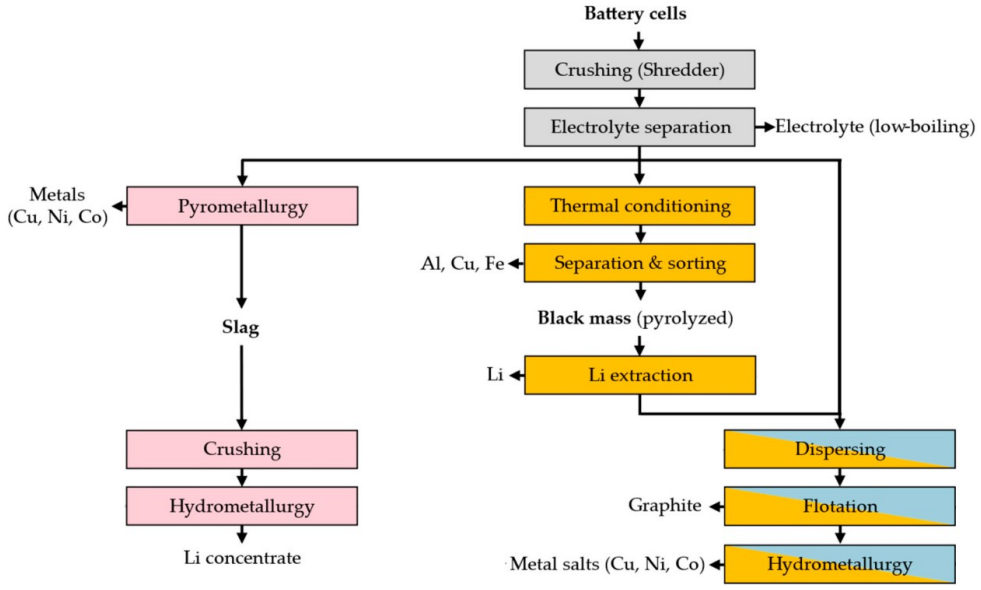

Figure 2.3.1: Different recycling ways of high thermal treatment, medium thermal treatment and no thermal treatment of LIBs. These processes are based on the InnoRec Process, adapted from [178] is licensed under CC BY 4.0 (https://creativecommons.org/licenses/by/4.0/).

2.3.1 Recycling approaches for liquid Li-Ion Batteries

Recycling processes that are currently in use in industry are for example a combination of pyrometallurgical and hydrometallurgical process (by Umicore)[179], a combination of pyrolysis, mechanical and hydrometallurgical process (ACCUREC) and a combination of mechanical and hydrometallurgical process (Duesenfeld).[178,180,181] The following section provides a detailed explanation of each process, each with its own benefits and disadvantages. Prior to the recycling steps, it is necessary to deactivate the battery system. The battery system is therefore dismantled to the cell modules, and deactivation occurs either by a full electrical discharge and subsequent short circuiting or by treatment in saline solution or by pyrolysis (>200 °C).[182,183] Only after this step, the actual recycling process begins.

The process as defined by Umicore represents a typical pyrometallurgical application within the industrial context. One advantage of this process is that it allows for the recovery of various types of batteries.[179] After dismantling of the cell, and removal of the plastic and metal housing parts, the cells are pyrolyzed at three different temperatures from 400 °C to 1450 °C.[179] During this process, Ni, Co and Cu are recovered in a metal alloy, while metals such as Al and Li are transferred into the slag phase.[184] The melting process can separate different LIBs elements, while high recovery rates (>95%) for Ni, Co and Cu have been observed.[182] Li, for example, can be also found in the flue dust, due to

evaporation.[178,184] All three, flue dust, metal alloy and slag, must undergo a subsequent hydrometallurgical step to obtain the reusable materials.[47,179]

Pyrolysis, a medium-temperature process, employs temperatures of up to 660 °C (the melting temperature of Al) under an inert atmosphere (Ar or N_2), with an attached exhaust gas filter. The process is employed for the treatment of organic-containing waste, whereby the organics are separated by evaporation and cracking, thus minimizing exothermal reactions and suppressing the melting of metal content (Al).[182,184] As previously stated, pyrolysis also allows to deactivate the battery cells under control.[182] The removal of organic components is of significant importance, as they negatively influence subsequent steps, such as hydrometallurgical processing or flotation.

During the flotation process, particles can be separated due to the differences in their wettability. The process is commonly employed in battery recycling to separate graphite from the cathode active material.[185] Thermal treatment steps result in burning and removal of the electrolyte, which could alternatively be recovered through liquid extraction, which is a complex and expensive process though.[178,186]

A recycling process that does not involve heat treatment is typically a combination of a mechanical step and a hydrometallurgical step. Whole Li-ion battery packs can be shredded, although there is a high risk of thermal runaway of the cells. Therefore, only discharged batteries are used in mechanical shredding. Furthermore, the process is conducted under an inert atmosphere.[7] The materials are then sorted based on their specific properties, *e.g.,* magnetism or density.[7,178] Mechanical processes are unable to produce material purities exceeding 95% for Co, Cu, and Ni, which is the reason why it is usually followed by a metallurgical step.[47,178] Even if mass fractions of 96% and higher were recovered by separating Al and Cu via pneumatic separation, this process is not suitable for cathode active material.[187]

Hydrometallurgy is a widely utilized process in battery recycling that employs low temperature aqueous phases, separated into three different steps: During the leaching process, metals are dissolved using acids and bases. Subsequently, a purification step is required to separate and purify each material, while the final recovery step completes the process. The leaching of shredded fractions, which have undergone mechanical treatment, comminution, or the leaching of slag and alloy materials, which have undergone high-thermal treatment, is achieved through the use of acids.[47] Acids that are typically employed in the leaching process are either inorganic, such as sulfuric acid, or organic, such as citric acid. Organic acids are often selected for their environmental friendliness.[188] The hydrometallurgical process allows for the recovery of materials with high quality and flexibility, and it is therefore the final step in battery recycling.[189,190]

In addition, it should be noted that different alternatives to the aforementioned recycling steps are currently developed in the field of recycling technology. Here, only the early-stage-lithium recovery (ESLR) will be mentioned, as this process has gained significant interest in the recycling of future battery technologies. In this process, Li is recovered prior to the aforementioned recycling routes by

utilizing water as a leaching medium. Subsequently, a co-precipitation with CO_2 is employed to recover Li_2CO_3.[191,192]

An alternative approach is the direct recycling route. In this process, the valuable materials are not separated and recovered in their elemental form; rather the components are recovered. Gaines *et al.* conducted an evaluation of the direct recycling approach in comparison to conventional recycling.[193] One example is the LFP cathode active material: While the value of recovered LFP material is \$0.75/lb, the cathode itself costs \$9.10/lb.[194] Some materials, especially cathode material, are cost-intensive to process due to their high embodied energy. The energy required for cathode production can be reduced by 50% by using re-functionalized cathode material in place of virgin materials.[195] Different direct recycling routes are available: The solid-state route[196] is used to re-lithiate cathode active material by combining cathode material with a solid Li source under thermal treatment.[195,197,198] The hydrothermal method[196,199] is a re-lithiation step as well, but based on a reductant and a Li source which are used in solution with the cathode active material. The eutectic medium method[196] is based on a eutectic solvent to first leach transition metals and regain the cathode active material afterwards *e.g.* for LCO and NMC.[200] Electrochemical regeneration[196] can be used to achieve the selective recovery of lithium and transition metals by an electric field.[201]

On the one hand, direct recycling has the advantage of avoiding the need for repeating the full production process, while on the other hand, hydro- and pyrometallurgical treatment are already well established in industry. The recovered elements can be utilized not only in battery production but also in a variety of other applications. In certain applications, the purity of the recovered elements is not necessarily a critical factor. This may make it sometimes worthwhile to engage in downcycling, as the effort to achieve high purity may not always be required.

2.3.2 Recycling strategies for All-Solid-State Batteries

The motivation for recycling of LIBs is analogous to that for ASSB recycling. The cathode material utilized in LIBs is similar to that employed in ASSBs, as the underlying principle is identical. Therefore, no new developments of recycling processes are required for the cathode site. The application of lithium metal as anode introduces a critical raw material, as it is used in a higher quantity than in LIBs. In addition to the aforementioned critical materials, Li, Ni, Co, Mn, and Cu, there are other materials that will be utilized in future ASSB technology. In the case of oxides, tantalum (Ta) and gallium (Ga) are also listed as critical raw materials, both of which are necessary dopants to increase the ionic conductivity of LLZO,[61] a focused battery material under oxide solid electrolytes.

A number of forecasts have been produced comparing the recycling of ASSBs, with the majority focusing on the three main groups: oxides, sulfides and polymers.[202] Schwich *et al.* developed a forecast of LLZO and $Li_{1+x}Al_xTi_{2-x}(PO_4)_3$ (LATP) electrolytes connected with LCO and NMC as cathode material, based on a global capacity production of 1 TWh per year.[32] In a recent publication, Ahuis et al. presented a comprehensive review of recycling strategies for ASSBs, categorizing them into polymer, sulfide, and oxide groups.[203] The review concluded that developing a cost-effective recycling route for polymers is challenging due to their low value. Furthermore, mechanical treatment is challenging due

to the high adhesion between the components.[203] Sulfide-based ASSBs exhibit a high reactivity in air and humidity, leading to the formation of toxic H_2S gas. Therefore, it is essential to develop recycling strategies under inert or dry atmosphere.[203] Additionally, the solid electrolyte becomes inactive in contact with air, which is contradictory to the recovery of the components. Oxides are as predicted by Doose *et al.* to be a ceramic material with a high hardness, resulting in specific requirements for mechanical treatments.[47,203] ASSBs have in common the use of a Li metal anode, which requires additional safety aspects, as it will form LiOH in contact with water, forming the gas H_2.[47] Here, the ESLR is suitable to minimize the effect of metallic Li immediately prior to recycling, increasing the safety of the entire recycling process. Nevertheless, a strategy must be developed for the use of ESLR with water on metallic Li, whereby the gas H_2 can be released in a careful manner.

In their study, Doose *et al.* proposed that the recycling of oxide-based ASSBs could result in a high cost when co-sintering electrode and separator due to the necessity for mechanical separation.[47] Consequently, they suggested that a pyrometallurgical process could become a more attractive option. While Schneider *et al.*[204] demonstrated the viability of a hydrometallurgical process by comparing different acid treatments on LLZO, leading to a solubility of 99% in strong acids, a direct recycling approach is being investigated for cathode material LCO[205], NMC[206], and solid electrolyte LLZO[9], a publication derived from the present work. Sloop *et al.* additionally investigated a complete LIB cell in a direct recycling approach on an industrially scalable process.[11]

The recycling of ASSBs is not yet sufficiently developed. However, initial experimental approaches have demonstrated that a direct recycling route is beneficial in many cases with the new cell design, especially when the embodied energy is high. Moreover, the metallic lithium may present a challenge during recycling, underscoring the necessity to develop early-stage lithium recovery techniques to ensure the safe recycling of ASSB.

3 Manufacturing and Characterization of All-Solid-State Batteries

3.1 Synthesis and Processing of $Li_7La_3Zr_2O_{12}$ and $LiCoO_2$-$Li_7La_3Zr_2O_{12}$

In this work two different processing routes for synthesis were used for LLZO with various dopings. After the powder preparation, the powder was used in a slurry to create green tapes via tape cast process. The green tapes were then sintered with various sintering temperatures and times, also indicated for each experiment.

3.1.1 Powder preparation

$Li_{6.45}La_3Al_{0.05}Zr_{1.6}Ta_{0.4}O_{12}$ with 10% Li excess (LLZO-10) and with 20% Li excess (LLZO-20) powder was synthesized by a solid-state reaction method.[72] Precursors such as La_2O_3 (99%, Merck, pre-dried at 900 °C for 10h), Ta_2O_5 (99.95%, Inframat), Al_2O_3 (99.82%, Inframat), Ga_2O_3 (99.995%, Alfa Aesar), ZrO_2 (99.7%, Treibacher), and $LiOH{\cdot}H_2O$ (98%, Merck) were used for the synthesis of LLZO. Furthermore, $Li_{6.45}La_3Al_{0.02}Zr_{1.6}Ta_{0.4}O_{12}$ (LLZO:Ta,Al), $Li_{6.5}La_3Zr_{1.6}Ta_{0.4}O_{12}$ (LLZO:Ta), $Li_{6.4}La_3Ga_{0.2}Zr_2O_{12}$ (LLZO:Ga), were synthesized with same precursors but without the solid state reaction. This will be explained in detail in chapter 4.2. In some experiments Li_2CO_3 (99%, Alfa Aesar) were used and will be indicated in the experiment itself.

The pre-synthesized LLZO powder was milled down to a suitable particle size for the slurry developed for the tape cast process (see Rosen et al. [107]). This was done in a planetary micro mill (Pulverisette P7, Fritsch) with 3 mm zirconia milling balls at a speed of 500 rpm for 240 minutes milling time, each 5 minutes and 25 minutes break time to cool down the solvent (ethanol, 97%, Hoffmann – Schmittmann GmbH). In the course of the present work, an optimized milling procedure was developed by using a ball mill (E_{MAX}, Retsch) at a speed of 1000 rpm for 15 minutes with 1mm zirconia milling balls in the same solvent. The resulting particle size distribution of LLZO-10 and LLZO-20 can be seen in **Figure *3.1.1***. The solvent removal of the milled powder was performed in a drying step in an N_2 atmosphere at 60 °C for 12 hours.

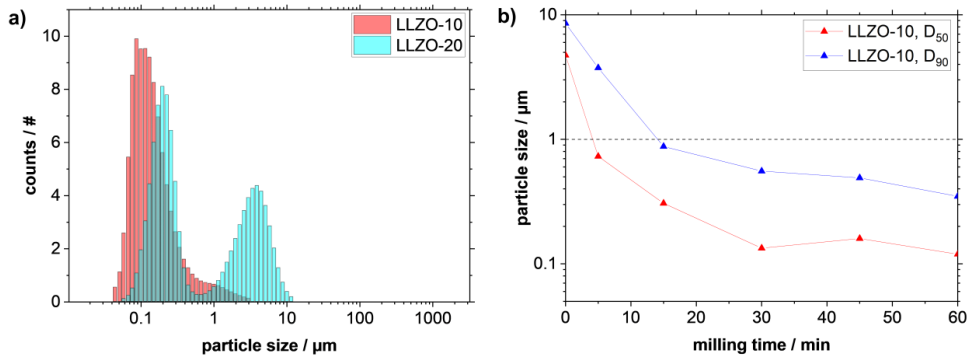

Figure 3.1.1: a) Particle size distribution of LLZO-10 powder and LLZO-20 powder with optimized parameters. **b)** Particle size distribution D_{50} and D_{90} value for different ball-milling times for LLZO-10 powder.

The LCO powder (99.5%, MSE Supplies) was milled down in a planetary micro mill (Pulverisette P7, Fritsch) with similar milling parameters as above. The resulting milled cathode active powder was dried on a hot plate at 70 °C overnight to remove any residual solvent.

In the following work, a direct recycling route will be evaluated on real waste material. For this approach, LLZO-10 powder which had been used in several heat treatments and stored in air for up to four months, is further named LLZO-p. In a parallel approach, LLZO-10 powder was processed to a green tape (following the process described in 3.1.2) and also stored for up to four months in air. This aged LLZO-10 green tape is crushed manually and named LLZO-t green tape. For re-synthesis in the tape-cast process, the original source must be in powder form. Therefore, the manually shredded green tapes were additionally heated at 600 °C for 2 hours in an alumina crucible with a closed lid. This heat treatment removed the organic matter, the resulting powder is named LLZO-t powder. The LLZO-t powder was then wet-ball milled to the adjusted particle size (see **Figure 3.1.2**), as previously described with a Pulverisette P7.

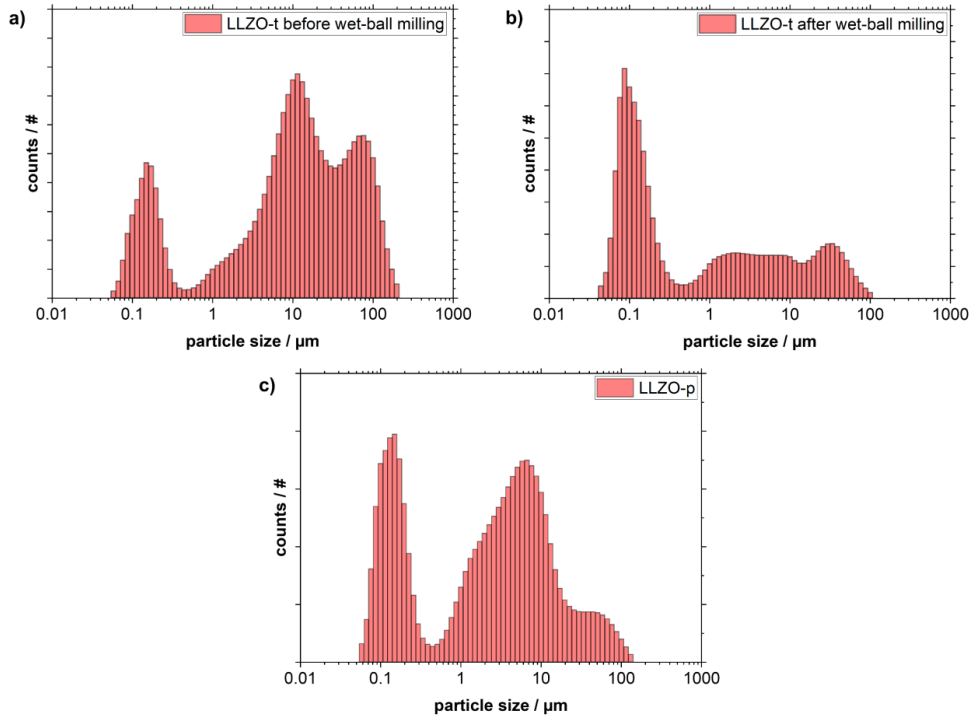

Figure 3.1.2: Particle size distribution of the LLZO waste material. LLZO-t powder **a)** before wet-ball milling, **b)** after wet-ball milling and **c)** LLZO-p powder, adapted from [9] is licensed under CC BY 4.0 (https://creativecommons.org/licenses/by/4.0/).

Furthermore, in chapter 4.2, a new route is developed. For this approach, different powders were needed. The precursors for the new *in-situ* synthesis route are comparable to the approaches previously demonstrated in this work and in the literature.[107,108,159] The oxide precursors LiOH, La_2O_3, and ZrO_2 and – depending on the dopant – Ta_2O_5, Al_2O_3 and Ga_2O_3 are used to synthesize either LLZO:Ta,Al with the stoichiometry $Li_{6.45}Al_{0.02}La_3Zr_{1.6}Ta_{0.4}O_{12}$, LLZO:Ta ($Li_{6.5}La_3Zr_{1.6}Ta_{0.4}O_{12}$) and LLZO:Ga ($Li_{6.4}Ga_{0.2}La_3Zr_2O_{12}$). A Li excess of 10 % is considered for LLZO:Ta and LLZO:Ta,Al and of 5 % for LLZO:Ga synthesis.

3.1.2 Tape-casting

The organic solution was prepared by mixing the following materials: 5 g binder (PVB98, Sigma Aldrich), 2.5 g dispersants (DISPERBYK180, BYK), 2.5 g each plasticizers (PEG400, Sigma Aldrich and Tri(ethylenglycol)bis-2-ethylhexanoate, Solutia Inc.) and solvents (between 5 g and 7 g) for 10 g of powder. Due to a change in the process, either an azeotrope of 66% Methylethylketon (MEK) and 34% Ethanol (97%, Hoffmann – Schmittmann GmbH) or only Ethanol is used. The organic solution was mixed on a rolling bench for 24 hours before usage. Storage of this organic solution is assumed to have no influence on the resulting tape.

For the creation of free-standing single layers up to 100 µm thickness of LLZO, the milled LLZO powder or the milled precursor powder was mixed and homogenized with the organic solution in a mixer (Thinky) with a speed of 1500 rpm for 2 minutes. The slurry was immediately poured onto mylar foil on the tape cast bench with a gap size of 350 µm with a velocity of 30 mm s^{-1}.

For the composite cathode green tapes, the same organic solution was used. Milled LCO powder and milled precursor powder were mixed with the organic solution to a slurry in a mixer (Thinky, see above). Depending on the green tape requirements a single layer was cast (350 µm gap, mixture of precursors:LCO, 1:1 wt%) or a tri-layer was cast. Here, precursors:LCO ratios of 2:1 wt%, 1:1 wt%, 1:2 wt% were mixed with the organic and sequential tape cast with a gap size of 180 µm, 220 µm and 240 µm, respectively. The tape casting was started with the precursor-rich slurry. Between each layer, a drying step of 5 minutes was added previously to the next tape casting.

The resulting green tapes were dried in air at room temperature for 14 hours (MEK:ethanol) or for 5 hours (ethanol).

The dry green tapes were then placed in a warm press (P/O/Weber GmbH) at 80 °C and a pressure of 3 kN cm^{-2} (30 MPa) for 2 minutes (16 kN cm^{-2} (160 MPa) for 2 minutes, for composite cathodes) to densify the green tape. The resulting tapes were punched with 12 mm (separator and composite cathode), 14 mm (separator) diameter round molds.

3.1.3 Sintering

The resulting green tapes, already shaped into circular tapes with varying diameters need to undergo a de-binding step to remove organics and a sintering step.[98] Warm pressed green tapes were placed in an alumina crucible for sintering. There are two different attempts for the material choice between the green tapes and the underlying crucible to minimize contact and minimize uptake of Al. One is a magnesia with a thickness of 5 mm and on top LLZO powder and additionally LLZO pellets with a similar diameter as the green tapes, cut into 1 mm thick pellets. The green tape was placed between two pellets to suppress deformation during sintering. Sintering on LLZO was not possible without destruction due to the formation of sintering necks between pellet and green tape, leading to adhesion and fractured tapes. A more optimized way to suppress deformation was by using a different sintering approach, adding a de-binding step to the whole process. This led to the possibility of a slightly different structure in the crucible. Magnesia plates were still placed in the crucible first, by adding LLZO powder, evenly distributed with a smooth surface secondly. On top of these the LLZO green tapes were placed for sintering with a closed lid. For mixed cathode green tapes, the approach is similar but the LLZO powder on top of the magnesia plate is mixed with 50% of LCO powder. A schematic structure of the crucible before and after optimization can be seen in the following **Figure 3.1.3**.

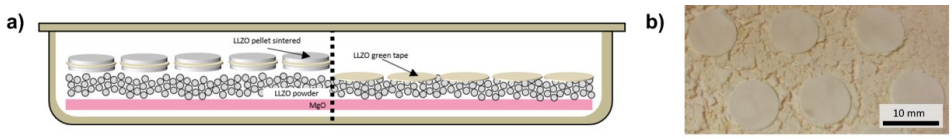

Figure 3.1.3: a) Scheme of crucible during conventional (left) and optimized (right) sintering, by removing the LLZO pellets and sintering only on LLZO powder bed, resulting in **b)** sintered flat LLZO tapes.

The crucible filled with the green tapes and powder bed is placed in an oven and sintering takes place in air. Different approaches were used here: A direct heating to the final sinter temperature, indicated in each experiment with a dwell time (e.g. 1175 °C, 5 h) includes the heating of 5 K min^{-1} and similar cooling rate. The second optimized sintering way, uses holding steps for moisture and de-bindering; here with a ramp at 5 K min^{-1} up to 200 °C, holding the temperature for 1 hour and then heat with a ramp of 10 K min^{-1} to 650 °C to burn the organics, where the dwell time is 2 hours or without the step at 200 °C, immediately ramping up to 650 °C. Finally, the temperature is ramped up with 10 K min^{-1} to the final temperature, indicated in each experiment, and hold there for the indicated time. Cooling always occurs with a ramp of 5 K min^{-1}. The resulting three sintering profiles are displayed in the following **Figure 3.1.4**.

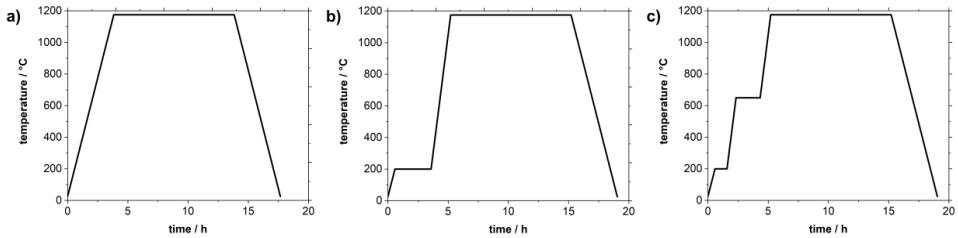

Figure 3.1.4: Sintering temperature profile: **a)** immediately reaching sintering temperature, **b)** adding one holding-step before reaching sintering temperature and **c)** adding two holding-steps for moisture and de-bindering before reaching sintering temperature.

3.1.4 Cell assembly

The resulting tapes are supposed to be investigated in a battery cell setup. This implies that LLZO separators are used to build a symmetrical cell, applying Li metal on both sides of the separator (Li|LLZO|Li). The LLZO sintered tape surface was cleaned by heating the tapes in an alumina crucible in an argon atmosphere at 750 °C for 2 hours (at a ramp of 5 K min^{-1}) and afterwards stored in an argon atmosphere. A thin Au current collector, serving here by forming an alloy with Li metal later on, was sputtered onto the surface (5-15 nm, Cressington 108 auto coater). The alloy positively influences the wetting of the Li metal to the LLZO.[126,130] Li metal was freshly calendared and carefully placed on top and below the LLZO tape. The whole stack was heated to 300 °C on a hot plate to melt the Li and attach it to the surface. The cell was surrounded by Ni plates as current collector and transferred into a Swagelok cell and electrochemical measurements were carried out.

For composite cathodes, a full-cell setup was established to investigate the electrochemical response. A thin Au current collector was applied on the LCO-rich side of the composite cathode tape by sputtering (see above). The non-sputtered sides, with the LLZO-rich side were coated with a polymer (PEO, M:600000, Sigma Aldrich; LiTFSI, Sigma Aldrich; conductive carbon, Alfa Aesar; in acetonitrile, Roth; the ratio of PEO:LiTFSI was 1:20; 20µm thick, Eppendorfer pipet). The polymer on top of the cathode was dried for 5 hours at room temperature in an argon atmosphere. LLZO pellets were used as separators (fabricated as stated by Scheld *et al.*[207]). The pellets were polished with 4000 grit SiC paper to remove surface contaminations. Li metal was freshly calendared and was manually pressed on the LLZO pellet and heated to 300 °C for 5 minutes to melt the Li and increase the contact. The composite cathode attached to the polymer and the separators attached to the Li metal, was stacked on top of each other, while the polymer acts as connection between both ceramic components. The cell is transferred into a Swagelok cell, surrounded by a Ni plate on each side and electrochemical measurements were carried out.

3.2 Materials Characterization

3.2.1 Particle Size Distribution

Static laser diffraction is a technique employed to determine the dimension and distribution of particles within a powder. In this method, particles are dispersed in a liquid or gas and then passed through a laser beam. Subsequently, the scattered light is collected and analyzed by detectors. Diffraction also occurs, resulting in point-like diffraction patterns for real particles, which are irregular in shape. Two models are typically employed to interpret the signals recorded by the detectors: The Fraunhofer and Mie models. In this study, Mie theory was employed because it is frequently utilized for smaller particles (< 1 µm in this work), and considers diffraction, refraction, absorption, and emission of laser light. Mie theory offers a great accuracy in particle size determination, particularly in the lower micrometer range when evaluating real particles with non-ideal spherical shapes.

The particle size distribution was determined by using a Retsch LA950 instrument, utilizing ethanol as the liquid medium. Ultrasound was employed to destroy the agglomerates, enabling the measurement of the primary particle size was measured.

3.2.2 X-Ray Powder Diffraction

X-Ray powder diffraction (XRD) is used to reveal the structural properties of materials. The technique is based on the diffraction of x-rays penetrating in the lattice structure of the material, based on its unit cell. X-rays are being diffracted by the periodicity of this unit cell, while only some diffracted x-rays exhibit a constructive interference. Each atom in the lattice results in a specific scattering angle, depending on the material (**Figure 3.2.1**) and can be calculated by Braggs Law, see equation **3.1** below[208,209]:

$$2d \cdot sin(\theta) = n\lambda \qquad \textbf{Eq. 3.1}$$

Where d is the spacing between atoms/planes, Θ the incident angle, n an integer and λ is the wavelength of the x-rays.[71]

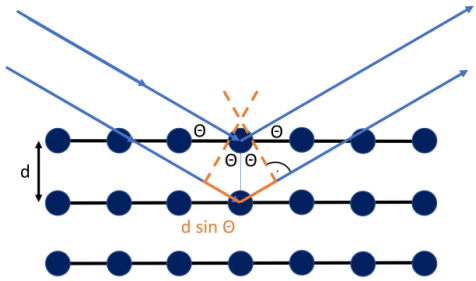

Figure 3.2.1: Scheme of x-rays penetrating into the material and be diffracted by the atom in the lattice. Braggs Law can be illustrated by this, adapted from [71].

In this work, a Bruker D4 Endeavour instrument using Cu-Kα radiation and equipped with a 1D detector LYNXEY and a DIFFRACplus BASIC package, which was released in 2009, was used to analyze the phase compositions of the powders, green tapes and sintered tapes. The standard measurement program with the following parameters were used: range of diffraction angle 10° to 80° 2Θ, with an increment of 0.02° for 2Θ and 0.75 seconds per measurement step. In one single measurement (**Figure 4.2.5**) an Empyrean (Malvern Panalytical, Almelo, Netherlands), using a 255-channel PIXcel linear detector from 10° to 90° 2Θ in 0.026° steps was used. A Rietveld analysis was performed with the software TOPAS (Bruker).[210]

3.2.3 Scanning Electron Microscopy

Microstructural analysis was performed by Scanning electron microscopy (SEM), which is a surface sensitive technique, by using a focused electron beam, to scan the surface. An electron gun generates primary electrons and they interact with the atoms near the surface, being scattered. Scattering can lead to different types of *e.g.* electrons (secondary electrons and backscattered electrons) or x-rays, photons *etc.* Depending on the detector information, topography or composition can be investigated. Backscattered electrons (BSE) can for example give information about the composition, while energy dispersive x-rays are used for elemental investigation, as they are characteristic for each element (EDX measurement). Furthermore, to gain information about the crystallographic orientation, and grain boundaries the sample needs to be tilted to 70° for electron backscatter diffraction (EBSD). With this tilt, the sample produces diffraction bands, which are also called Kikuchi patterns. A scheme of an electron beam directed on the surface is displayed in **Figure 3.2.2**.[211]

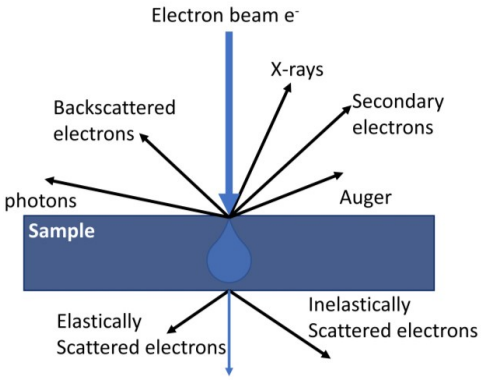

Figure 3.2.2: Principle of an SEM of an electron beam directed on the sample and its interaction, adapted from [212].

Different instruments were used for the sample analysis in this work. In chapter **4.1.4** SEM images were taken using a field emission scanning electron microscope (Merlin, Carl Zeiss Microscopy), equipped with the X-Max Extreme EDX-detector (Oxford Instruments). Chapter **4.2.3** used the SEM instrument (SEM, Zeiss Gemini 450), equipped with a secondary electron (SE) and backscattered electron (BSE) detector and an EDX detector (ULTIM MAX 170, OXFORD INSTRUMENTS). The electron acceleration voltage was set to 8 kV, except for the overview of the full cathode (**Figure 4.2.7**) it was set to 15 kV. The combination of SEM and Raman technology was performed on an EVO 15 (Zeiss) using an BSE detector together with an EDX detector (ULTIM MAX 100, OXFORD INSTRUMENTS) with an accelerating voltage was set to 15 kV. All other investigations were performed by a HITACHI TM3000 instrument in back scattering mode with a 15kV beam accelerating voltage.

Sample preparation varied for each investigation. For fractured, un-polished samples, no necessary steps previously to the measurement needed to be taken care of. For sintered tapes with a polished cross-section, the tapes were embedded in epoxy resin, ground by SiC paper, and polished with a water-free diamond suspension. After the final step a thin gold layer (<10 nm, Cressington 108 auto coater) for measurements on the Hitachi instrument or a thin platinum layer (<10 nm, Baltec, type SCD 050) for measurements on the Zeiss instrument was sputtered on top. Powder samples were prepared on a Si wafer, placed with pure ethanol, dried and coated with platinum (<10 nm, Baltec, type SCD 050).

The images in chapter **4.1.4** were prepared by Ar-ion milling (3 kV acceleration voltage, 380 µA discharge current) using a flat milling system (IM-3000, Hitachi). A thin iridium layer was sputtered onto the sample surface to compensate for charging effects (Q150TS coater, Quorum).

EDX was performed on the same instrument state above (SEM, Zeiss Gemini 450) using a secondary electron (SE) and backscattered electron (BSE) detector and an EDS detector (ULTIM MAX 170, OXFORD INSTRUMENTS). The EDX measurement related to Raman was performed on an EVO 15 (Zeiss) using an BSE detector together with an EDX detector (ULTIM MAX 100, OXFORD INSTRUMENTS) with an accelerating voltage was set to 15 kV.

EBSD measurements were performed on the instrument (SEM, Zeiss Gemini 450) using a secondary electron (SE) and backscattered electron (BSE) detector and an EBSD detector (C Nano, with the software Aztec, OXFORD INSTRUMENTS).

Sample preparation was followed as explained by Fu *et al.*[213], due to the highly surface sensitive measurement and the fast degradation of LLZO in air.

3.2.4 Grain Size Distribution

SEM images were used to evaluate the grain size distribution of sintered tapes. This was performed on a cross-section of a fractured sample, un-polished, to see the visible grain boundaries due to intergranular breaking of most of the grains. It is not possible to polish the cross-section of thin tapes and do a chemical or thermal treatment to make grain boundaries visible, due to the fragility of the tapes. Although un-polished cross-sections distort the real grain size, it is the best possible assumption and was applied to get a quantitative grain size distribution in the different samples. Therefore, the following steps were performed in the ImageJ software[214]. The resulting images are pictured in **Figure 3.2.3**. The SEM images were used to analyze the grain size distribution by setting a threshold, using the 'watershed' program and manually adjusting those grain boundaries that were assumed falsely by the program, and converting them finally into ellipses with a specific value on the long and short axis. The value for the long axis was used as maximum grain size and plotted. For the Gaussian fit, the chi-tolerance value of 1×10^{-9} was realized in the software Origin.

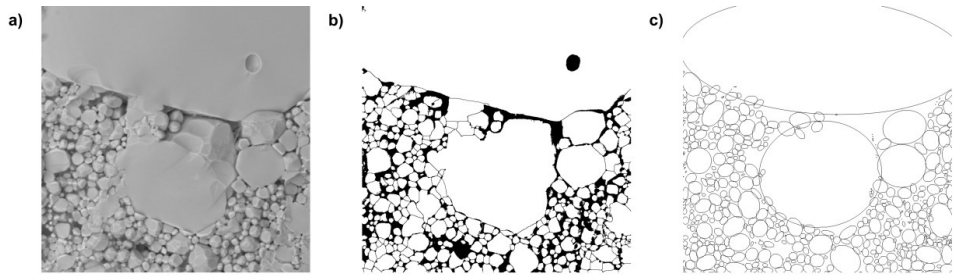

Figure 3.2.3: Grain size distribution analysis by ImageJ showing **a)** the SEM image used, **b)** the converted picture in ImageJ, manually adapted the grains if necessary and **c)** the resulting ellipses used for calculation of the grain sizes.

3.2.5 Density

Density measurements can be performed in various ways, *e.g.* calculating on the geometry, using Archimedes principle or by analysis of a cross-section image. Due to the low weight and highly deformed tapes during synthesis, both first cases are not applicable for investigation of the density of the sintered tapes. Therefore, the only possibility is an image analysis. Due to the evaluation of different grain sizes and the problematics of the polished cross-sections explained in the previous section, no polished cross-sections were examined for density measurement, as it is usually done by setting a

threshold in the ImageJ software.[214] Here, density measurements were performed in the same tape on three different areas: 1) On a polished cross-section, 2) on cross-sections fractured, the latter with intragranularly fractured grains and intergranularly fractured grains to see the difference in density measurement depending on the preparation, assuming that the real density is homogenously in the tape.

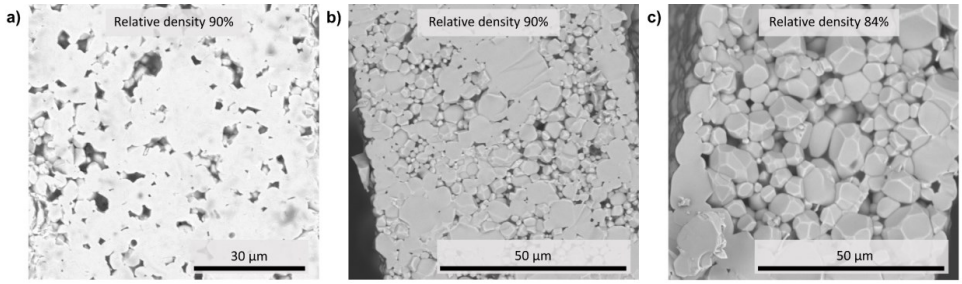

Figure 3.2.4: SEM images of a **a)** polished cross-section **b)** an un-polished cross-section with intragranularly fractured surface and **c)** an un-polished cross-section with intergranularly fractured surface and their specific density, calculated by ImageJ.

The three different images reveal that between a polished cross-section and an un-polished cross-section with intragranularly fractured grains no differences can be seen in the relative density of the tape. The difference to the un-polished cross-section with intergranularly fractured grains is around 6% lower than the other relative densities. Therefore, the density is usually higher than the calculated value if the density of an intergranularly fractured surface is used. Therefore, the values based on intergranularly fractured areas are only used for an indication on the relative density of the tape.

3.2.6 Raman

Raman measurement were carried out to investigate the local chemical order of a sample. The sample is illuminated by a monochromatic light, here a laser source, and photons are excited from a vibrational energy state to a virtual energy state. The photon can than emit either in elastic light scattering (Rayleigh) or inelastically (Raman). For Raman scattering, the frequency is either increases or decreases resulting in a Stokes or Anti-stokes shift[215]:

(i) Rayleigh line with frequency $\nu = \nu_o$

(ii) Antistokes Raman line with frequency $\nu = \nu_o + \nu_V$

(iii) Stokes Raman line with frequency $\nu = \nu_o - \nu_V$

With ν = frequency, ν_o = initial frequency and ν_V = specific frequency of any value. A schematic of the emitted photons can be seen in **Figure 3.2.5**.[215]

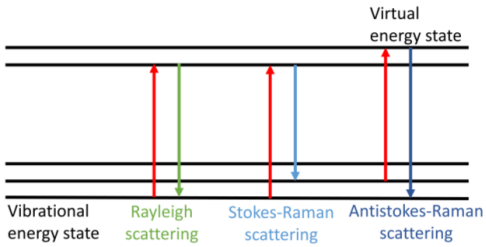

Figure 3.2.5: Schematic drawing of the light emitted, with indication of Rayleigh lines, Stoke-Raman Lines and Antistokes-Raman lines, adapted from [216].

To be Raman active, the sample needs to undergo a vibrational or rotational mode leading to a change in polarization. Then the Raman spectrum can be used to identify inorganic solids, due to their differences in vibrational spectra.[215] Further optimization can enhance the intensity of the inelastically light scattering, for example surface-enhanced Raman scattering.[215]

Raman spectroscopy was measured with an INVIA QONTOR, RENISHAW with a 532 nm laser (~2.5 mW) and a 2400 l mm^{-1} grating installed. The spectra were collected with a step size of 1 µm in x- and y-direction and a measuring time of 1 s per spectrum. The spectra were processed with the WiRE software, including cosmic ray removal and normalization, and the mappings were averaged to a single spectrum, or a phase analysis of the mapping was performed. Due to the sensitivity of LCO and LLZO to the light, the power was set to 5%.

3.2.7 Time-of-Flight Secondary Ion Mass Spectrometry

Time-of-Flight Secondary Ion Mass Spectrometry (TOF-SIMS) is used to evaluate the surface-sensitive chemically related information and is a destructive technique. A pulsed ion beam bombards the sample surface and sputters secondary ions from it. The measurement is based on the ratio of mass to charge of the ionized elements, as its duration to hit the detector depends on it. Therefore, the required time to hit the detector can be related to the mass-charge ratio. This technique can detect the whole periodic table.[209,217]

The measurements were performed on a TOF-SIMS 5 NCS system (IONTOF GmbH) equipped with a Bi Nanoprobe 50 primary ion gun, an oxygen sputter gun, and a low-energy electron flood gun for charge compensation. Bi^+ primary ions were chosen for analysis at an energy of 30 keV, and the oxygen sputter gun operated at 1 keV. Images were taken in positive polarity in an analysis raster of 50 µm × 50 µm and 1024 × 1024 pixels in imaging mode, while the sputter raster was set to 350 µm × 350 µm.

3.2.8 Micro x-ray tomography

To assess the microstructure of the composite cathode on a large scale, micro x-ray tomography (µCT) measurements were performed. The used tool was a Zeiss Xradia Versa 520. Smaller pieces were needed

for the measurement, therefore, composite cathode tapes were cracked into pieces (< 10×10 mm) and fixed on top of a thin metal needle. The x-ray source was set to an acceleration voltage of 60 kV and a power of 5 W while using 40x optical magnification, resulting in a voxel length of 300 nm. Image quality was ensured through high exposure time of 35 s per image, leading to an overall measurement time of roughly 30 hours. An initial warmup step ensures that the sample has a constant temperature during the tomography. The chosen parameter set provides high-quality images with good contrast. This lowers the number of post-processing steps to just one non-local means filter, which was implemented in the 2023 distribution of GeoDict (GeoDict software, Math2Market, Germany, release 2024). Finally, Otsu's method is chosen as the segmentation algorithm. Microstructural evaluation was also performed with GeoDict 2023, using the MatDict and PoroDict modules. Initially, the phase distribution of active material and electrolyte is analyzed using MatDict. In the second step, pore connectivity is quantified in PoroDict.[218]

These measurements were performed by Adrian Lindner, IAM-ET, Karlsruhe Institute of Technology.

3.3 Electrochemical characterization

Electrochemical characterization methods are necessary to assess the performance of separators and composite cathodes in more detail. Therefore, cells, (symmetric half cells with two attached lithium anodes in order to characterize separators and full cells with lithium anode and composite cathode for composite cathodes) are analyzed with varying methods. To investigate the resistance of either separator or full cell, electrochemical impedance spectroscopy is performed on both type of cells. Another characteristic for separators is the critical current density for dendrite formation, while for full cells charge and discharge behavior are analyzed to evaluate the capacity of the composite cathode.

3.3.1 Electrochemical Impedance Spectroscopy (EIS)

Electrochemical Impedance Spectroscopy (EIS) is one of the most used technique to analyze the resistance in a battery cell. It provides information of the bulk resistance, the impedance of interfaces and charge-transfer reactions. EIS works with Alternating Current (AC) with a low amplitude over a high frequency range. When AC is applied to a battery cell, the impedance (Z) can be explained following Ohm's law for AC:

$$Z(\omega) = \frac{E_t}{I_t} \qquad \textbf{Eq. 3.2}$$

with the excitation signal of the voltage (E_t) and the current response signal (I_t), while ω is the angular frequency with $\omega = 2\pi f$, with frequency (f). Excitation signal and current response to a shift in phase (φ) can be described by the following equations:

$$E_t = E_0 \sin(\omega t) \quad \textbf{Eq. 3.3}$$

$$I_t = I_0 \sin(\omega t + \varphi) \quad \textbf{Eq. 3.4}$$

Inserting the above equations into Eq. 3.2 by displaying complex exponential functions (Euler's equation) gives a real component (Z') and imaginary component (Z'').

$$Z(\omega) = \frac{E_0 \sin(\omega t)}{I_0 \sin(\omega t + \varphi)} = Z_0 \frac{\sin(\omega t)}{\sin(\omega t + \varphi)} = Z' - jZ'' \quad \textbf{Eq. 3.5}$$

Typically for representing battery cells, a Nyquist plot is used, which plots the real component (Z') against the negative imaginary component (Z''), resulting in separate points for each frequency, although the frequency is hidden in the plot. To investigate the different contributions, *e.g.* resistance to the battery cell, equivalent circuit models are used to describe each electrochemical process/component. The electrical components, such as resistors (R), capacitors (C), inductors (L) and constant phase elements (Q_{CPE}) are most common in battery analysis. The fundamental electrochemical elements can be described as following:

$$resistance\ (R): \quad Z = R \quad \textbf{Eq. 3.6}$$

$$capacitors\ (C): \quad Z = \frac{1}{j\omega C} \quad \textbf{Eq. 3.7}$$

$$inductors\ (L): \quad Z = j\omega L \quad \textbf{Eq. 3.8}$$

$$constant\ phase\ element\ (Q_{CPE}): \quad Z = \frac{1}{Q(j\omega)^{\alpha}} \quad \textbf{Eq. 3.9}$$

with $\alpha = 1$ for an ideal capacitor, $\alpha = 0$ for an ideal resistor, and $\alpha = -1$ for an ideal inductor. A pure diffusion process would be described by $\alpha = 0.5$ and is also called Warburg diffusion. It is neglected in this work though.

The Nyquist plot for each of the above electrochemical elements would show different properties, *e.g.* an ideal capacitor would only be a direct line in $-Z''$ direction. The combination of these elements is displayed in individual semi-circles for each battery cell, depending on the resistance of bulk material, grain boundaries and interfaces. A Nyquist plot with an equivalent circuit model for a typical battery cell is shown in **Figure 3.3.1**.

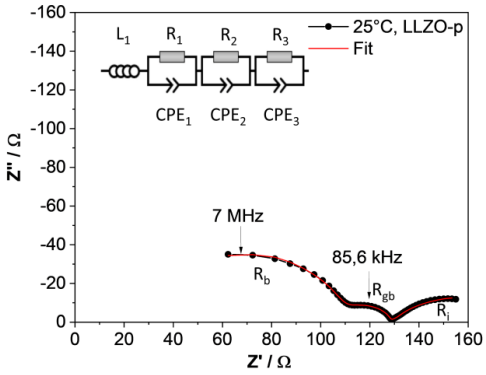

Figure 3.3.1: Example of a Nyquist plot with equivalent circuit model on real data adapted from [9] is licensed under CC BY 4.0 (https://creativecommons.org/licenses/by/4.0/).

The Nyquist plot shows three R-CPE elements, previously of an inductance, resulting in three semi-circles. By extracting the underlying parameters from the semi-circles, resistances and capacitance can be extracted. The capacitance cannot be used from the CPE element as extracted and need to be converted to obtain the effective capacitance[219]:

$$C = \frac{(Q \cdot R)^{\frac{1}{\alpha}}}{R} \qquad \textbf{Eq. 3.10}$$

In accordance with the recommendations set out by Irvine *et al.*[220], the value of the measured capacitance provides insight into the potential underlying phenomenon, as summarized in **Table 3-1**.

Table 3-1: Typical capacity values and their responsible phenomenon taken from[220]

Capacitance / F	***Responsible phenomenon***
10^{-12}	Bulk
10^{-11}	Minor, second phase
$10^{-11} – 10^{-8}$	Grain boundary
$10^{-10} – 10^{-9}$	Bulk ferroelectric
$10^{-9} – 10^{-7}$	Surface layer
$10^{-7} – 10^{-5}$	Sample/electrode interface
10^{-4}	Electrochemical reaction

It is assumed that LLZO has a low electronic conductivity of 10^{-10} S cm^{-1} [221], which is neglected. The ionic conductivity can then be calculated with equation **3.11**:

$$\sigma = \frac{L}{(R_b + R_{gb})A} \qquad \textbf{Eq. 3.11}$$

where σ is the ionic conductivity (S cm^{-1}), L the height of the sample, A the area, and R_b and R_{gb} the resistances of the bulk material and grain boundary.

Electrochemical tests in this work were carried out at either 25 °C or 60 °C by using a VMP-300 multi-potentiostat (BioLogic Sciences Instruments Ltd, France) combined with a climate chamber (Vötsch Industrietechnik VT 4002EMC, Germany). The data were evaluated using the EC-lab software (BioLogic Sciences Instruments Ltd, France) and Data Analysis (Z-View, Scribner Associates Inc.). Electrochemical impedance spectroscopy (EIS) was performed at 3.0 V in a frequency range of 3 MHz to 10 Hz with an amplitude of 10 mV.

3.3.2 Critical Current Density

Another important factor for a working separator is not only the high ionic conductivity at room temperature, but also the critical current density (CCD) of the separator. The critical current density describes the stability of LLZO against stripping and plating of Li metal in direct contact. CCD depends on many factors besides temperature, especially ionic conductivity, dendrite formation, and electrochemical stability, while other factors are related to the three mentioned above, e.g. relative density, mechanical strength, and interfacial resistance.[222]

To investigate dendrite formation, impedance and critical current density measurements were conducted at 60 °C using a BioLogic VMP-300 multi-potentiostat. The lithium was stripped and re-plated for this test at an increasing current density. It started from 5 µA (9.94 µA cm^{-2}) for 30 minutes per step with an increment of 5 µA per cycle for LLZO-t measurement (**Figure 4.1.28 b**), while for LLZO-p (**Figure *4.1.28* a**) reaching 50 µA (99.4 µA cm^{-2}), the increment was increased by 15 µA per cycle instead of 5 µA. Here, the critical current density is defined to be reached when the first Li dendrite grows by observing a significant voltage drop.

3.3.3 Cyclo-Voltammetry

Galvanostatic cycling was carried out at 35 µA cm^{-2} in a voltage window of 3.0 – 4.0 V vs. Li/Li^+. The battery was charged to a constant voltage of 4.0 V vs. Li/Li^+ until the current dropped to 13 µA cm^{-2}. The data were evaluated using the software EC-lab (BioLogic Sciences Instruments Ltd, France) and Data Analysis (Batalyse GmbH, Germany).

4 Results and Discussion

Based on the state of the art overview in chapter 2.2.3, several aspects have been identified where further research regarding the use of LLZO in ASSB is needed. The present chapter will address approaches to the following three key challenges:

- Consumption of critical resources
- Energy intensity
- Production cost

The first point will be discussed in the following sub-chapter 4.1, where the focus will be on recycling options of reject streams that occur within the production process to minimize waste production. A potential remedy for the other two issues, high energy requirements and production cost, will then be presented in sub-chapter 4.2, by introducing a new *in-situ* synthesis route.

4.1 Part I: Recycling of the solid electrolyte $Li_7La_3Zr_2O_{12}$

Recycling is important for a number of reasons, including the scarcity of resources for the materials used[8] which was identified as an issue related to LLZO. Furthermore, EU-Regulations defined a recycling rate for several crucial materials, including Li to be as high as 35% and for total battery recycling to be as high as 65% by 2025.[6] However, waste material is not only generated at the end of life, but also during the production process. At an industrial level, the waste production of a new battery manufacturing facility can be as high as 90% of the total output in the first year and also represents a challenge beyond the ramp-up phase.[223] Of particular interest for recycling due to the scarcity of resources for the materials used in LLZO are Li and various dopants such as Ta and Ga. Typically, a costly and time-consuming hydro- or pyrometallurgical approach (or a combination) is used to recycle the oxide materials and their dopants.[204] In order to minimize costs, a different approach of a direct recycling of production reject streams would help enormously to minimize the ecological footprint of oxide materials, as well as the high processing cost.[8] Particularly a non-destructive way of recycling production waste would lead to much lower recycling costs. Furthermore, the need to repeat a multitude of processing steps would be eliminated, saving energy, time, production capacity and ultimately again cost.

In this chapter, the focus is hence not on conventional recycling of end-of-life products, but rather on the recycling of production reject streams within the manufacturing plant. As large industrial LLZO production does not exist to date, the following findings are based on lab scale in research. This approach allows to anticipate potential issues in industrial production at a very early stage and to develop countermeasures and optimized processes ahead of time. The production waste is therefore mimicked

by purposefully producing waste material, and options for re-lithiation are investigated with regard to their influence on the final product and potential side effects. As a consequence, a direct and simple recycling route for in-production LLZO waste material was developed, with considerably lower energy consumption and cost than a pyrometallurgical or hydrometallurgical approach.

4.1.1 Preparation of $Li_7La_3Zr_2O_{12}$ waste production material for re-lithiation

To investigate potential recycling approaches for reject material caused by LLZO process malfunctions, this scrap material needs to be synthesized as a first step, as industrial waste output is not yet available for research. The most common impurity of LLZO is the Li-poor $La_2Zr_2O_7$ pyrochlore phase[224–226], which would occur during a malfunction in the process. It prevents LLZO from reaching its full ionic conductivity[227] and can be expected to play a crucial role also in industrial processes in the future. LLZO ($Li_{6.45}La_3Al_{0.05}Zr_{1.6}Ta_{0.4}O_{12}$) was synthesized in a solid-state reaction following the steps reported by Mann *et al.*[72] As detailed in chapter 2.2.3, Li-loss is a major drawback of the heat treatment which becomes necessary due to the formation of Li_2CO_3 during the milling step. Excess Li is usually used to overcome Li loss during heat treatment. To mimic the use of LLZO scrap production with an impurity of the Li-poor pyrochlore phase $La_2Zr_2O_7$, a heat treatment of LLZO powder was used to create a pyrochlore phase. After the heat treatment, XRD measurements were carried out to assess whether the pyrochlore phase was formed. The LLZO-10 and LLZO-20 powders after wet-ball milling and heat treatment at 750 °C for 2 hours were analyzed and compared to pristine LLZO-10 and LLZO-20 in **Figure 4.1.1**.

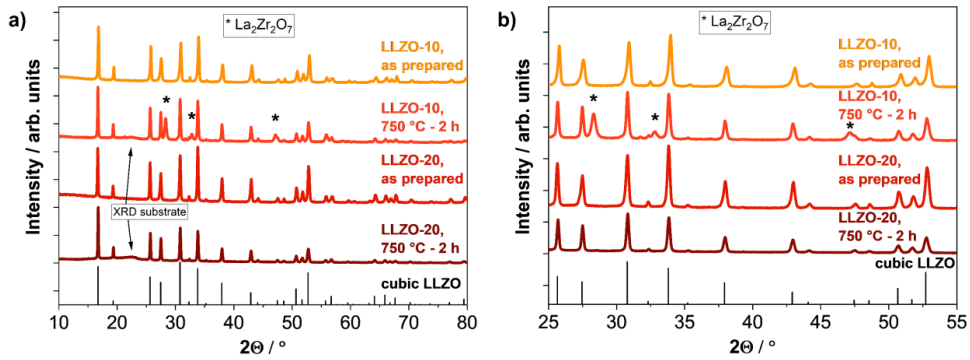

Figure 4.1.1: XRD patterns of the pristine LLZO-10/LLZO-20 powder and the LLZO-10/LLZO-20 after wet-ball milling and additional heat treatment of 750 °C for 2 hours are shown. For analysis, the cubic LLZO reference (ICSD: 182312)[52] is given, while **a)** shows the total pattern, and **b)** is zoomed-in to show the impurity phase in a higher detail.

The pristine LLZO powder shows a pure cubic LLZO structure after synthesis. The powder after wet-milling and heat treatment with Li excess of 10% shows significant amounts of $La_2Zr_2O_7$ (reflectance at 28.1 2Θ).[224] The Li loss at 750 °C was high enough for secondary phases to form. No secondary phases formed in the heat-treated powder with Li excess 20%, which will be discussed below. In all cases, the cubic structure of LLZO was maintained as primary phase.

In order to verify that the heat treatment was the actual cause of the Li loss and thus the impurity of $La_2Zr_2O_7$, the wet-ball milled powder was dried and heat treated at 750 °C for 2 hours in air and in argon. XRD measurements were performed on the dried powder and on the LLZO-10 and LLZO-20 powders after heat treatment in air and argon respectively.

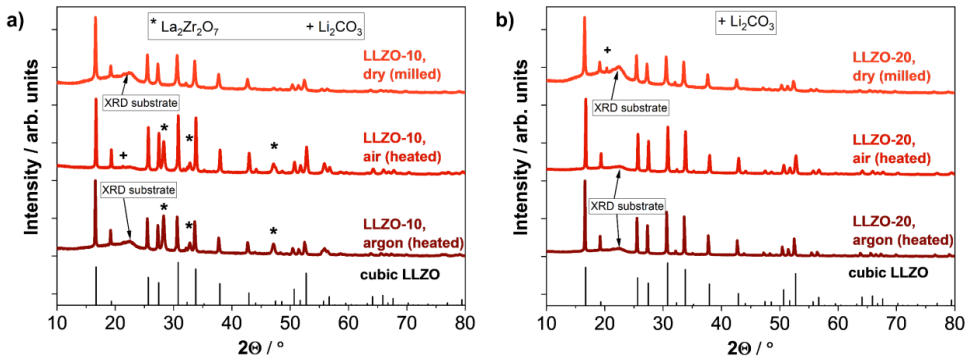

Figure 4.1.2: XRD patterns of the wet-ball milled LLZO powder (dry) and after an additional heat treatment of 750 °C for 2 hours in air and in argon are shown. For analysis, the cubic LLZO reference (ICSD: 182312)[52] is given, while **a)** shows the LLZO-10 powder for each treatment, and **b)** shows the LLZO-20 powder for each treatment.

Due to exposure of the LLZO powder to air during the XRD measurement, the previously described surface reaction with ambient air to form Li_2CO_3 may occur (Eq. 2.3 &2.4). These Li_2CO_3 reflections can appear as an additional impurity in the XRD plots above even though Li_2CO_3 may not occur in the actual synthesis process.

When comparing the analyses of the XRD patterns of the milled powders and the heat-treated LLZO-10 and LLZO-20 powders, two differences can be identified. For the milled LLZO powder (LLZO-10 and LLZO-20), the powder was air dried after wet-ball milling to see the effects of wet-ball milling in direct comparison to the heat-treated powder. The dry powders show the cubic LLZO phase with the exception of an additional Li_2CO_3 impurity in the LLZO-20 powder due to air exposure during XRD measurement.

For the heat treatment in both argon or air for LLZO-10, cubic LLZO is still the main phase, but with a high impurity of $La_2Zr_2O_7$ and small amounts of Li_2CO_3, due to air exposure during data acquisition. In the powder analysis after heat treatment in air or argon with LLZO-20, only the pure cubic LLZO structure is present. This leads to the assumption that the Li excess of 20% in the LLZO-20 powder is high enough to compensate for the Li-loss in the structure during heat treatment. In the LLZO-10 powder, the excess of Li is still insufficient to compensate for the complete Li loss during the heat treatment, and the cubic LLZO structure is transformed into a Li-poor $La_2Zr_2O_7$ phase. The atmosphere of the heat treatment has no influence on the structure of the LLZO, since in both cases the pyrochlore phase $La_2Zr_2O_7$ becomes the main impurity.

It could be shown that the LLZO-10 powder is well able to demonstrate the malfunction of a synthesis in terms of Li loss, with the main impurity phase being $La_2Zr_2O_7$. The LLZO-10 powder with 10% Li

excess shall hence serve as baseline for further investigation of additives. The LLZO-20 powder in turn allows to avoid the pyrochlore phase and is used to demonstrate the influence of impurities on the microstructure in a later sub-chapter.

4.1.2 Influence of LiOH additive on $Li_7La_3Zr_2O_{12}$ waste production material

In the previous section, the main production failure of LLZO by loss of Li was mimicked successfully, resulting in a pyrochlore phase of $La_2Zr_2O_7$ as the main impurity. This sub chapter will now focus on options to avoid the formation of a Li-poor pyrochlore phase during the production process. The central idea of this recycling approach is to use reject material directly from the LLZO synthesis process, which is mimicked by the waste material from the previous sub-chapter. In the present sub chapter now, excess Li is added to the waste production material in the form of LiOH and Li_2CO_3 to compensate for the Li-loss during heat treatment, ultimately avoiding the formation of a $La_2Zr_2O_7$ secondary phase. This re-lithiation approach would allow to restore reject material to the required state, even if the Li content after synthesis of the LLZO powder was insufficient due to typical process malfunctions mentioned above.

The influence of LiOH and Li_2CO_3 as Li sources was analyzed at cell component level of solid electrolytes. Depending on the purpose of adding a Li source, it can be used in four different ways in the process: It can be added during the wet-ball milling step, during subsequent heat treatment, during tape-casting, or during sintering. A scheme (**Figure 4.1.3**) illustrates the addition of the chemical in the various processing steps of a cell component production. “Heat treatment” is defined here as the calcination step at 750 °C for 2 hours, whereas the sintering step, which technically is a heat treatment as well, is defined as “sintering” (by default at 1175 °C for 10 hours, varied).

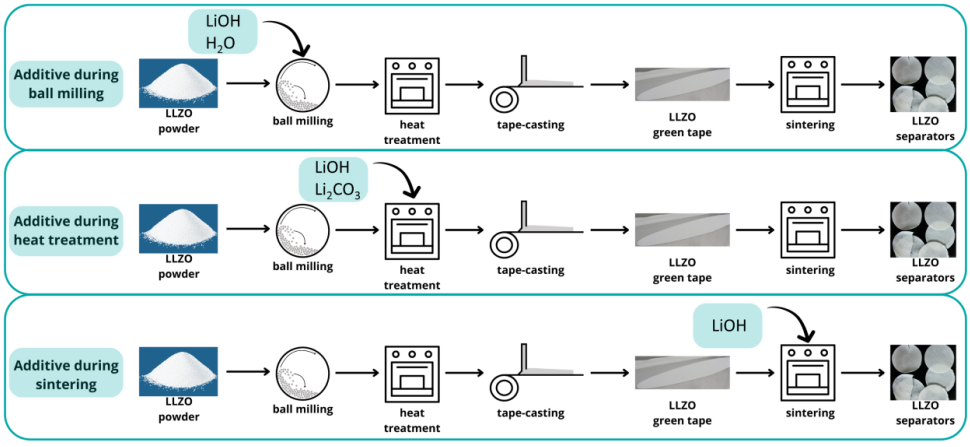

Figure 4.1.3: Scheme of the battery component process of a separator, showing when the different chemicals (either one or both together) were included. Adapted from [9] is licensed under CC BY 4.0 (https://creativecommons.org/licenses/by/4.0/).

The tape casting process is highly sensitive to the particle sizes of the materials. If LiOH or Li_2CO_3 were added to this process step, the powders would hence need to be milled to specifically meet the slurry particle size distribution. This step adds significant process complexity and is unlikely to be adapted in industrial scale applications. It will therefore not be considered further here. Furthermore, adding Li sources during wet-ball milling will not be discussed in detail, but will be discussed briefly in section 4.1.3, including additives such as LiOH and H_2O. As the high temperatures during the first heat treatment and sintering stages exceed the boiling temperature of the Li source, the Li source powder can be easily added into crucibles.

The starting point for this investigation is the LLZO powder ($Li_{6.45}La_3Zr_2Al_{0.05}Ta_{0.4}O_{12}$) with 10% Li excess to ensure initial Li shortage as demonstrated in section 4.1.1. LiOH and Li_2CO_3 additives are used as an additional Li source to counteract the Li loss that would result in a pyrochlore phase in the final solid electrolyte. Any other impurity or dopant effect will not be investigated here in order to avoid effects caused by interdependencies of dopants. At this stage, the focus of the investigation will be on reversing the failure of the synthesis of LLZO powder and later of LLZO green tapes.

Additional Li sources during heat treatment

XRD patterns of the dried LLZO-10 powder have shown a cubic LLZO structure, whereas the most visible change after heat treatment of LLZO-10 powder was an impurity by a pyrochlore phase. This mimics a degradation after a successful LLZO synthesis as it can be caused also by a malfunction or imperfection in an industrial process. As proven above, the synthesized LLZO products would then be contaminated with secondary phases if further treated in the process. Therefore, the first process improvement will focus on the first heat treatment step to avoid the formation of a pyrochlore phase before the green tapes can even be cast. This means that even if LLZO material with insufficient Li excess was produced, it could be saved and further processed by simply adding another Li source. In a first attempt, LiOH respectively Li_2CO_3 was added during the heat treatment by simply adding the powder to the LLZO-10 milled powder and mixing by hand. The mixed powder was then filled into a crucible with a closed lid, ensuring a high Li atmosphere in the crucibles. The molar ratio was kept at 1:1 (LLZO:LiOH), adding the equivalent of a Li excess of 15 % plus the remaining Li excess in the LLZO.

An XRD pattern was recorded after the heat treatment with added Li source to investigate the influence of additional Li excess and if a high Li atmosphere can prevent the material from decomposing into $La_2Zr_2O_7$.

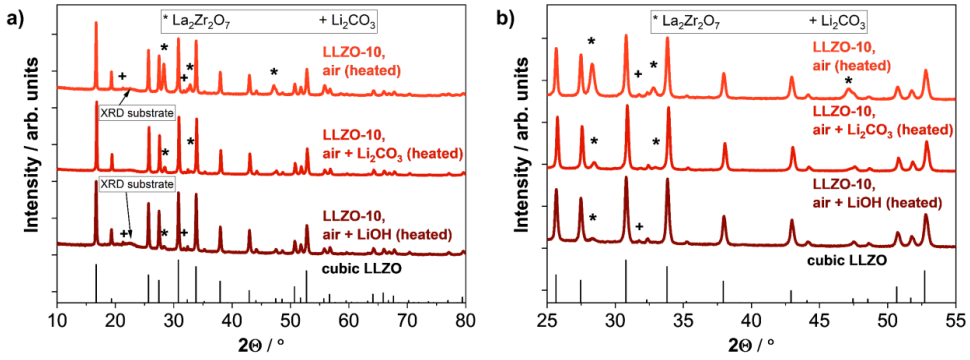

Figure 4.1.4: XRD pattern of LLZO-10 milled powder after heat treatment in air without addition, with addition of Li_2CO_3 and with an addition of LiOH. For analysis, the cubic LLZO reference (ICSD: 182312)[52] is given, while **a)** shows the total pattern, and **b)** is zoomed-in to show the impurity phase in a higher detail.

The amount of pyrochlore phase $La_2Zr_2O_7$ decreases, almost disappears, compared to **Figure 4.1.2 a** without added Li source, which means that a Li-rich atmosphere can prevent Li loss during heat treatment, at much lower temperatures than usual during synthesis (750 °C compared to 900-1000 °C), where the Li excess is normally used. It is known from LLZO synthesis that $La_2Zr_2O_7$ is one of the forming phases of LLZO already at temperatures as low as 400 °C.[82] During synthesis, the pyrochlore phase increases, with increasing temperature until 800 °C, where the Li source in the synthesis will melt and form LLZO.[82,83] We propose that a similar mechanism occurs during the re-lithiation. Since all necessary chemicals are present in the green tape, the pyrochlore phase is formed into LLZO by melting Li_2CO_3 respectively LiOH, which was added to the crucible and enriched the Li atmosphere at even higher temperatures.

The LLZO-10 powder heat treated with additional LiOH (LLZO-10, air+LiOH (heated)) was then further processed to a separator tape via tape-casting and sintering on an LLZO-20 powder bed according to **Figure 4.1.3**, without any further additions during the process. The green tapes were placed on an LLZO powder bed consisting of LLZO-20 powder during sintering. In addition to prove the cubic LLZO structure of the resulting separator tape, also the microstructure was analyzed to see if any changes occur during the first heat treatment caused by the additional Li source. The LLZO tapes processed in a similar way by Rosen *et al.*[107] shall serve as reference for the microstructure here.

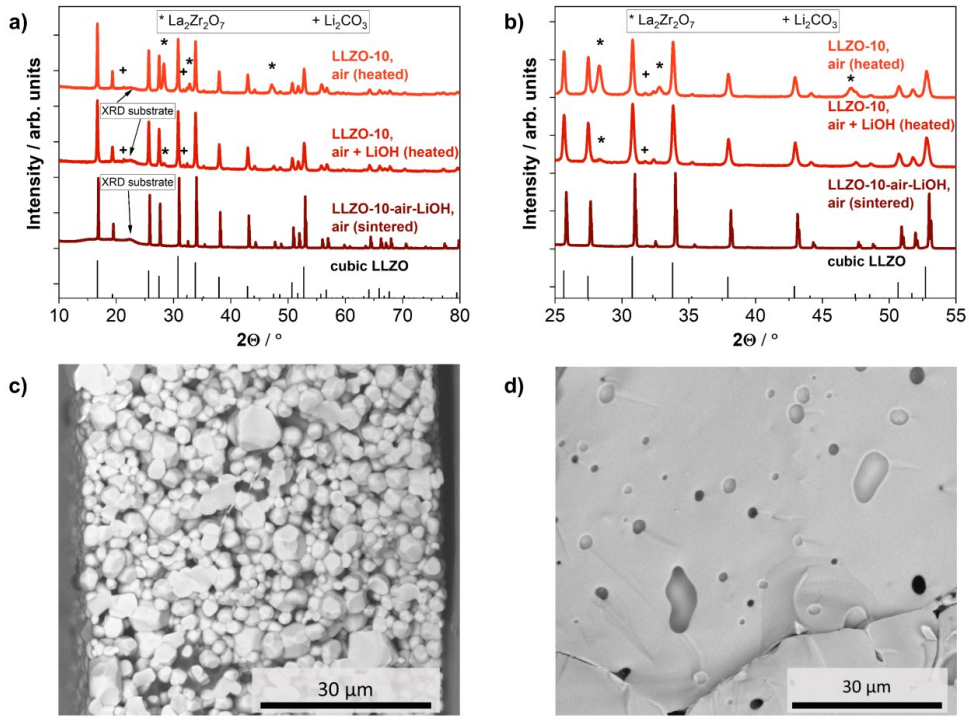

Figure 4.1.5: XRD patterns of LLZO-10 powder after heat treatment in air with and without addition of LiOH and the sintered tape, after heat treatment with LiOH. For analysis, the cubic LLZO reference (ICSD: 182312)[52] is given, while **a)** shows the total pattern, and **b)** is zoomed-in to show the impurity phase in a higher detail. BSE-SEM image of a cross-section (fractured, un-polished) of a sintered LLZO tape with additional LiOH in the first heat treatment step shown to evaluate the grain growth, grain shape and grain size. **c)** shows a different area of the same tape as **d)**.

The sintered separator tape had a total shrinkage in x-y direction of 20%, resulting in a thickness of 60 µm with a relative density of at least 70% (obtained by ImageJ analysis). Analysis of the XRD patterns showed that the cubic LLZO structure was obtained. Interestingly, the LLZO-10 powder still showed a $La_2Zr_2O_7$ impurity after the first heat treatment with addition of LiOH, which was nearly completely removed after the sintering step. At this point, the LLZO-20 powder bed during sintering should be recalled once again: Besides the primary purpose of separating the green tapes from the MgO plate or the crucible below, it also contains excess Li. It is therefore assumed here that the Li excess in the crucible atmosphere due to the Li release from the LLZO-20 powder bed is high enough to not only compensate the Li loss during sintering, but also to re-lithiate the pyrochlore phase initially present in the tape. This hypothesis will be examined later in chapter 4.1.3.

Cross-sectional BSE-SEM images of a fractured LLZO separator tape were taken (**Figure 4.1.5 c+d**), without any polishing steps, to evaluate grain growth and possible changes in the microstructure. Here, one can clearly see a change from previously obtained LLZO separator tapes in the same process without additional Li sources, shown by Rosen *et al.*[107] Two different areas can be distinguished in the microstructure of the sintered tape: One area (**Figure 4.1.5 c**) has uniformly shaped grains with an

average grain size of 3.5 µm (calculated by ImageJ, see chapter 3.2.3). The second area (**Figure 4.1.5 d**) shows a different structure of either three large grains with residual intragranular pores or many grains without visible grain boundaries. The assumption of many small grains without visible grain boundaries would imply that the LLZO tape undergoes a change from intergranular fracture to intragranular fracture. Kim *et al*. found a change from intergranular to intragranular fracture with increasing density of their LLZO sample.[104] On the contrary, an intergranular fracture could be observed, when impurities or sintering additives are located at grain boundaries, although the ceramic in that study was yttria-stabilized zirconia.[228] The assumption of a larger grain, however, would indicate abnormal grain growth, due to the large change in grain size distribution. A large grain across the entire thickness of the tape, resulting in a grain size of tens of microns to hundreds of microns, would represent an increase of up to two orders of magnitude compared to the smaller grains. The general definition of abnormal grain growth is the variation in the growth of a few grains that grow larger than the surrounding grains.[229] There are several factors that can cause such an abnormal grain growth. These include the presence of impurities or secondary phase particles that affect the grain boundaries, which is a driving force for grain growth.[102,229] In addition, impurities or second phases can lead to liquid phase sintering, where a different grain growth mechanism operates.[102] The advantages of abnormal grain growth are large grains without internal grain boundaries, resulting in a higher bulk content and less blocking grain boundaries. Disadvantages are the difficulty of control during growth, the inhomogeneous distribution of grains, and the weak grain boundary on large grains due to the impurities in this area.[99] In contact with Li metal, it may on the one hand be beneficial due to lower amounts of grain boundaries at the contact area, but on the other hand disadvantageous as the path for the Li dendrite is straightforward at a single grain boundary.

Additional Li sources during sintering

It was shown in the last section that small impurities of $La_2Zr_2O_7$ can be re-lithiated by the Li excess from the LLZO-20 powder bed in the crucible. This suggests that Li excess does not only prevent the formation of a Li-poor pyrochlore phase, but Li excess can actually revert existing $La_2Zr_2O_7$ impurities during the sintering step. The idea was hence developed to skip the addition of Li sources before heat treatment and instead re-lithiate directly in the sintering step. To overcome the potential problem of Li loss, LiOH was added as an additional source to the tapes in the crucible to examine its capability to re-lithiate the already formed pyrochlore phase $La_2Zr_2O_7$.

Therefore, green tapes with high impurity of $La_2Zr_2O_7$ were obtained, followed by sintering with the added LiOH to improve the Li atmosphere in the crucible. The resulting separator tapes were then analyzed first via XRD and BSE-SEM as shown in **Figure 4.1.6**.

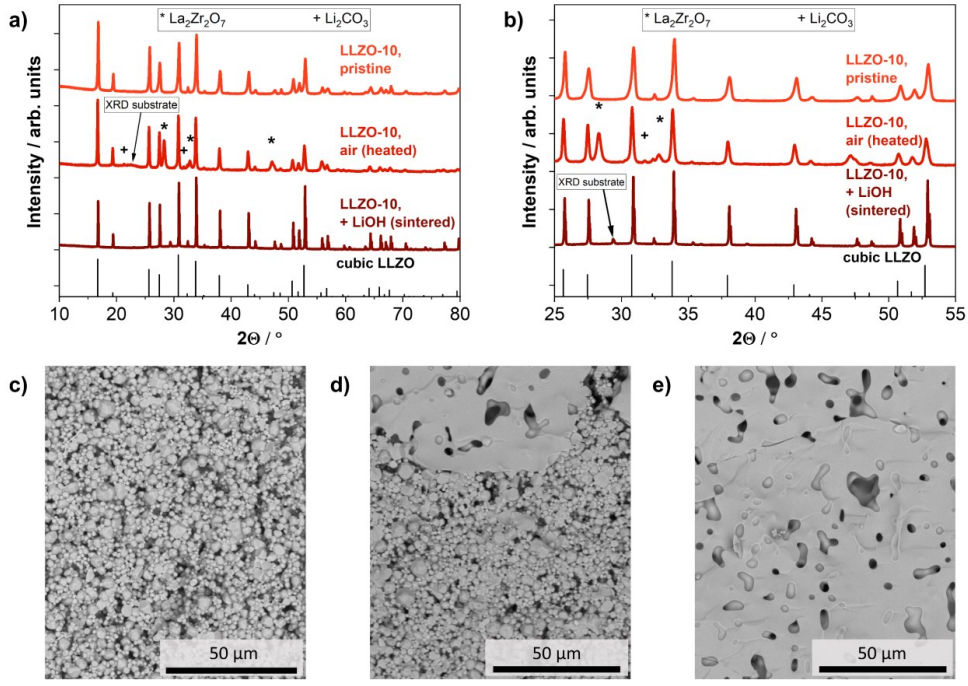

Figure 4.1.6: XRD patterns of pristine LLZO-10 powder, after heat treatment in air without addition, and the sintered tape with LiOH addition during sintering. For analysis, the cubic LLZO reference (ICSD: 182312)[52] is given, while **a)** shows the total pattern, and **b)** is zoomed-in to show the impurity phase in a higher detail. BSE-SEM image of a cross-section (fractured, un-polished) of a sintered LLZO tape with additional LiOH during sintering is shown to evaluate the grain growth, grain shape and grain size. **c)-e)** show different areas of the same tape.

The analysis of the XRD patterns shows that with an added Li source such as LiOH in the sintering atmosphere, the LLZO was significantly re-lithiated compared to the LLZO powder after the first heat-treatment with the $La_2Zr_2O_7$ impurity, thus restoring a pure cubic LLZO phase (within the detection range of the XRD).

The analysis of the microstructure of the sintered tapes by BSE-SEM reveals areas with very large grains as observed in the last sub section. A comparison of different areas of the tape suggests two different grain growth mechanisms. For the sintered separator with additional Li in the sintering atmosphere, a microstructure similar to the addition of Li source in the first heat treatment step was observed. The abnormal grain growth is again observed, leading to the assumption that a Li-rich atmosphere changes the grain growth mechanism in a similar way compared to manual mixing into the LLZO powder. Here, large pores are observed, which reduce the density of the large grain. However, the particles neighboring the abnormal grains show a partial sintering behavior without clear sintering activity. The grains have an average grain size of 2.6 µm, proving that almost no growth occurred during sintering, as the initial particle size is below 1 µm.

This undesired behavior may represent a relevant electro-chemical disadvantage in some cases (see sub chapter 4.1.3 for details). Another disadvantage of the abnormal grain growth becomes obvious when handling the sintered tapes: Due to the brittleness of the tapes, only parts of the tape could be removed from the sintering crucible in most cases. An evaluation of the entire tape with an estimation of the area covered by large grains is hence not possible. Also industrial upscaling is challenging with increasing fragility. It will therefore be necessary to better understand and possibly limit abnormal grain growth in LLZO to allow adaptation in industrial processes that were developed within this chapter.

Subsection summary

After mimicking a typical waste material production with a pyrochlore phase of $La_2Zr_2O_7$, this chapter first describes a successful suppression of the unwanted pyrochlore phase during heat treatment of LLZO via the addition of Li_2CO_3 and LiOH. In a second step, the re-lithiation of an existing pyrochlore phase to cubic LLZO was achieved by adding LiOH to the sintering process. Due to the addition of a Li source, the grains tend to show abnormal grain growth, resulting in large single crystals with sizes up to 350 µm. This structure has some significant disadvantages which makes in-depth studies of abnormal grain growth in LLZO necessary.

4.1.3 Understanding abnormal grain growth in $Li_7La_3Zr_2O_{12}$:Ta,Al

The focus of the present sub chapter is a better understanding of abnormal grain growth in LLZO and its dependency on different process parameters. The effect of abnormal grain growth on the conductivity of the separator has been reported inconsistently by different studies. Whilst Kim *et al.* for example found that it leads to a higher ionic conductivity due to fewer grain boundaries, Cheng *et al.* showed that grains with a size of 20-40 µm have a higher ionic conductivity than larger grains.[123,230] It is reported that the mechanical stability increases with increasing density or decreasing grain size. [231] Abnormal grain growth has been studied with respect to mechanical strength, resulting in a much lower value than for homogeneous fine-grained LLZO.[232] Intergranular fracture was observed firstly because impurities weaken the grain boundaries, and secondly by the lack of structural support from other grains which increases the risk of tape breakage when only one grain layer is present throughout the tape thickness.[99] The same effect also causes low resistance against Li dendrite growth as a further relevant separator parameter: Whilst the dendrites do not perforate the large grains themselves, the probability of Li dendrite growth is increased significantly along the grain boundaries. Since the large grains do not overlap, they form straight intergranular channels which are favorable for rapid dendrite growth.[233,234]

On the other hand, abnormally large grains have the advantage of a high density of the bulk material. Only a few round pores are typically retained, suggesting that a gas was trapped during growth.[98] In both cases, the abnormally large grains are larger than the thickness of the tape itself. This means that only one large grain defines the microstructure across the entire thickness of the tape. This would also mean that in the case of a battery application as a separator, the bulk ionic conductivity is the limiting conductivity in these areas because there are much fewer grain boundaries.

Since an additional Li source was added to the system, the most likely cause for abnormal grain growth would be an impurity or secondary phase, a theory which shall be further evaluated in this section.

Confirming abnormal grain growth

In a first step, the occurrence of abnormally large grains shall be confirmed by EBSD analysis. This would allow to rule out the second explanatory approach presented in sub chapter 4.1.2 by which very fine grains without visible grain boundaries may be mistaken for large grains. The following **Figure 4.1.7** illustrates a tape with the observed structure against a millimeter paper background to indicate the composition of the tape. It should be noted for transparency that the tapes in **Figure 4.1.7** and **Figure 4.1.8** were selected based on the clearest images to illustrate the pattern. In this exact batch, the LiOH happens to be added together with H_2O in the milling step, the following analyses prove the exact same behavior in case of the LiOH addition during sintering though. A detailed list of all experiments resulting in abnormal grain growth is given in **Table 4-1**.

Table 4-1: Summary of each experiment leading to abnormal grain growth, not discussed in the work presented.

LLZO:Ta,Al	*Additive 1*	*Step 1*	*Additive 2*	*Step 2*	*Sintering temperature, -time*	*AGG*
10% Li excess	H_2O (10 vol%)	Ball-milling	--	--	1175 °C – 10 hours	***Yes***
10% Li excess	H_2O (10 vol%)	Ball-milling	LiOH (1:1 molar ratio)	sintering	1175 °C – 10 hours	***Yes***
10% Li excess	H_2O (10 vol%) + LiOH	Ball-milling	--	--	1175 °C – 10 hours	***Yes***
10% Li excess	H_2O (10 vol%) + LiOH	Ball-milling	--	--	1050 °C – 10 hours	***Yes***
20% Li excess	H_2O (10 vol%)	Ball-milling	--	--	1175 °C – 10 hours	***Yes***

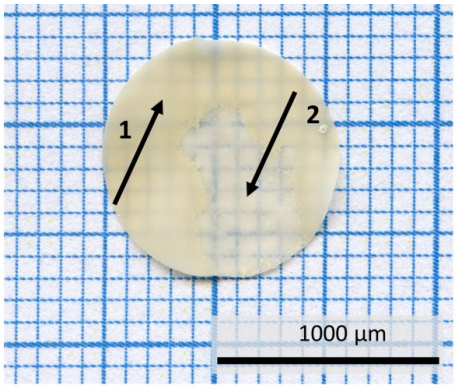

Figure 4.1.7: Scan of a tape with abnormal grain growth in the middle (transparent area, No. 2) on millimeter paper

The image shows a full tape, while the arrows highlight two different areas: Arrow No. 1 shows a translucent small-grained area. Arrow No. 2 indicates the presumably large grain area, which is more transparent. The reason could be the low effect of refraction combined with much reduced impurities along the very few grain boundaries in an area with large grains.[235] The transparent area correlates with these areas where large grains with grain sizes >100 µm seem to exist according to above BSE-SEM analysis.

Additional EBSD measurements were then performed to evaluate whether the large grains are actually single crystals or consist of multiple small grains without visible boundaries.

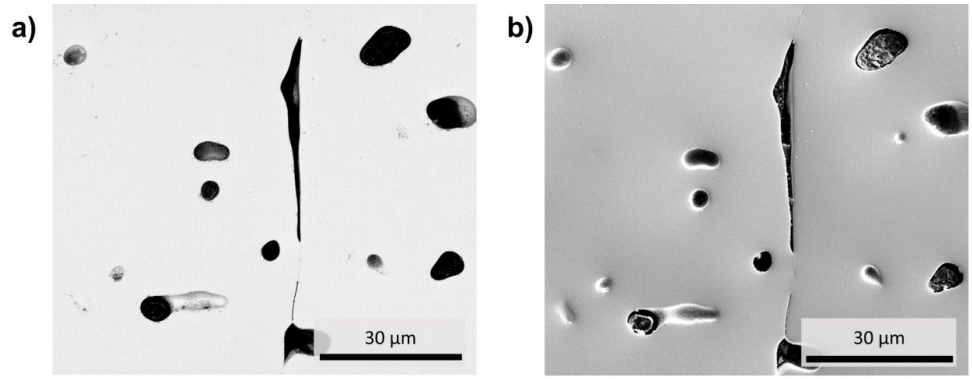

Figure 4.1.8: Polished cross-section of a sintered LLZO tape, area at an abnormal grain taken with **a)** an EBSD detector, where pattern quality is visible and **b)** showing the secondary electron image.

The image in **Figure 4.1.8 a** shows the pattern quality, which gives an idea of the intensity of the Kikuchi bands. The pattern quality depends on a lot of factors, but one can summarize that a dark area means no pattern could be observed, cause by *e.g.* grain boundaries, pores, lattice defects, surface contamination. As indicated by the overall bright area in both large grains, clearly no grain boundary can be detected. This shows that each large grain is indeed a single crystal of 100-350 µm. It can now be confirmed that sintering of LLZO with the addition of LiOH before calcination can indeed lead to abnormal grain growth.

To investigate abnormal grain growth, each sample was analyzed by SEM measurements of a fractured cross-section to evaluate the intergranular or intragranular fracturing and to visualize large grains. The process parameters were kept constant, throughout the time and temperature experiments, although they varied from the above experiments. The optimized parameter can be found in the experimental section 3.1.1.

Demonstrating abnormal grain growth in Li-saturated crucible environment

In a next step, it shall now be shown that sintering LLZO in Li-saturated crucibles does produce the same abnormal grain growth as found in the last section. The LLZO-10 and LLZO-20 powders were used as a starting point for the study, while no additional Li source was added during the process itself. Prior to sintering, the crucibles used were saturated using LiOH. To demonstrate that abnormal grain

growth is again visible in the tapes, LLZO-10 and LLZO-20 powders without further addition of Li sources were compared before and after sintering in saturated Li-Al crucibles.

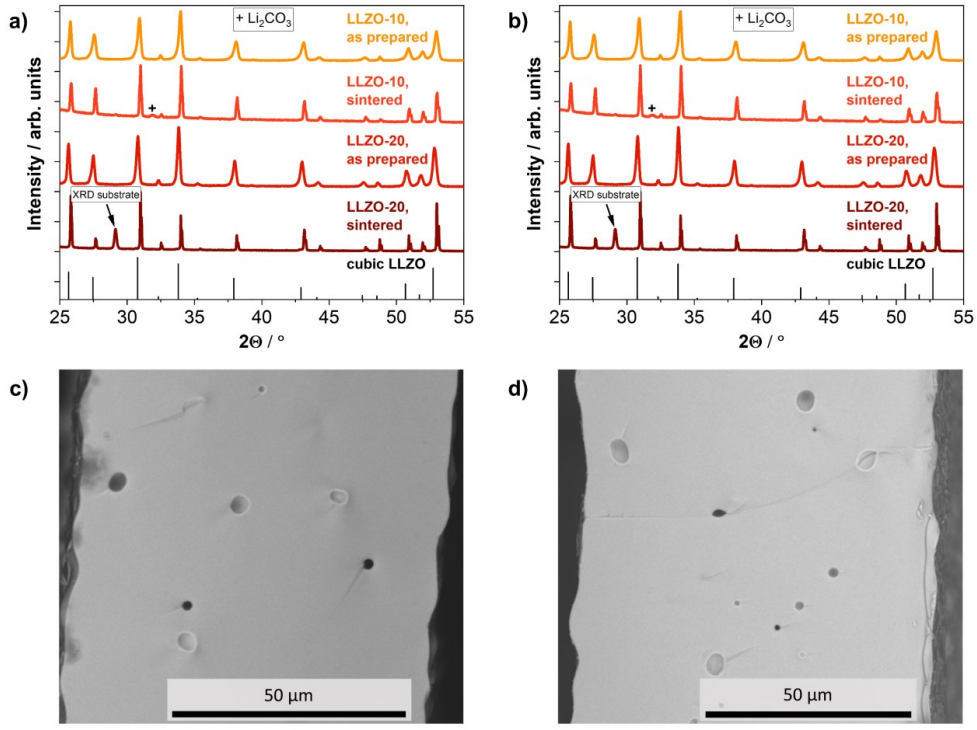

Figure 4.1.9: XRD patterns of pristine LLZO-10/LLZO-20 powder, after synthesis, and the sintered tape without Li source, sintered in a Li saturated crucible. For analysis, the cubic LLZO reference (ICSD: 182312)[52] is given, while **a)** shows the total pattern, and **b)** is zoomed-in to show the impurity phase in a higher detail. BSE-SEM image of a cross-section (fractured, un-polished) of a sintered LLZO tape without additional Li source but sintered in a Li saturated crucible is shown to evaluate the grain growth, grain shape and grain size. **c)** shows the tape sintered from LLZO-10 powder, **d)** shows the tape sintered from LLZO-20 powder.

XRD measurement and BSE-SEM images of a fractured surface of each tape were taken to evaluate the expectation that abnormal grain growth still occurs at 1175 °C for 10 hours of sintering. The XRD plots confirm that the Li-saturated crucible, which was used to sinter the tapes, indeed saturates the atmosphere in the crucible with Li-ions to such an extent that it prevents the formation of the Li-poor $La_2Zr_2O_7$ phase and also shows exactly the same abnormal grain growth as observed in section 4.1.2. In both cases (LLZO-10 and LLZO-20), the amount of Li in the atmosphere during sintering is high enough to show the expected microstructure, which will be investigated next.

To further investigate the occurrence of abnormal grain growth, BSE-SEM images are analyzed. There are several problems in analyzing the grains. Firstly, the brittleness of the tapes itself precludes a chemical or thermal treatment to make grain boundaries visible after polishing. Another problem with the surface of a polished LLZO tape is the high reactivity in air to Li_2CO_3, which interferes with the measurement. Therefore, only the fractured cross-sections can be analyzed. Even if the resulting grain

size distribution cannot be compared 1:1 to grain sizes extracted from polished surfaces, the deviation between the two is very low (see explanation in chapter 3.2.3). More importantly, however, the following approach relies solely on relative comparability between the grain size distributions which are all produced in the same way and hence are comparable between each other. Secondly, the images taken cover only a small section of the tape, meaning that the cross-section should ideally be at a location where, in the best case, all types of grain growth in the tape can be seen. To improve the reliability of the findings, at least 5 images (not all shown here) were analyzed and statistically averaged for every experimental case, trying to cover all types of grain growth to get a representative overview: no significant changes in grain size, an abnormally large grain and the transition of an abnormally large grain to the area of smaller grain sizes are the most common area types observed in the tape. Exemplary BSE-SEM images of these three type areas are shown in the following **Figure 4.1.10**.

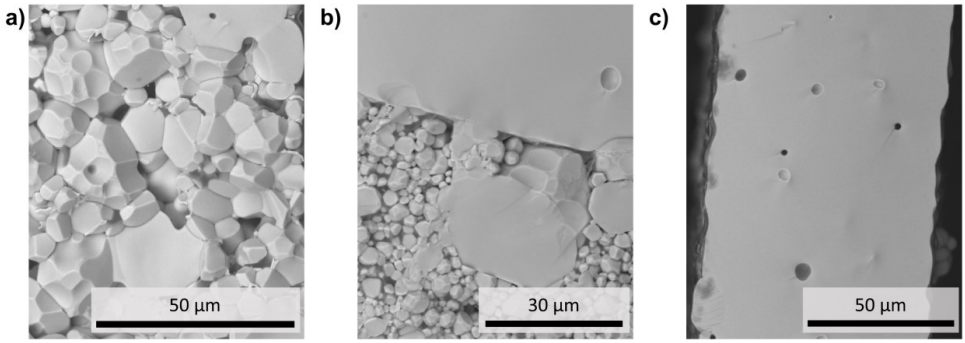

Figure 4.1.10: BSE-SEM image of LLZO tape cross-section (fractured, un-polished) sintered in Li saturated crucible (1175 °C, 10 hours, LLZO-10). **a-c)** show different areas with three typical kinds of grain growth.

Figure 4.1.10 a shows grains up to 25 µm in size. The second image shows a large grain in contact with grains that are much smaller than in the other image. Grains up to a few microns in size are found in this section, except for one large grain in the center of the image. The relevance of abnormal grain growth for the tape structure becomes obvious in the BSE-SEM image in **Figure 4.1.10 b**, when analyzing the large size difference between the grains (up to two orders of magnitude). The last image shows only a single large grain with a few round pores, suggesting that gas has been trapped inside. An analysis of the density of this area (intragranular fractures) yields density values as high as 99% for the large grain of the tape sintered at 1175 °C for 10 hours. This is a high value for sintered ceramics, even if not over the entire area of the tape. The relative density of the entire tape was analyzed separately via ImageJ and was determined to be at least 86%. Similarly to the challenges described hereabove, it is difficult to analyze the density though due to the brittleness of the tape, the low weight and the reactive surface. The methodology hence relies on a fractured cross-section as well, the exact procedure and potential value deviations are described in chapter 3.2.3.

The grain size trends are now analyzed to see the potential effects of the sintering. The grain size is calculated using ImageJ and normalized to the total grain count, once only for areas that do not show abnormal grain growth (**Figure 4.1.10 a**) and once only for those sections that contain abnormal grain growth (**Figure 4.1.10 b+c**). It was found though that besides the first two peaks, the rest of the grain

size roughly follows a Gaussian distribution (see **Figure 4.1.11 a**), which was used to fit it in a secondary step. A detailed step by step analysis procedure is shown in chapter 3.2.3.

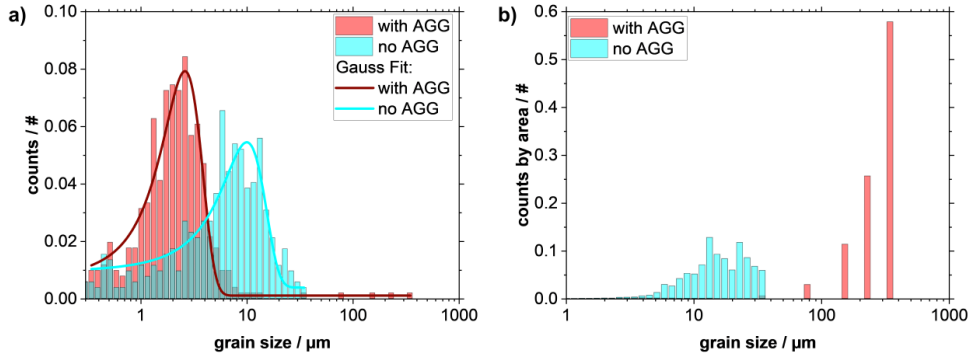

Figure 4.1.11: Grain size distribution of the sintered tape, shown above, with the following sintering parameters: 1175 °C for 10 h. The grain size distribution was evaluated by ImageJ, and shows the grain sizes for images without abnormal grain growth and with abnormal grain growth. **A)** shows the grain size distribution by counts with a Gaussian fit, while **b)** shows the grain size distribution normalized to the area.

The analysis of the sections without abnormal grain growth resulted in the green plot labeled as "no AGG" in **Figure 4.1.11**, revealing a cluster of grain sizes around the size of 10 µm (maximum of fitting curve at 9.9 µm) and no large grains as expected. Focusing only on areas with abnormal grain growth as shown exemplarily in **Figure 4.1.10 b+c** resulted in the grain size distribution labeled "with AGG" in red in **Figure 4.1.11**. Here, four small counts of large grains, three of them >100 µm, are visible, while the grain size distribution of the smaller, neighboring grains is shifted to low grain sizes. Their dominance in the count-based grain size distribution does not reflect their share of the tape area. In order to visualize this effect, the grain size distribution was normalized to the total area in **Figure 4.1.11 b** to show the proportions of the area covered by few small grains compared to many small ones. It shows that more than 80% of the image section areas are covered by only 4 large grains in the case of the selected images and gives a quantitative impression of the local dominance of large grains. The exact share depends on the exact image sections though and cannot be generalized further. For the images without abnormal grain growth (in green), however, the maximum is still just above 10 µm, while small grains <3 µm are no longer visible in the plot.[236] The distribution peaks at 2.6 µm, hence significantly smaller also than in areas that are not influenced by abnormal grain growth. This can be explained by a look at the lower part of **Figure 4.1.10 b**: It shows an overall smaller grain size accumulation next to the abnormally large grain. This can be explained by constrained sintering, where large grains exhibit a rapid densification and grain boundaries have a high mobility, while constrained sintering with rigid inclusions minimizes the grain growth next to the large grains.[98,236] It is clear that the poor sintering behavior of the grains neighboring the abnormally large grains is detrimental to the suitability of the produced separator tape. It should be kept in mind, however, that these very small grains appear mainly close to abnormally large grains.

Impact of sintering time on abnormal grain growth

To better understand under which conditions abnormal grain growth takes place, the effects of sintering parameter changes are assessed in the following. Therefore, time and temperature, the most easily accessible parameters during sintering, were varied. First, the temperature was fixed at 1175 °C, as the original sintering is 1175 °C for 10h, and the time was varied from 10h (long time sintering), 5h, 1h and 15 minutes (short time sintering). Subsequently, the temperature was varied from 1175 °C over 1150 °C, 1100 °C, 1050 °C, and 1025 °C to 1000 °C for a given time.

The above analysis with 1175°C and 10 h dwell time is the starting point for further evaluation of the dependence of abnormal grain growth first on the sintering time. The next experiment in the series starts by reducing the sintering time to 5h, i.e. half of the dwell time above.

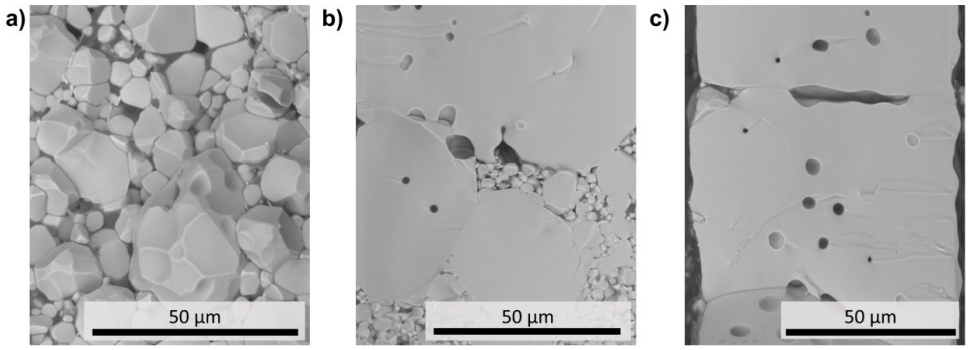

Figure 4.1.12: BSE-SEM image of a cross-section (fractured, not polished) of a sintered LLZO tape without additional Li source but sintered in a Li saturated crucible is shown to evaluate the grain growth, grain shape and grain size. Here, sintering parameters were as following: 1175 °C for 5 hours with LLZO-10 powder. **a-c)** show the tape sintered in different areas, to capture all three kinds of grain growth.

Analysis of the sintered tape at 1175 °C for 5 hours sintering time shows a similar grain growth compared to 1175 °C for 10 hours (**Figure 4.1.12**). Both tapes have three different types of areas, such as grains with a size of 25 µm, areas with a large grain surrounded by small grains smaller than 5 µm, and large grains with a size larger than the thickness of the tape. Here, the large grains have more intragranular pores, resulting in a lower density (95%) than the tape sintered for 10 hours. **Figure *4.1.12* c** even shows two connected large grains with an elliptical pore between the large grains. Longer sintering times would probably decrease the amount of pores trapped inside the large grains.[98] The overall impression based on visual interpretation of the SEM images is confirmed by the ImageJ-based grain size analysis, showing that the distribution especially for areas with large grains is indeed comparable to that of the tape sintered at 1175 °C for 10 hours, even if differences exist.

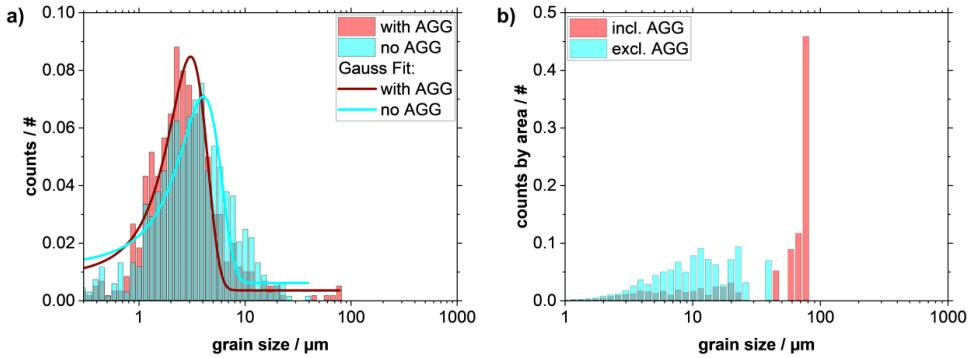

Figure 4.1.13: Grain size distribution of the sintered tape, shown above, with the following sintering parameters: 1175 °C for 5 h. The grain size distribution was evaluated by ImageJ and shows the grain sizes for images without abnormal grain growth and with abnormal grain growth. **A)** shows the grain size distribution by counts with a Gaussian fit, while **b)** shows the grain size distribution normalized to the area.

Comparing the grain size distribution of the tape sintered for 5 hours with that of the tape sintered for 10 hours, it should first be noted that a significant impact on the predominant grain size in regions without abnormal grain growth is observed: Whilst the Gauss peak for the green plot was at 9.9 µm before in **Figure 4.1.11 a**, it is now 60% lower at 4.0 µm in **Figure 4.1.13 a**. This demonstrates the necessity of longer sintering times for normal grain growth. Large grains occupy most of the area (**Figure 4.1.13 b**) despite the much greater number of small particles peaking at a value of 3.4 µm (**Figure 4.1.13 a**). Comparing these results to **Figure 4.1.11**, it is impressive how close the size distributions of 5 hours and 10 hours samples are when the areas near abnormally large grains are considered. However, the size of the abnormally large grains themselves as well as their total area share does further increase with increasing time.

To further analyze the dependency of abnormal grain growth on sintering time, the dwell time was reduced first to 1 hour and then to 0.25 hours. For comparison, BSE-SEM images of all four sintering times are shown in the following **Figure 4.1.14**. Whilst isolated large grain areas could be identified visually in samples with 1 h sintering time (not shown here), no more abnormally large grains were found after 0.25 h sintering. To allow visual comparison, **Figure 4.1.14** therefore contains only image sections without impact of abnormal grains also for the 10 h, 5 h and 1 hour sample.

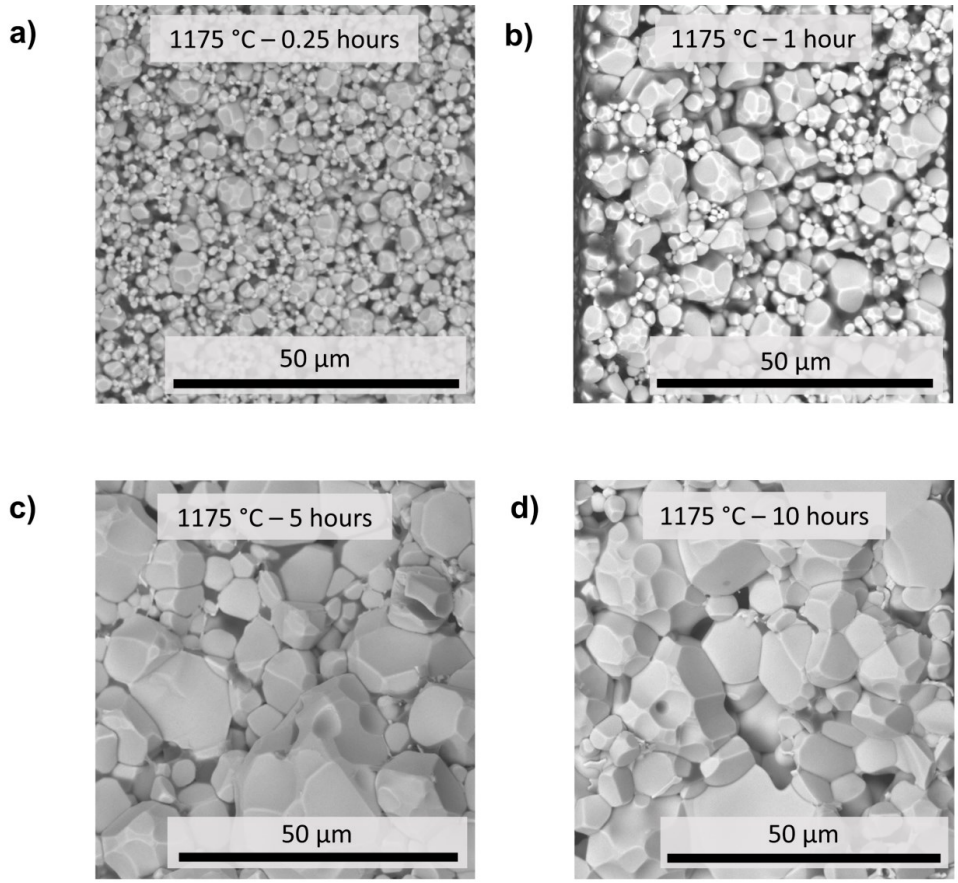

Figure 4.1.14: BSE-SEM image of a cross-section (fractured, not polished) of a sintered LLZO tape without additional Li source but sintered in a Li saturated crucible is shown to evaluate the grain growth, grain shape and grain size. Here, sintering parameters were as following: **a)** for 0.25 hours, **b)** for 1 hour, **c)** for 5 hours and **d)** for 10 hours, all at 1175 °C with LLZO-10 powder.

The analysis of BSE-SEM images reveals a homogenously distributed grain structure for all four tapes. However, it also shows a further decrease in grain size of the sintered tapes in non-abnormal grain growth areas with decreasing dwell times from 1 hour to 0.25 h. The particles are very small and only a few isolated sintered grains can be made out (**Figure 4.1.15**). In both cases, the particles do not sinter well together, with again a visible decrease from 1 hour to 0.25 hours. It becomes obvious that the normal grain growth is limited by the sintering time, and abnormal grain growth is strongly reduced, even suppressed in the case of the 0.25 h tape. It is not clear yet whether the reason for the latter is only time dependent or if additional unknown factors have an influence as well. Furthermore, the density resulting from the four sintering times can be compared. Just like for the grain sizes, the density based on fractured surfaces can only be considered an estimate and tends to be underestimated (see chapter 3.2.5) but can be compared relatively: The density is around 88% for the 10 hours and 5 hours tapes (87%), while it decreases with time to 72% for the 1 hour and 0.25 hours tape (73% and 71%

respectively). The grain size distribution is shown below for both sintering times (1 hour and 0.25 hours) in the same graph, as abnormal grain growth does not exist in the tape sintered for 0.25 hours.

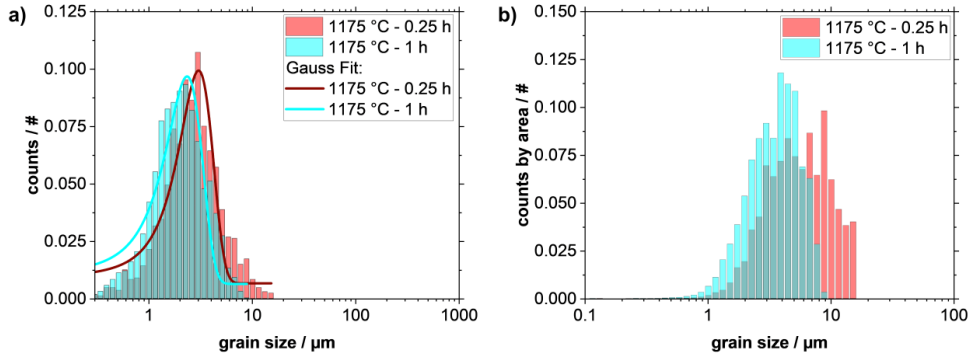

Figure 4.1.15: Grain size distribution of the sintered tape, shown above, with the following sintering parameters: 1175 °C for 1 h and 0.25 h. The grain size distribution was evaluated by ImageJ and shows the grain sizes for images without abnormal grain growth. **A)** shows the grain size distribution by counts with a Gaussian fit, while **b)** shows the grain size distribution normalized to the area.

The grain sizes of the tape sintered for 1 hour and the tape sintered for 0.25 hours are similar to each other. There is, however, still a shift to smaller grain sizes as the dwell time decreases, given that the Gaussian maximum for 1 hour is at 3.0 µm vs. 2.3 µm for 0.25 hours, which confirms the impression from **Figure 4.1.14**. Probable explanation for the different behavior could be that the grain growth does barely occur in the 15-minute timeframe. The grain sizes are only marginally larger than the powder particles, hence confirming that there is limited densification and grain growth is suppressed.

In the following plot, the grain size peak (Gaussian) is plotted against the sintering time to provide a wholistic overview of the grain sizes in areas with and without abnormal grain growth for different sintering times. Also, the maximum large grain sizes are plotted, even if this can be considered indicative only as the number of recorded image sections in combination with the low total number of large grains does not allow for a statistically reliable statement.

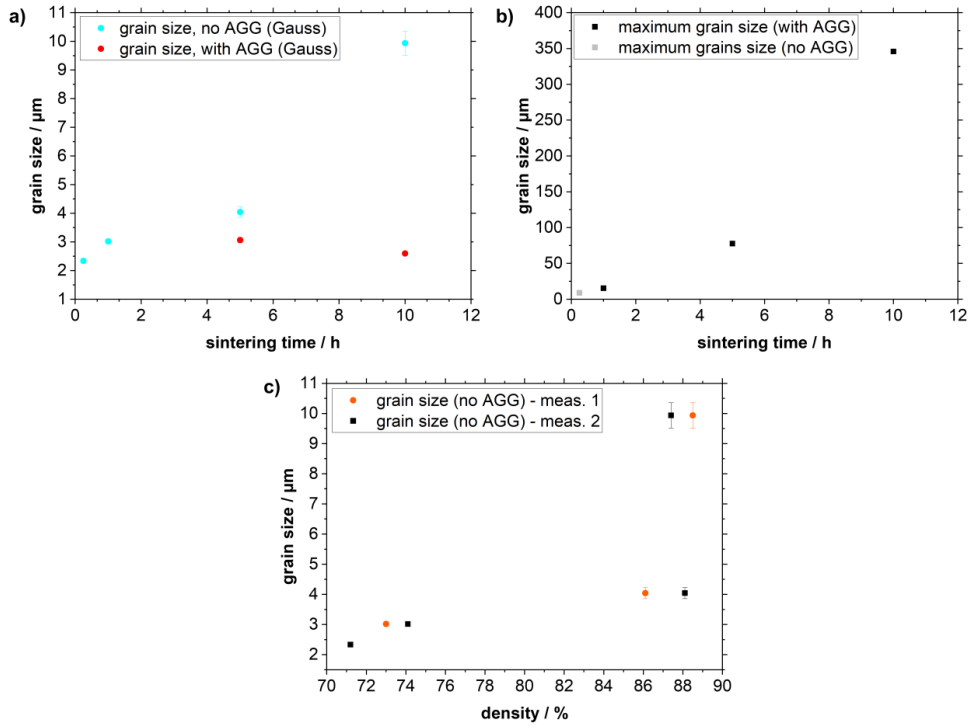

Figure 4.1.16: a) Gauss fit peak values for the grain size distribution of the sintered tapes over the sintering time, differentiating between areas with and without abnormal grain growth. **b)** Maximum grain sizes in the tape over the sintering time. **c)** Gauss fit peak values for the grain size distribution in areas without abnormal grain growth depending on the tape density.

The analysis of the predominant grain size in areas not affected by abnormal grain growth as function of sintering time shows a clear increase in normal grain sizes from 2.3 µm to 9.9 µm over the dwell time range from 0.25 hours to 10 hours. The increase in sintering time from 5 hours to 10 hours has a much bigger impact than the change from 1 hour to 5 hours, indicating that longer sintering times are advantageous for tape structures that are not affected by abnormal grain growth. The grain sizes at the boundaries of abnormally large grains behave completely differently though. They could only be captured for tapes sintered for 5 hours and 10 hours but allow an interesting conclusion: The sintering time within the tested range does not seem to have any significant impact on the small grains microstructure near abnormally large grains which is caused by constrained sintering.[98] Appearing around 1 hour of sintering time, the abnormally large grains did grow further non-linearly with increasing sintering times until the largest abnormal grain size of 345 µm was obtained at 10 hours sintering time. However, due to the large size of the grains partly exceeding the image sections and their low number, a statistically valid statement cannot be made as mentioned also above. The density measurements are only a rough estimation but still follow the typically exponential curve of density and grain growth.

It is very interesting that doubling the sintering time had significant influence on the normal grain sizes, where the grain size increased non- linearly with sintering time, whilst it had nearly no further impact on the grain size of the small grains neighboring abnormally large grains. This leads to the conclusion that a further prolongation of the sintering time within industrially reasonable limits is not a viable option to avoid the structural deficiencies at grain boundaries affected by abnormal grain growth. From the experiments, it can be concluded that abnormal grain growth in LLZO-10 powder develops at some point between around 1 hour of sintering time at 1175°C under Li excess. However, given all other parameters, sintering times below this threshold would lead to poor overall sintering behavior, low density and low cohesion, resulting in low ionic conductivity. One can hence conclude that overall, the disadvantages of abnormal grain growth cannot be circumvented by adapting the sintering time.

Variation of the sintering temperature

In a next step, the sintering temperature is now adjusted to better understand the reasons of abnormal grain growth and see if the abnormal grain growth can be suppressed without changing the sintering activity of the small grains. The sintering temperature was therefore reduced step-wise from 1175 °C (see **Figure 4.1.12**) to 1150 °C, 1100 °C, 1050 °C, 1025 °C, and 1000 °C. BSE-SEM images of the cross-section are shown below for each sample sintered at the different temperatures for 5 hours. The images were chosen to show an area where large grains are surrounded by small grains for a better comparison. After having shown the results of each experiment individually in the above variation of the sintering time to illustrate the approach, the present sub section will present all results at once for comparison.

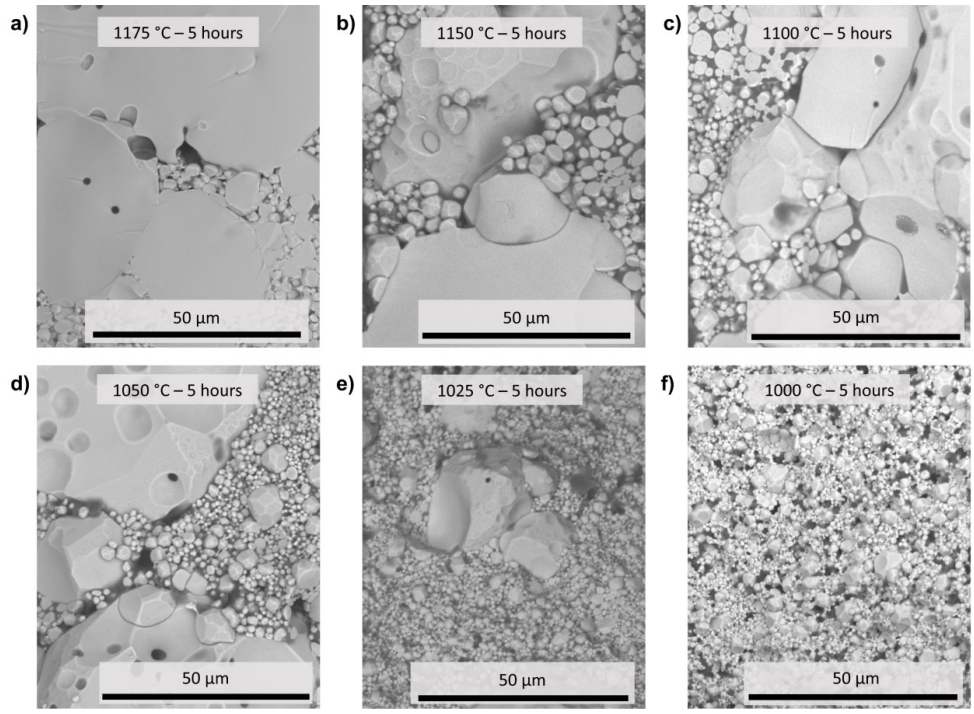

Figure 4.1.17: BSE-SEM image of LLZO-20 tape cross-section (fractured, un-polished) sintered in a Li saturated crucible is shown to evaluate the grain growth, grain shape and grain size. Here, sintering parameters were as following: **a)** 1175 °C for 5 hours, **b)** 1150 °C for 5 hours, **c)** 1100 °C for 5 hours, **d)** 1050 °C for 5 hours, **e)** 1025 °C for 5 hours and **f)** 1000 °C for 5 hours with LLZO-20 powder.

The BSE-SEM images reveal three main variations between the tapes with decreasing sintering temperature: First, for sintering temperatures below 1175 °C, large grains tend to break intergranularly rather than intragranularly. Second, it appears that large grains become smaller with decreasing temperature, although a grain size distribution must first be evaluated to verify this assumption. Third, indication of a large grain can still be observed at a sintering temperature as low as 1025 °C, even if it is very small compared to the other temperatures, while no abnormal grain can be found at 1000 °C. Finally, the small grains at the lowest two temperatures are very small compared to the other temperatures. Densities were estimated by ImageJ software and are overall decreasing for the different temperatures. 1175 °C for 5 hours reaches 87%, 1150 °C reaches 83%, 1100 °C without abnormal grain growth was not measured, 1050 °C reaches 76%, 1025 °C reaches 74%, and 1000 °C reaches only 72%.

Grain size distributions were analyzed for the different sintering temperatures, analogue to the analysis of the time variation. The detailed grain size distribution for each temperature is shown in **Figure 4.1.18**.

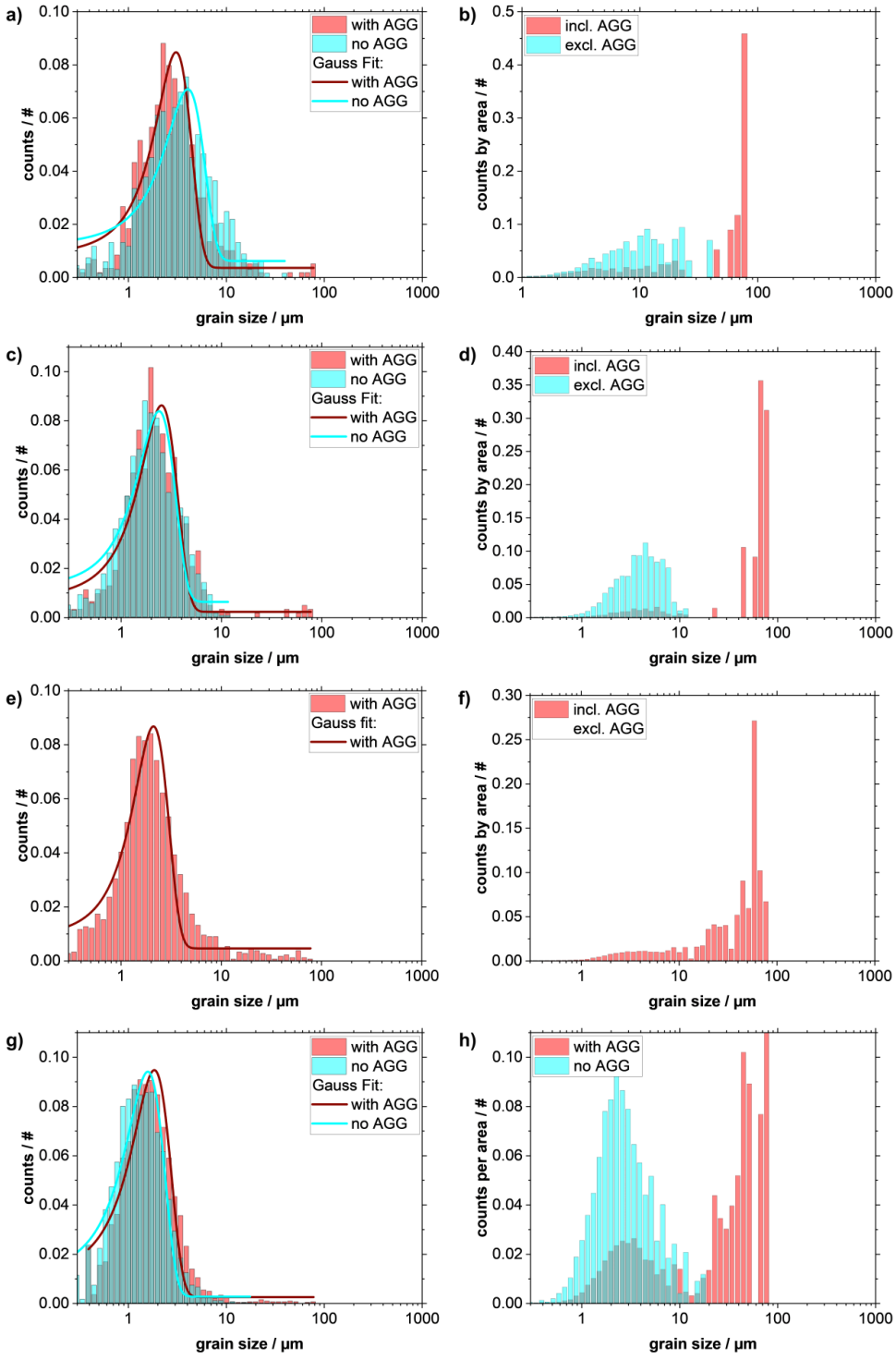
a)
with AGG
no AGG
Gauss Fit:
with AGG
no AGG
counts / #
grain size / µm
b)
incl. AGG
excl. AGG
counts by area / #
grain size / µm
c)
with AGG
no AGG
Gauss Fit:
with AGG
no AGG
counts / #
grain size / µm
d)
incl. AGG
excl. AGG
counts by area / #
grain size / µm
e)
with AGG
Gauss fit:
with AGG
counts / #
grain size / µm
f)
incl. AGG
excl. AGG
counts by area / #
grain size / µm
g)
with AGG
no AGG
Gauss Fit:
with AGG
no AGG
counts / #
grain size / µm
h)
with AGG
no AGG
counts per area / #
grain size / µm

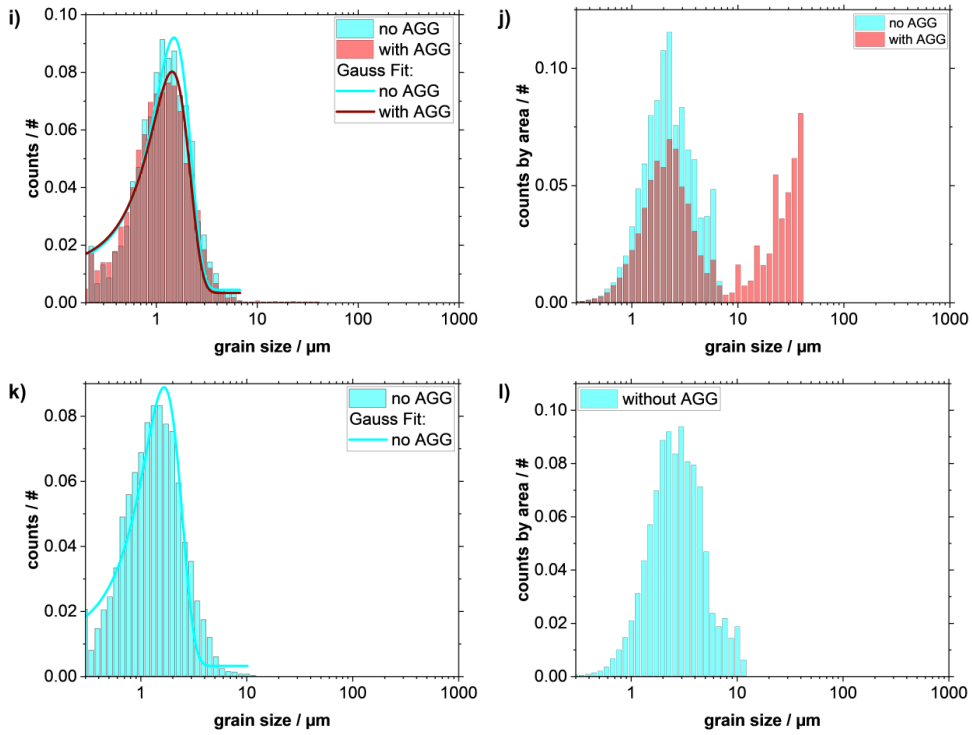

Figure 4.1.18: Grain size distribution of the sintered tapes. The grain size distribution was evaluated by ImageJ and shows the grain sizes for images without abnormal grain growth and with abnormal grain growth. Left shows the grain size distribution by counts with a Gaussian fit, while right shows the grain size distribution normalized to the area for **a)+b)** 1175 °C, **c)+d)** 1150 °C, **e)+f)** 1100 °C, **g)+h)** 1050 °C, **i)+j)** 1025 °C, and **k)+l)** 1000 °C, all for 5 hours.

For the grain size distribution analysis at 1100 °C for 5 hours, no images without large grains were available, while for the grain size distribution analysis at 1000 °C for 5 hours, no abnormal grain growth was observed.

In addition, the results shall be presented below as a summary of a) the grain size distribution with and without abnormally large grains, b) the maximum grain size of the abnormally large grains and c) the density in dependency of the grain size in areas without abnormal grain growth.

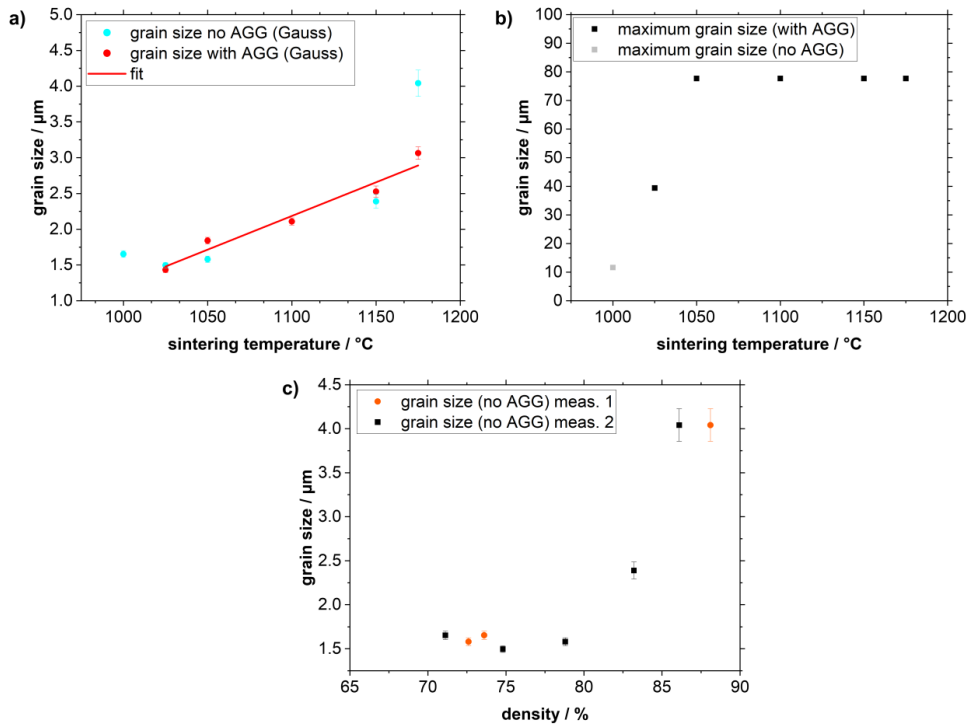

Figure 4.1.19: a) Gauss fit peak values for the grain size distribution of the sintered tapes over sintering temperature, differentiating between areas with and without abnormal grain growth. **b)** Maximum grain sizes in the tape over the sintering temperature. **c)** Gauss fit peak values for the grain size in areas without abnormal grain growth depending on the tape density.

It is interesting that the grain size distribution in areas without large grains is increasing strongly non-linearly with increasing temperature above 1050 °C, whereas the average grain size difference between 1000 °C and 1050 °C is near zero, considering the error margin of ImageJ when detecting very small grains. This means that on the one hand, increasing temperature enhances the grain growth massively, whereas no effect can be seen at temperatures below a threshold of 1050-1150 °C. When comparing this with the grain size distributions of tape areas that are affected by abnormal grain growth, it becomes obvious that the growth of the small grains neighboring abnormally large grains is nearly linear with temperature. The slope of ca. 0.01 µm K^{-1} (at 5 hours sintering time) is much lower than the growth rate of the non-affected grains at higher temperatures, though. At low temperatures, however, the small grains neighboring abnormally large grains start at the same size and then tend to be larger than grains that were grown normally, before normal grain growth takes over at temperatures higher than 1150 °C. This difference in growth dependency on temperature is very interesting and might imply different growth mechanisms. The growth of the abnormal grains themselves was found to start at temperatures of 1025 °C with a maximum size of 40 µm. As soon as 1050 °C were reached, the maximum grain size does not change anymore and is stable at 77 µm.

To summarize, abnormal grain growth takes off at 1050 °C with first traces occurring at temperatures as low as 1025 °C. The largest grain size of 77 µm does not depend on temperature anymore above 1050 °C. Whilst the undesired small grains around the abnormally large grains grow linearly with temperature, the average grain size of tape areas without large grains increases significantly around 1150 °C and nearly no growth is observed at lower temperatures. This means that even if low temperatures are able to suppress abnormal grain growth, such temperatures also inhibit an acceptable overall sintering performance. Similar to the sintering time variation, a variation of the sintering temperature is hence not a suitable option to avoid abnormal grain growth in well-sintered separator tapes. The densities achieved for the grain sizes without abnormal grain growth follow the exponential curve of density and grain size, although the density is only a rough estimation and probably lower than the actual one (see chapter 3.2.5).

Potential causes of LLZO abnormal grain growth in sintering atmosphere saturated by LiOH

The size of the abnormally large grains increases with both sintering time and temperature independently. This indicates that an energy-related cause leads to the abnormal grain growth. Comparing the results with literature, Kim *et al.* found large grains and suggested that an Li-Al-O phase may lead to abnormally large grains.[123] Zhou *et al.* found a similar abnormal grain growth by intentionally adding Li_5AlO_4 as a sintering additive to their LLZO.[237] They suggest that Li_2O is formed next to a molten Li-Al-O phase, resulting in a gas-liquid-solid transport. They achieved relative high densities >94% at 1050 °C, which is in the same region as observed here. The LLZO in the above experiments is doped with Al, and the additional Li excess was observed to change the microstructure towards abnormally large grains. It is therefore suggested that a similar mechanism could be at work here for the tapes. Li-Al-O phase diagrams shows that liquid phases form, starting at temperature ranges of 1055-1065 °C[238] respectively 1334 K[239] (1060 °C). In a phase diagram, these liquid phases occur towards a higher content of Li compared to Al, which could explain why the abnormal grain growth is only visible with an additional Li source. The fact that the reported liquid phase temperature is slightly higher than the temperature of 1025 °C at which first traces of abnormal grain growth were observed might be explained by an overshooting of the furnace temperature: The furnace has been observed to overshoot considerably at the end of the heat-up process with a ramp of 10 K min^{-1}, and an overshoot of only 2.9% would suffice at 1025 °C to enable liquid phase formation. This would imply that a liquid phase occurs during sintering, which would completely change the sintering mechanism. This statement is also supported by the above observation that the sintering behavior and growth rate over temperature is very different for small grains in direct neighborhood of abnormally large grains, which would hence be affected by the liquid phase, and grains in other areas which are not affected by abnormal grain growth.

In order to prove that this hypothesis is plausible, a secondary Li-Al-O phase should be confirmed in the samples. Although no secondary phase was detected in the XRD pattern, this phase may still be present in a small amount due to the low doping of Al-ions in the LLZO. This would also explain the abnormal grain growth in only parts of the tapes, since 10-15 vol% of liquid phase must be given for complete rearrangement[98,240]. To further investigate whether a secondary phase of Li-Al-O phase can be found in the tapes, an area between two large grains is examined by EDX measurement. The polished

cross-section of the tape was previously used in EBSD measurements to detect the single crystal of a large grain. The same tape is now analyzed by EDX to see if Al-ions can be found in this area.

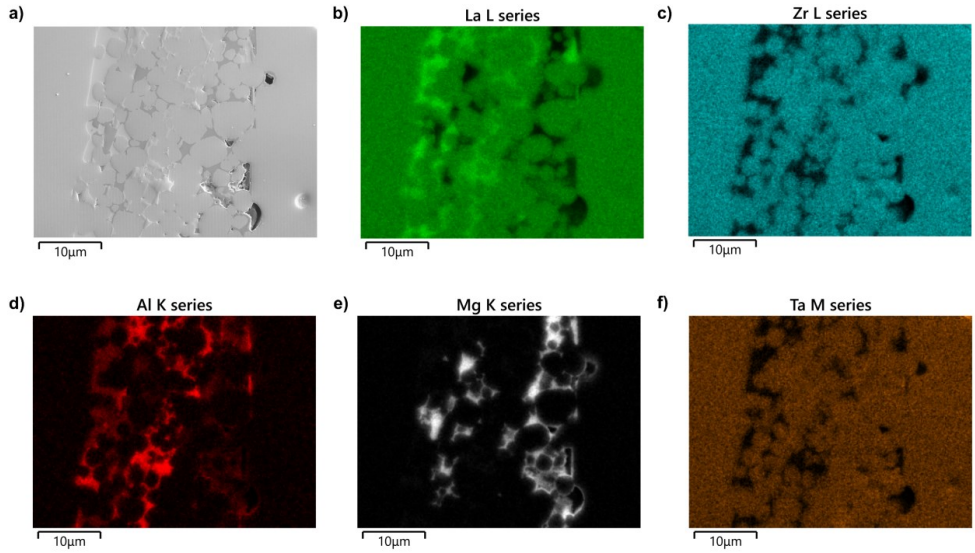

Figure 4.1.20: Polished cross-section of a sintered tape (LLZO-10, milled with H_2O and LiOH and sintered at 1175 °C for 10 hours. **a)** shows an SE-SEM image of the cross-section between two large grains of the abnormal grain growth, while **b)-f)** show the EDX mapping for La, Zr, Al, Mg and Ta, respectively. This image was taken by Dr. Doris Sebold.

The analysis of the SE-SEM image in **Figure 4.1.20 a** already shows three different phases. The dominating phase of the large grains in the right and left part of the image as well as in the circular grains in the center, displayed in medium gray, is cubic LLZO as the XRD has shown above. A lighter gray phase and a darker gray phase are further found between the grains. Both additional phases appear to have formed from liquid phases which can be considered a strong indication for the above liquid phase hypothesis. The EDX measurement shows a homogenous distribution for La, Zr and Ta in both the large grains and the small grains, confirming that this is LLZO. The lighter gray phase corresponds to a La-rich phase with additional Al. The dark gray phase corresponds to Al and Mg signals in the EDX analysis. The Mg impurity in the sample can be explained by the MgO plate used in the crucible, which may diffuse through the LLZO powder bed into the tapes. The presence of La particles has been observed before in some batches of LLZO processed in-house and may indicate room for improvement regarding the stoichiometric weighing.

To complement the analysis, also the grain boundary between two large grains without any possible phase impurities was analyzed. In this area, there are no small particles because two large grains are in direct contact with each other. The idea is that impurities at the grain boundary will allow a better understanding of what is causing the abnormal grain growth. The baseline for this analysis is the same area that was examined for the analysis of a single crystal in a large grain in the EBSD measurement (see chapter 4.1.2). This area, which was analyzed by EBSD measurement in **Figure 4.1.8**, is now

measured by EDX, to assess whether Al, Mg, and La are also present at the grain boundary of the two large grains.

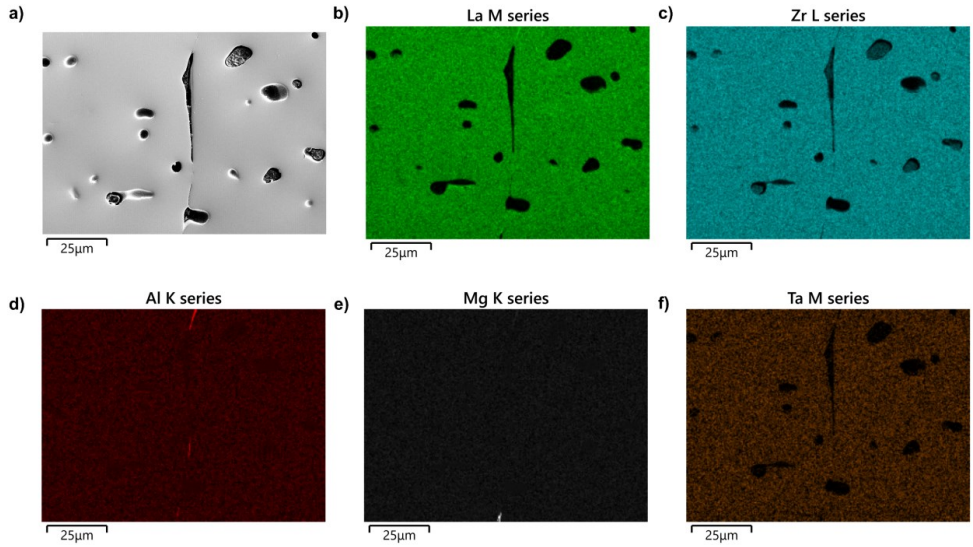

Figure 4.1.21: Polished cross-section of a sintered tape (LLZO-10, milled with H_2O and LiOH and sintered at 1175 °C for 10 hours. **a)** shows an SE-SEM image of the cross-section of the grain boundary between two large grains of the abnormal grain growth, while **b)-f)** show the EDX mapping for La, Zr, Al, Mg and Ta, respectively. (Image taken by Dr. Doris Sebold.)

The EDX measurement shows a clear homogeneous distribution for the elements La, Zr and Ta all across the large grain areas, suggesting that the grains are composed of LLZO. Again, Al in combination with La is visible between the large grains at the grain boundary, where the large particles are close together. At the very bottom of the image, also Mg was found between the large grains, together with Al. Both figures hence show the same phase compositions, independent of the presence of small grains between the large grains.

The results suggest that the cause for the abnormal grain growth at least in the above experiments was not a liquid Li-Al-O phase as suggested by Kim *et al.*[123] and assumed before: The additional phase areas would therefore need to contain only Al and O plus Li which is not detectable in the above EDX analyses. Even if both detected secondary phases contain Al, they both do contain an additional element, either La or Mg. La could have been explained as solid particles which may just be transported in the liquid Li-Al-O phase of interest. However, this would imply that solid La particles should also be transported in the second liquid phase which is not the case as it only consists of Mg, Al, O and probably Li, but not La. This in turn suggests that a liquid Li-Al-Mg-O phase may have been formed. Cross-referencing the sintering temperatures used above against a Li-Al-Mg-O phase diagram[239] confirms that: Li-Al-Mg-O does indeed have a liquid phase that forms at 1060 °C at elevated Li content. The other secondary phase, consisting of La, Al and O, is unlikely to be an La-Al-O compound as its melting point is considerably higher than the temperatures reached[241]. It is therefore assumed that it is actually a Li-La-Al-O phase and that the Li content in the compound reduces its melting point to such an extent that

it becomes liquid at the above sintering temperatures. The exact melting point of Li-La-Al-O could not be determined as, to the best of the author's knowledge, no phase diagram of Li-La-Al-O exists in literature. It is indicative for this theory, however, that both Li-Al-O and Li-Al-Mg-O show a very similar behavior where the melting point is reduced to 1060-1073 °C in both cases by elevated Li contents. The sintering temperature of 1025-1050 °C at which abnormal grain growth was first observed does not exactly match the reported melting temperatures, but is close enough considering the observed temperature overshoot of the furnace, especially given that the majority of the abnormal grain growth was observed above 1050 °C.

Therefore, it is concluded that the Li excess changed both the Li-Al-Mg-O and Li-La-Al-O phase compositions such that liquid phases could form at temperatures around 1060 °C which then caused the observed abnormal grain growth. Even if the Mg and La impurities might possibly be resolved by using another crucible plate and an improved stoichiometric weighing, the formation of a potentially liquid Li-Al-O phase as observed by Kim *et al.*[123] and Zhou *et al.*[237] could not be avoided as long as Al-doped LLZO was used. Abnormal grain growth can then only be suppressed by two means: Either by sintering temperatures significantly lower than 1050-1060 °C or by reducing the Li excess and hence the Li content in the secondary phases such that the areas of the low melting points of the secondary phases are not reached anymore. The first did lead to poor overall sintering behavior in above experiments, even if mechanical pressure might induce further densification, and the second is not an option in many cases as re-lithiation is an integral part of the recovery of cubic LLZO structures in the recycling of waste streams in battery production processes.

Controlled abnormal grain growth to obtain coarse-grained tape

As an addition to the goal of understanding abnormal grain growth in LLZO under Li excess, it should be mentioned that the production of tapes with 100% large grains is possible as well. By sintering LLZO-20 powder with the optimized milling at the sintering temperature of 1175 °C for 10 hours, it was possible to produce a complete tape with large grains (see **Figure 4.1.22**). The grain size reached over 300 µm. When the tape was prepared for a symmetrical cell assembly, the tape broke, as shown in the figure. It is known that mechanical stability decreases with abnormal grain growth.[232] The grain boundaries are not as stable as the bulk material, and due to the fact that the grain size is larger than the thickness of the tape, a single fractured grain boundary cause the tape to break at this point. One possibility would be to create a glass phase that sits at the grain boundaries to increase mechanical stability.[242] In the present case, the handling was not suitable for further processing into battery components. With the given process, it was also not possible to enhance grain growth further to obtain a single crystal with a suitable diameter as a battery component. Therefore, the experiments were stopped when the cause of the abnormal grain growth was found.

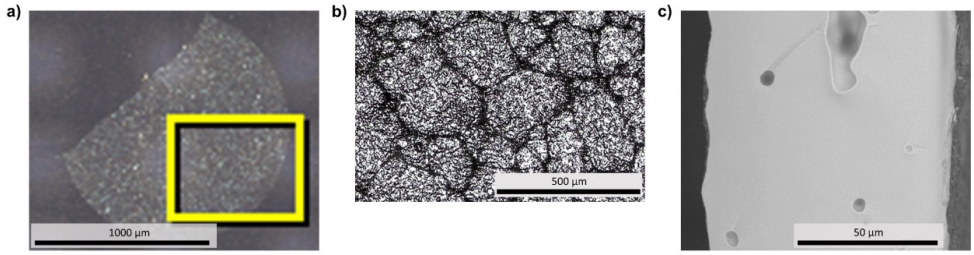

Figure 4.1.22: a) Image of the top surface of tape after sintering at 1175°C – 10h with LLZO-20, with **b)** zoom in and **c)** a BSE-SEM image of the cross-section of tape (fractured, un-polished).

Subsection Summary

In this subsection, the abnormal grain growth was further analyzed. The largest grain size of an abnormal large grain was about 350 µm, but due to the increased brittleness of the tapes, no electrochemical tests could be performed. Assuming that smaller grain sizes between 20-40 µm are preferable for the ionic conductivity[230], abnormal grain growth is not the optimal result for a sintered tape. It was shown that abnormal grain growth can be avoided by a reduction of the sintering time and temperature, but only at the cost of a significant deterioration of the sinterability of the overall tape. When investigating the causes for abnormal grain growth in LLZO:Al,Ta, EDX measurements revealed Al and Mg impurities at the large grain boundaries, suggesting that both an Li-Al-Mg-O phase and probably an Li-La-Al-O phase, which are liquid close to the investigated sintering temperatures, lead to the abnormal grain growth. Whilst the Al dopant was already present in the LLZO tape, the Mg propagated from the MgO plate in the crucible during sintering and La may stem from the LLZO synthesis. The Li excess used for the recovery of the cubic LLZO then shifted the secondary phases Li-Al-Mg-O respectively Li-La-Al-O to a higher Li content and hence made liquid phases possible. This explanation is backed by similar observations made by Kim *et al.*[123] and Zhou *et al*.[237]

4.1.4 Direct re-lithiation of $Li_7La_3Zr_2O_{12}$ waste material

The following subsection was published in the Journal of Power Sources (vol.609) under the title "Waste minimization in All-Solid-State battery production via re-lithiation of the garnet solid electrolyte LLZO" and was also part of a student work, where the experiments were performed by the master's student under supervision and guidance of the author.[9]

In subsection 4.1.2, it was shown that a Li-rich atmosphere can prevent Li loss of LLZO during heat treatment, avoiding the formation of the pyrochlore phase $La_2Zr_2O_7$, and can also re-lithiate this pyrochlore phase back to the cubic LLZO phase. Furthermore, it was discovered that LiOH as an additional Li source during sintering leads to abnormal grain growth. In collaboration with the work of Touidjine *et al.* to which the author contributed, it was found that the addition of Li_2CO_3, following a similar approach as shown in the above chapter, does not lead to abnormally large grains and can be controlled.[243] Therefore, the following direct recycling route by re-lithiation was evaluated based on the selection of Li_2CO_3 as an additional Li source. It shall now be applied to real LLZO waste material in both powder and green tape form.

Real waste material of the in-house synthesis was used to show that re-lithiation works on LLZO production waste material by following the same route as outlined previously (see chapter 3.1). The following figure shows the pristine LLZO-10 powder immediately after synthesis, the aged LLZO-10 powder (LLZO-p) and the aged LLZO-10 green tapes (LLZO-t) as aged tape and as powder prepared as described above.

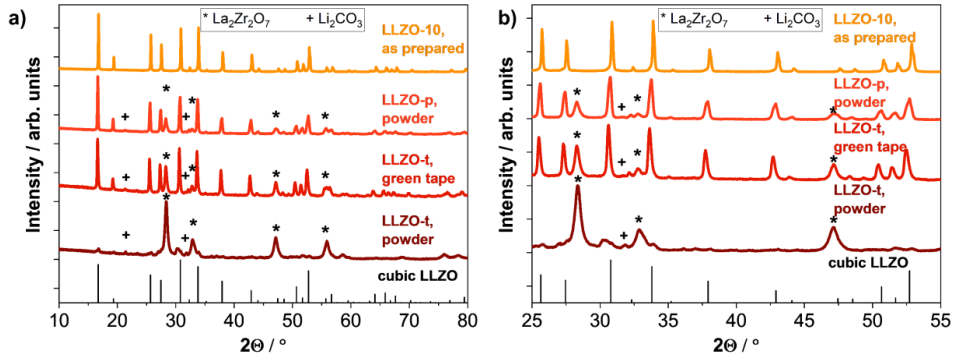

Figure 4.1.23: XRD patterns of LLZO-10 powder as prepared, and the aged LLZO-p powder, and aged LLZO-t green tapes and powder. For analysis, the cubic LLZO reference (ICSD: 182312)[52] is given, while **a)** shows the total pattern, and **b)** is zoomed-in to show the impurity phase in a higher detail. Adapted from [9] is licensed under CC BY 4.0 (https://creativecommons.org/licenses/by/4.0/).

XRD analyses of the different LLZO stages show different secondary phase formations. Freshly synthesized LLZO powder shows a cubic LLZO structure without secondary phases. The LLZO-p powder shows a high impurity of the pyrochlore phase $La_2Zr_2O_7$, at its main reflection. LLZO-t (green tape) shows also the pyrochlore phase of $La_2Zr_2O_7$, due to earlier heat treatment of the powder that was initially used for the green tapes, and both of the above show also Li_2CO_3 impurity. For the burnt-out-

organic powder of the green tape (LLZO-t powder), the XRD pattern shows reflections for the pyrochlore phase of $La_2Zr_2O_7$. The LLZO has been destroyed and is only vaguely seen in the pattern as well as Li_2CO_3.

It could hence be demonstrated that the aged LLZO powder and aged LLZO green tape powder are indeed suitable candidates for an in-production recycling process of out-of-specification LLZO material. Using this material, the process to produce a free-standing sintered LLZO separator tape was followed as usual, except for the heat treatment as it is not required here anymore: For the LLZO-p powder, a slurry was mixed, a tape was cast and the tapes were then sintered, with an additional Li source of Li_2CO_3. The ratio of LLZO to Li_2CO_3 was set to 1:0.55 by mass, meaning that 17% of the initially needed Li were added. The crucibles were not saturated with Li this time. The LLZO-t powder was first heat treated to remove the organics and wet-ball milled to the adjusted particle size (see **Figure 3.1.2**). Afterwards, it was treated in the exact way as the LLZO-p powder. The only difference consists in the sintering step, where the additional amount of Li was set to a higher initial value due to the nearly complete absence of the LLZO phase: The ratio of LLZO to Li_2CO_3 was set to 1:2.22 by mass, meaning that around 70% of the initially needed Li were added. Furthermore, the sintering parameters were changed to 1185 °C (original 1175 °C) and 24 hours (original 10 hours) for both LLZO-p green tapes and LLZO-t green tapes. The dwelling time was extended to make sure that the LLZO is completely re-lithiated throughout the entire tape. After sintering of the green tapes freshly produced from the old powders, XRD measurements were made to see if the re-lithiation was successful.

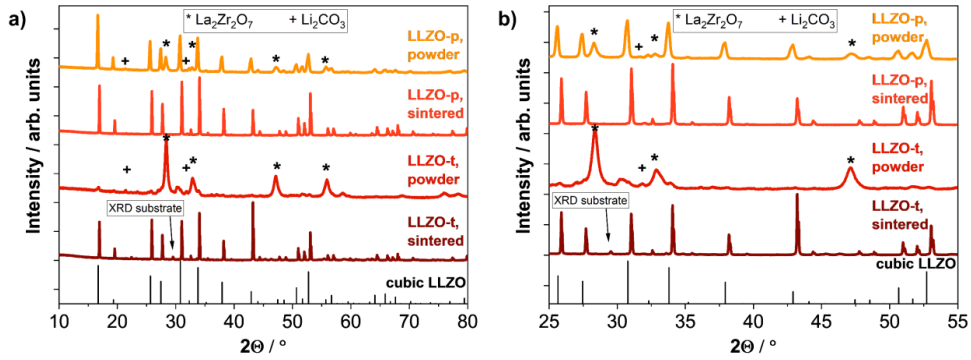

Figure 4.1.24: XRD patterns of LLZO-p/LLZO-t powder and the sintered tapes. For analysis, the cubic LLZO reference (ICSD: 182312)[52] is given, while **a)** shows the total pattern, and **b)** is zoomed-in to show the impurity phase in a higher detail. Adapted from [9] is licensed under CC BY 4.0 (https://creativecommons.org/licenses/by/4.0/).

The XRD analysis of the sintered LLZO separators of the re-processed LLZO-p and LLZO-t- powders both show a cubic LLZO phase without any traces of a $La_2Zr_2O_7$ impurity which was still seen before. The LLZO-p sintered tape additionally shows the Li_2CO_3 phase. This XRD analysis proves that the re-lithiation of degraded LLZO with the cubic structure was successful. The approach hence makes it possible now to convert a fully formed $La_2Zr_2O_7$ phase into a pure cubic LLZO phase by adjusting the Li content only during the final sintering step. Furthermore, the approach is simple and does not require additional hardware or process expertise beyond what is used already for the initial synthesis. The fact

that only small changes are required to re-lithiate waste material offers the possibility of a straightforward integration into the already existing process.

The thickness of the tapes was between 175 and 190 µm for both LLZO-p and LLZO-t powders. The slight variation in particle size distribution for the LLZO-p and LLZO-t powders explains the difference in thickness in the green tape, which is then also still visible in the sintered tape. The sintered LLZO separators were analyzed further to investigate for potential changes in the microstructure or abnormal grain growth as seen before.

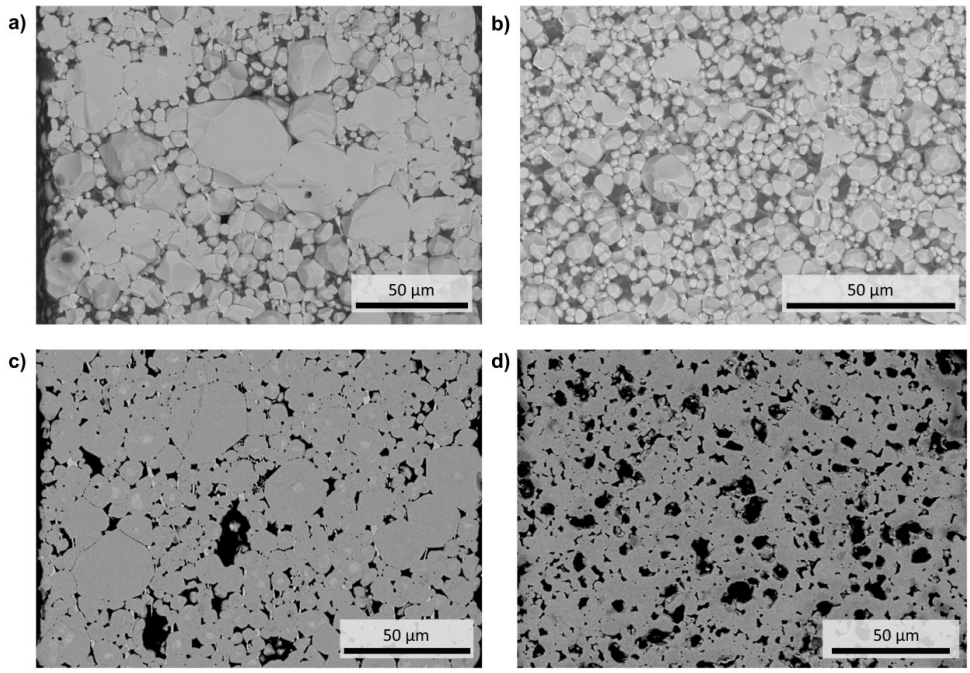

Figure 4.1.25: BSE-SEM images of sintered tapes after re-lithiation and of polished cross-section of sintered tapes after electrochemical testing, the Li metal anode was carefully removed before embedding**. a/c)** shows the LLZO-p sample, while **b/d)** shows the LLZO-t sample. **c)** and **d)** were taken from [9] is licensed under CC BY 4.0 (https://creativecommons.org/licenses/by/4.0/).

The BSE-SEM analyses of the un-polished and polished cross-sections show different microstructures for both tapes. There seem to be more large grains in the LLZO-p tape than in the LLZO-t tape. Furthermore, the density of the tapes is the most revealing change between the LLZO-p and LLZO-t samples. For LLZO-p, the tapes show a mixture of small and large pores and grains, yielding a relative density of nearly 87%. There are more pores visible in the LLZO-t sample and the relative density reaches only 76%. That means that both samples achieve a lower density than tapes fabricated in the same process but with fresh LLZO powder which was reported as 92.8%.[107] The low densification indicates insufficient sintering activity. One reason could be the impact of the surface of the LLZO particles: The particle surface might have changed due to either residues of the organics burn out in the

green tape waste, or due to the high amount of Li_2CO_3 in the crucible, leading to an insufficient sintering of the tapes.

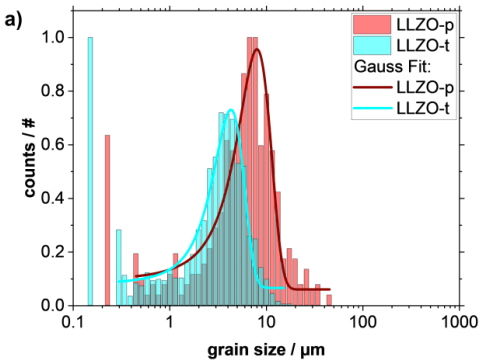

Figure 4.1.26: Grain size distribution of the sintered tape of LLZO-p and LLZO-t, shown above. The grain size distribution was evaluated by ImageJ and a Gaussian fit is indicated.

Finally, grain size distributions of the tapes were produced using ImageJ, as described in chapter 3.2.3, to quantify the grain size differences observed in the BSE-SEM-images above. The maximum grain size for LLZO-p tapes reached nearly 45 µm, while the maximum grain size for LLZO-t tapes reached only 13 µm. The grain size distribution peaks at 8 µm and 4.3 µm respectively. It is quite homogeneous for both cases, shifted to smaller grain sizes for LLZO-p samples. This confirms the observation from the BSE-SEM-images and the density comparison that sintering was more effective in the LLZO-p tape.

Electrochemical tests of the sintered separators were carried out to check performance of the re-lithiated LLZO. Both sintered tapes of LLZO-p and LLZO-t were used to construct a symmetric cell (Li|LLZO|Li).

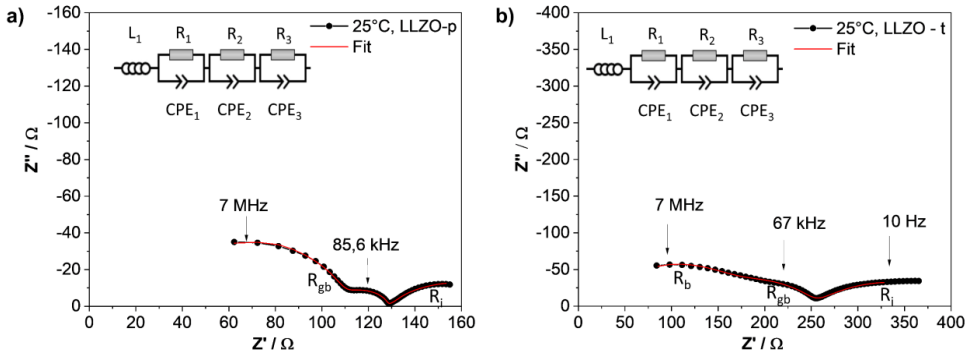

Figure 4.1.27: Electrochemical Impedance Spectroscopy of symmetrical Li|LLZO|Li cells measured at 25 °C. **a)** the spectra of LLZO-p sample, reaching a total ohmic resistance of < 160 Ω and **b)** shows the spectra of the LLZO-t sample, reaching a total ohmic resistance of < 375 Ω. Adapted from [9] is licensed under CC BY 4.0 (https://creativecommons.org/licenses/by/4.0/).

The symmetric cells were tested with impedance measurements at 25 °C to evaluate the electrochemical response of the recycled material. For the LLZO-p sintered tapes, the measurement shows three semi-circles at room temperature. The bulk conductivity of the LLZO-p sample cannot be seen here as it exceeds the suitable frequency and temperature boundaries, but the grain boundary resistance is at 47 Ω (10^{-7} F). The ionic conductivity is calculated using equation 3.11 and yields a value of 0.21 mS cm^{-1} at room temperature. This is in the range of various tape cast separators, although at the lower end of it. Considering the comparably low density in the tape, however, the ionic conductivity is quite high. For LLZO-t sintered tapes, similar measurements were made at room temperature. Again, three semi-circles were visible at room temperature, but this time the grain boundary resistivity was determined to be as high as 95 Ω (10^{-9} F), followed by the lithium interface resistivity (10^{-4} F). The ionic conductivity of the LLZO-t sintered tape is calculated as 0.14 mS cm^{-1}. This means that only 66% of the ionic conductivity of the LLZO-p tape was achieved in the LLZO-t tape, which is expected due to the even lower density of the LLZO-t tapes. Also the higher grain boundary resistivity of the LLZO-t samples may serve as an indication of the lower density.

In order to measure the critical current density, stripping and plating are performed for each of the LLZO-p and LLZO-t separators in a symmetrical cell with Li on both sides. The ionic conductivity is measured again at 60 °C beforehand, since the CCD measurement is also performed at 60 °C.

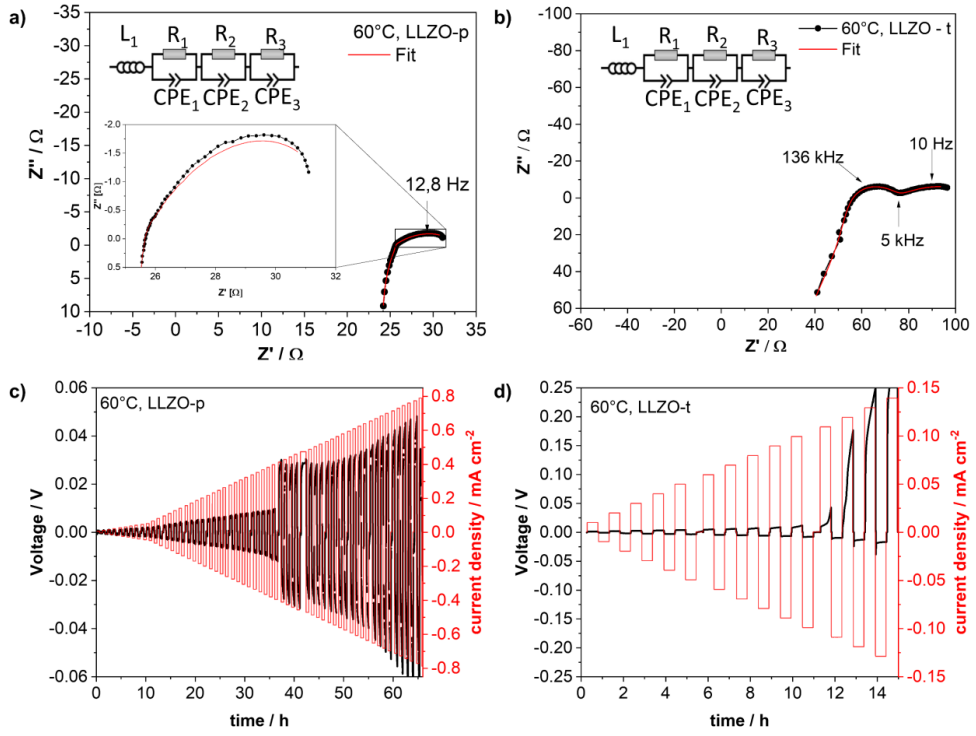

Figure 4.1.28: Electrochemical Impedance Spectroscopy of symmetrical Li|LLZO|Li cells measured at 60 °C. **a)** the spectra of LLZO-p sample, and **b)** shows the spectra of the LLZO-t sample. CCD measurement on a symmetrical Li|LLZO|Li cell at 60 °C **c)** shows the LLZO-p tape, while **d)** shows the LLZO-t tape. Red and black

lines indicate applied current density and change in cell polarization, respectively. CCD has been reached, when voltage drops, polarization is not considered. Adapted from [9] is licensed under CC BY 4.0 (https://creativecommons.org/licenses/by/4.0/).

For the sintered tapes with a higher density (LLZO-p), a critical current density of 750 µA cm^{-2} at 60 °C was reached. This is quite impressive, especially given the low density, as this value exceeds most current densities reported for tape-cast materials. The highest reported value for a pellet is still 1 mA cm^{-2} measured at room temperature, which translates to even higher values at 60 °C since CCD is strongly influenced by temperature.[128] In order to make the above values more tangible, the present tapes are compared to reported values for tapes produced from LLZO with pristine powder, using the conventional process described by Rosen *et al.*[107]: The relative density is lower than the reported 92.8%[107] (here 87%) as is the ionic conductivity (here 0.21 mS cm^{-1} instead of 0.39 mS cm^{-1} as reported[107]). The critical current density is considerably higher though with here 750 µA cm^{-2} at 60 °C compared to 318 µA cm^{-2} at 50 °C[107]. Please note that the critical current density was measured at 50 °C by Rosen *et al.* whereas the reference temperature in this case is 60 °C, the critical current density is therefore difficult to compare.

In contrast to the LLZO-p separator, the LLZO-t separator has a much lower critical current density of 110 µA cm^{-2} at 60 °C. These CCD results are in line with the lower density in the microstructure as well as a lower ionic conductivity of the LLZO.

Sub-section summary

After mimicking LLZO waste material by reproducing the most common secondary phase $La_2Zr_2O_7$, Li excess of LiOH was used in the thermal treatment steps of the process including sintering to avoid or recondition pyrochlore phases, but showed an abnormal grain growth in the microstructure of the tape due to liquid Li-La-Al-O and Li-Al-Mg-O phases. Re-lithiation of LLZO powder from the pyrochlore phase was, however, successfully demonstrated. Now, real LLZO production waste material in the form of powder and green tape was used to show that this approach is successful when Li_2CO_3 is used as the Li source. The powder and green tape contained the pyrochlore phase $La_2Zr_2O_7$ after aging and heat treatments. The waste material was used in the same process as before, resulting in two green tapes from the waste powder respectively the green tape waste material. Both tapes were sintered with an additional Li source (Li_2CO_3) and the cubic LLZO phase was successfully recovered. The microstructure revealed the need for optimization of selected parameters in future processing, notably the separator produced from powdered waste tape but the direct re-lithiation as a cost effective and simple alternative to conventional scrap recycling was shown to be successful and could hold tremendous potential for future LLZO recycling. In the case of the critical current density, the separator tape produced from waste powder material outperformed even the one made from fresh LLZO.

4.2 Part II: Precursor route development

Having addressed the consumption of critical materials by introducing a direct re-lithiation route to reuse waste during production, the following section will consider two more challenges related to LLZO: the high energy requirements and production cost. The aforementioned process contains the synthesis of LLZO, which is subsequently subjected to a forming process, resulting in the production of the battery component. The synthesis of LLZO in a solid-state reaction as discussed above involves several milling and calcination steps prior to sintering. While the high energy consumption represents a challenge with regard to the environmental footprint, it also contributes to the overall process cost. Moreover, the necessity of lengthy calcination periods, which necessitate the use of large oven capacities, contributes to the aforementioned challenge. The following chapter will introduce an environmentally friendly, rapid, energy-efficient, and cost-effective process. This will be achieved by an *in-situ* synthesis of LLZO during sintering. The concept and necessary preliminary actions are first explained, and then the new route is demonstrated on composite cathodes and separators with various dopants. To build on the previous chapter, recycled material will finally be employed as a precursor in the novel process, with the synthesis of this material also being investigated for future development.

4.2.1 Concept of the new *in-situ* synthesis route

Chapter 4.2.1, 4.2.2, and 4.2.3 are partly based on the paper "Direct precursor route for the fabrication of LLZO composite cathodes for solid-state batteries" published in Advanced Science volume 11, 2024.[218]

Oxide ceramics, including LLZO, share a common disadvantage in their processing: They include at least one calcination step to create a pre-synthesized powder, which is then shaped to form the final battery component. Additionally, the long processing times related to the calcination would require significant furnace capacities when scaling up production, adding to another problem of LLZO, its high production cost. A novel synthesis route for LLZO is presented as a solution here, which addresses the two aspects. The core element of the new concept is a single-step *in-situ* formation of LLZO during sintering of the final battery component. This process fully eliminates the necessity for energy expenditure associated with pre-synthesized LLZO, as the green tape is composed of the precursor material only. A preceding milling step of the precursors ensures not only suitable particle sizes, but also homogeneously mixture. This enables the formation of a pure cubic LLZO structure in the tape during the sintering step as the only heat treatment of the final component. The scheme below illustrates this new concept against standard solid-state reaction and sol-gel synthesis as existing processes for preparing pre-synthesized LLZO powder.

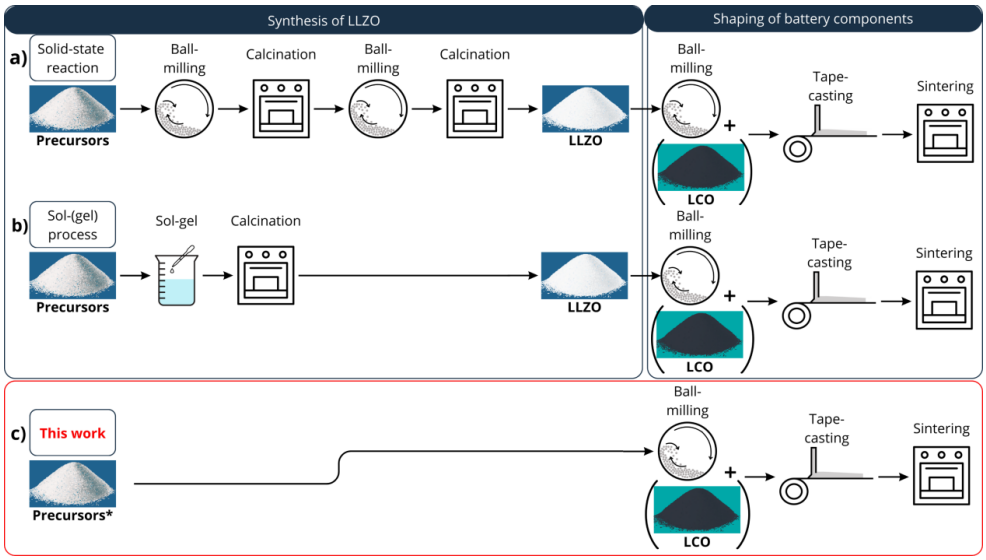

Figure 4.2.1: Schematic visualization of solid-state reaction, sol-gel process, and the route used in this work followed by a tape-casting and sintering step, adapted from [218] is licensed under CC BY 4.0 (https://creativecommons.org/licenses/by/4.0/).

The optimized wet-ball milling that was developed within the scope of this work (see chapter 3.1.1) is used here as well. The dry precursor powder was then used in the standard tape-casting process and underwent the final sintering step as previously described.

4.2.2 Pre-processing of the precursor material for the new *in-situ* synthesis

As explained above, all thermal treatments besides the final sintering step could be eliminated in the new process, as LLZO does not need to be pre-synthesized and therefore the risk of LLZO undergoing a Li^+/H^+ exchange is eliminated. Ball-milling of the precursors is still necessary though to mix the precursors evenly and achieve the desired particle size distribution for the slurry used during the tape-casting process. Moreover, a small particle size distribution necessitates a reduced energy input during the sintering process because of increased initial densification. The ball-milled precursor powder was analyzed via BSE-SEM images first (**Figure 4.2.2**) in order to investigate the particle size.

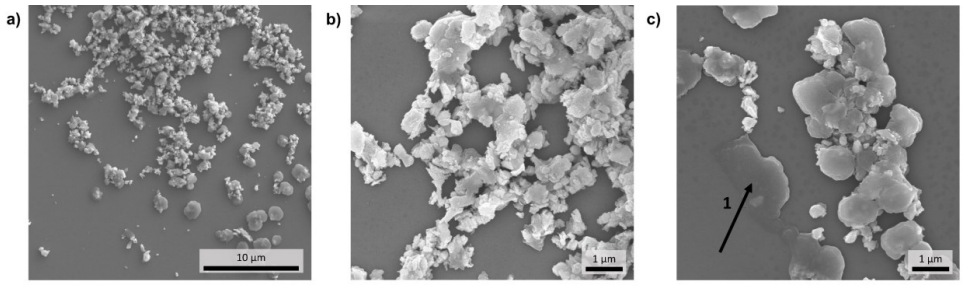

Figure 4.2.2: BSE-SEM image of a precursor powder on a Si wafer, after wet-ball milling with the optimized parameters. **a)** shows a lower magnification than **b)** and **c)**. Adapted from [218] is licensed under CC BY 4.0 (https://creativecommons.org/licenses/by/4.0/).

First of all, the BSE-SEM image confirms that the desired uniform grain size distribution of the precursor powder with diameters around 1 µm has been achieved by the ball-milling step. In the highest zoom level (**4.2.2 c**), a blurred shape can be discerned within the image though, highlighted by arrow 1. It is likely that these blurred shapes represent LiOH which will be assessed by EDX measurements below. Arrows display the locations of the EDX point measurements in an SEM image on the left as well as the EDX measurement for these points on the right. This assumption was proven by EDX measurements in the following.

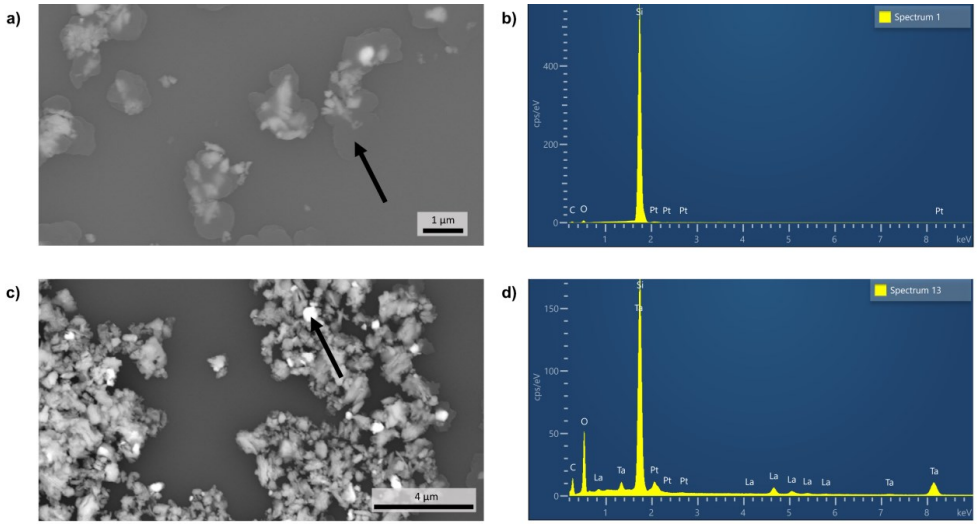

Figure 4.2.3: BSE-SEM images indicating the location of the point measurements of two different particles (**a+c**) and the resulting EDX (**b+d**). Adapted from [218] is licensed under CC BY 4.0 (https://creativecommons.org/licenses/by/4.0/).

The EDX measurements were taken on a blurred spot (**Figure 4.2.3 a**) and on a very bright spot with clear outlines (**Figure 4.2.3 c**). As anticipated, the EDX spectrum of the blurry point reveals only Si (the powder is placed on a Si wafer for measurements) and Pt, which was sputtered on the material to mitigate charging effects. It can be confirmed that the blurry particles are indeed LiOH, which is not detectable,

given that all other elements have been identified elsewhere (besides Al). The additional spectrum (**Figure 4.2.3 d**), in turn, clearly reveals the presence of Ta in addition to the Si signals caused by the backplate. Slight La background noise signals may be explained by the uneven surface of the particles, leading to possibly shifted reflections due to the EDX sensitivity of the detector. Further particles have been measured and confirmed the existence of all expected precursors (see **Figure 4.2.4**), besides Al which is present in minimal quantities only.

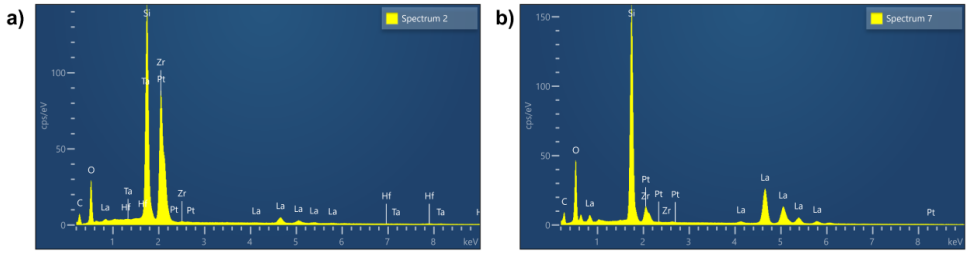

Figure 4.2.4: EDX of the precursor powder after milling for two different point analyses for La and Zr.

The EDX analysis, which is displayed alongside the Si element, also reveals the presence of Ta. Although Si and Ta are superimposed in the signal, more Ta and low La signals are registered. The remaining elements were not measured, as this sample lacked a polished cross-section and served solely to verify the particle size following milling. It could hence be shown that the preprocessing steps within the new *in-situ* route produce the expected outcomes. In particular, the ball-milling of the precursors does effectuate the desired degree of mixing and particle size without inducing the formation of undesired intermediate phases.

4.2.3 Application of the new *in-situ* synthesis route on composite cathodes

The precursor powder that was introduced above will now be used to tape-cast composite cathodes by adding ball-milled, pre-synthesized LCO to the slurry, as shown in **Figure 4.2.1**. The resulting composite cathode tapes will be analyzed to determine if they can compete with composite cathodes produced with pre-synthesized LLZO.

The gradient structure can be achieved by sequential tape-casting, described in chapter 3.1.2. The resulting green tape had a thickness of 100 µm and is sintered at a temperature of 1050 °C for 2 hours. XRD measurements of the sintered tape were taken and analyzed by a Rietveld refinement. In order to assess LLZO formation, additional XRD analysis was also performed on green tapes heated to 650 °C for 2 hours, and heated to 750 °C without holding time. The LLZO-rich side (2:1, LLZO:LCO) was measured to enhance the visibility of the LLZO reflections, which is of central interest in this chapter, compared to the LCO reflections, as it has to form first.

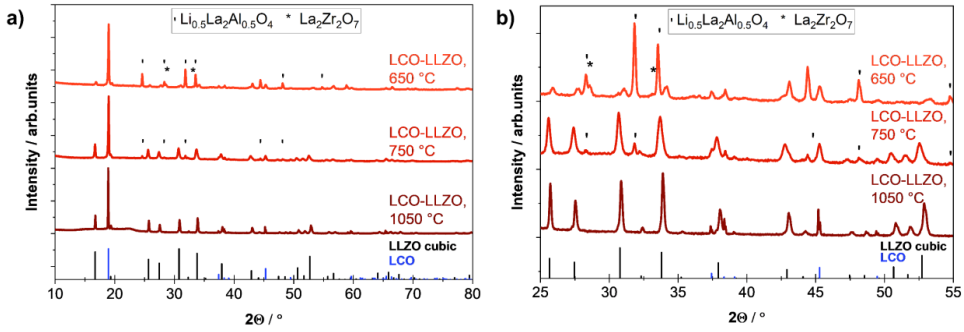

Figure 4.2.5: XRD pattern of tapes after heat treatment of 650 °C, 750 °C and 1050 °C with indication of side phases and the cubic LLZO structure (ICSD: 182312)[52] and LCO (ICSD: 29225) as references, adapted from [218] is licensed under CC BY 4.0 (https://creativecommons.org/licenses/by/4.0/).

As evidence for the *in-situ* synthesis of LLZO, intermediate products are expected to be detected at the forming temperatures of LLZO which are below the sintering temperature of 1050 °C targeted here. The measurement at 650 °C in **Figure 4.2.5** shows $La_2Zr_2O_7$ and $Li_{0.5}La_2Al_{0.5}O_4$. As mentioned in chapter 2.2.3, several studies have shown the formation of LLZO via $La_2Zr_2O_7$[82] and $Li_{0.5}La_2Al_{0.5}O_4$.[84] Chen *et al.*[83] investigated the LLZO formation process, and found a maximum amount of $La_2Zr_2O_7$ and $Li_{0.5}La_2Al_{0.5}O_4$ phases between 750 °C and 800 °C for LLZO:Al with similar precursors to this study. These reported intermediates match those found in this measurement, although the temperatures are slightly lower here. In this XRD measurement, Li_2ZrO_3 could not be detected[83], although it is a forming phase reported in literature, either because of the low XRD detection limit of about 5% or because it was not present.[81,82] The sintered tape at 1050 °C shows a cubic LLZO main phase, besides the LCO phase, confirming that not only intermediates but also the pure cubic LLZO structure was formed during sintering. The Rietveld refinement of the XRD data (see **Figure 4.2.6**) also suggests that 66% of LLZO:Ta and 34% of LCO are present, which is consistent with the expected 2:1 LLZO:LCO ratio. It can therefore be stated that the new *in-situ* synthesis of LLZO during the sintering step was successfully demonstrated for the first time.

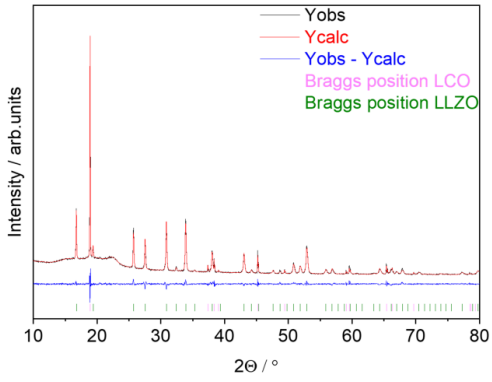

Figure 4.2.6: Rietveld refinement of the XRD pattern observed for the composite cathode LCO LLZO:Ta,Al. Adapted from [218] is licensed under CC BY 4.0 (https://creativecommons.org/licenses/by/4.0/).

Microstructural analysis of the composite cathode is then performed to evaluate the gradient structure, the sintering behavior of the LCO and LLZO grains, and grain size distribution.

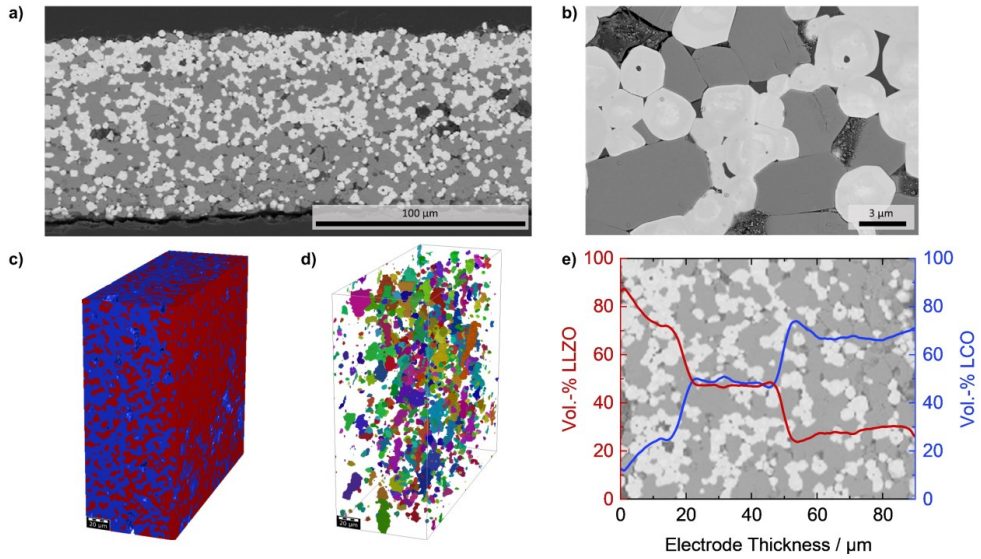

Figure 4.2.7: a) BSE-SEM image over a cross-section with the full thickness revealing the gradient structure of the composite cathode. **b)** BSE-SEM image with higher magnification. Results of micro x-ray tomography (µCT) analysis of the layered electrode in **c)** Segmented 3D structure with a visible gradient from LLZO-rich (blue) to LCO-rich (red) side. **d)** Analysis of pore connectivity performed with PoroDict. Different colors represent unconnected pore clusters. **e)** Distribution of solid electrolyte (LLZO) and active material (LCO) along the electrode thickness quantified via MatDict with an overlay of the BSE-SEM image, adapted from [218] is licensed under CC BY 4.0 (https://creativecommons.org/licenses/by/4.0/).

Analysis of the BSE-SEM image (**Figure 4.2.7a**) shows, that a gradient structure has been successfully fabricated across the whole thickness of the tape. It is remarkable that the relative density in the tape reaches values as high as 95% of the theoretical value (by ImageJ and micro x-ray computer tomography), even if LCO and LLZO are reported to have a low density when co-sintering[157,158] without additional pressure applied[103].Here, LLZO (bright) and LCO (dark) show a dense, highly sintered interface with a gradient structure from top to bottom. The LLZO-rich side with a ratio of 2:1 (LLZO:LCO) shows exactly 66% of the measured grains of LLZO (by µCT), similarly for the 1:1 and 1:2: ratios in the tape. Furthermore, the tape is vastly dense, and shows a good interface. In addition, the LLZO grains are interconnected, which helps with the Li transport. Analyzing the pores and grains, it seems that the pores are neither connected nor open to the surface (closed porosity), but have two kinds of sizes, in the range of 1 µm small pores and 10 µm large pores. Assuming that the small pores are unavoidable during sintering and densification, the large pores are of a different origin. LCO has a higher sintering activity, and sintering occurs at lower temperatures than for LLZO. LCO therefore creates a sintered matrix, where the LLZO particles are surrounded and LLZO sintering occurs in the restricted spaces.[157] This may limit the diffusion during the LLZO sintering, likely leaving the large pores behind. One possibility might be that the sequential layering during the tape-casting process could have induced air at the boundaries of the cast layers. Further analysis of the micro x-ray computer tomography,

however, shows that the large pores are found within the cast layers themselves, whereas the sequential tape-casting results in a low porosity between the different cast layers. This would mean that the slurry itself contains trapped air, whereas on the surface of each layer, which is already drying, the pores can be filled with the new slurry cast on top.

Following the above detailed analysis of the microstructure, the next analysis will focus on the interdiffusion of each element as it is a known weak spot in the co-sintering of LLZO and LCO.

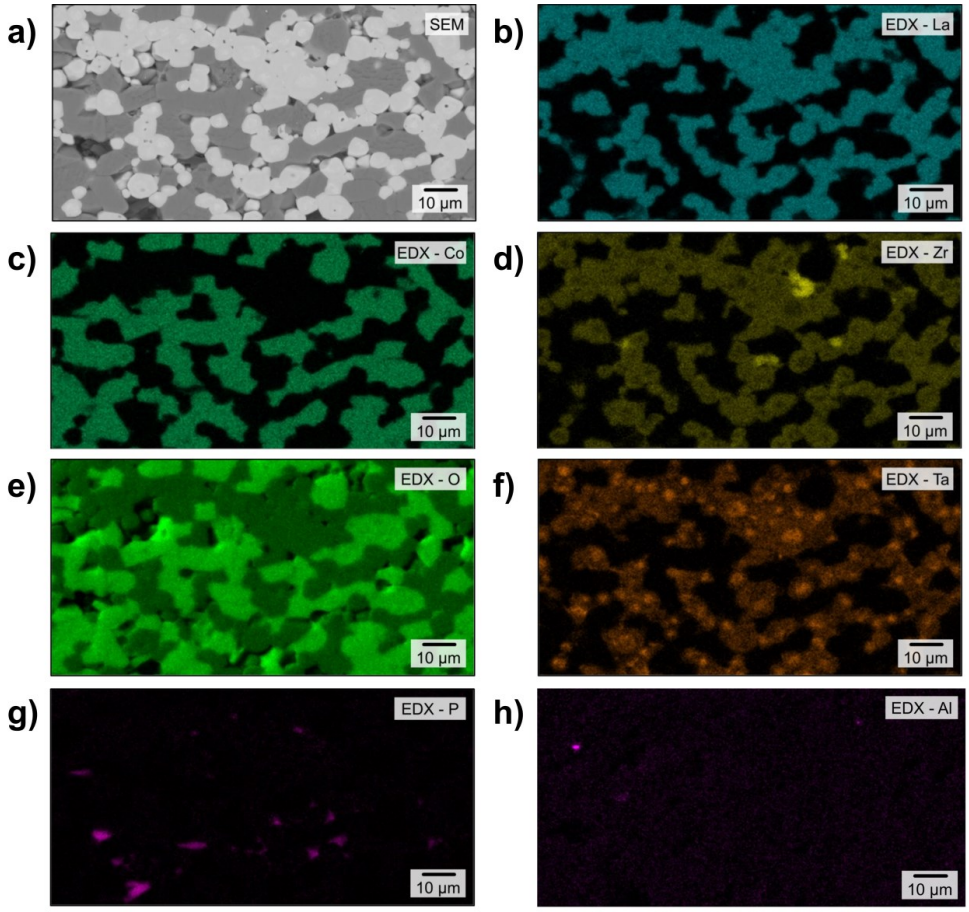

Figure 4.2.8: a) BSE-SEM image of the investigated area and the corresponding EDX results for the element distribution of **b)** La, **c)** Co, **d)** Zr, **e)** O, **f)** Ta, **g)** P, and **h)** Al, adapted from [218] is licensed under CC BY 4.0 (https://creativecommons.org/licenses/by/4.0/).

Therefore, EDX mapping and Raman measurements were performed at the exact same position in the tape. All measurements (except those with cross-sections) were taken on the LLZO-rich side as indicated by the XRD measurement. La, Zr and Ta elemental mappings match the bright LLZO spots in the image in **Figure 4.2.8 a**, while Co matches the dark spots of LCO. Interdiffusion between the two phases is not observed in the EDX mappings, although Ta has a somwhat inhomogeneous intensity distribution:

Ta is known to form Ta-rich rings inside the LLZO grains, although no answer is given in literature explaining the cause.[72,157,160,244,245] The Zr rich spots, leading to minimal traces of a secondary phase discernible in **Figure 4.2.8 a**, could also be related to this phenomenon as a consequence of the local shifts in stoichiometry by these Ta-rich rings given that Ta is located on the same lattice site as Zr. Else they may be caused by an imperfect stoichiometry weighing during the preparation of the precursors. The P traces that are detected in some areas result from a residue of the organic slurry mixture. The Al signal is too low to make a quantified assumption here.

In addition to the EDX measurement, Raman measurements are undertaken to confirm the results. Sometimes, as in the case of Al, secondary phases or intermediates are below the detection limit of EDX measurement, while Raman spectroscopy can still resolve them.[207]

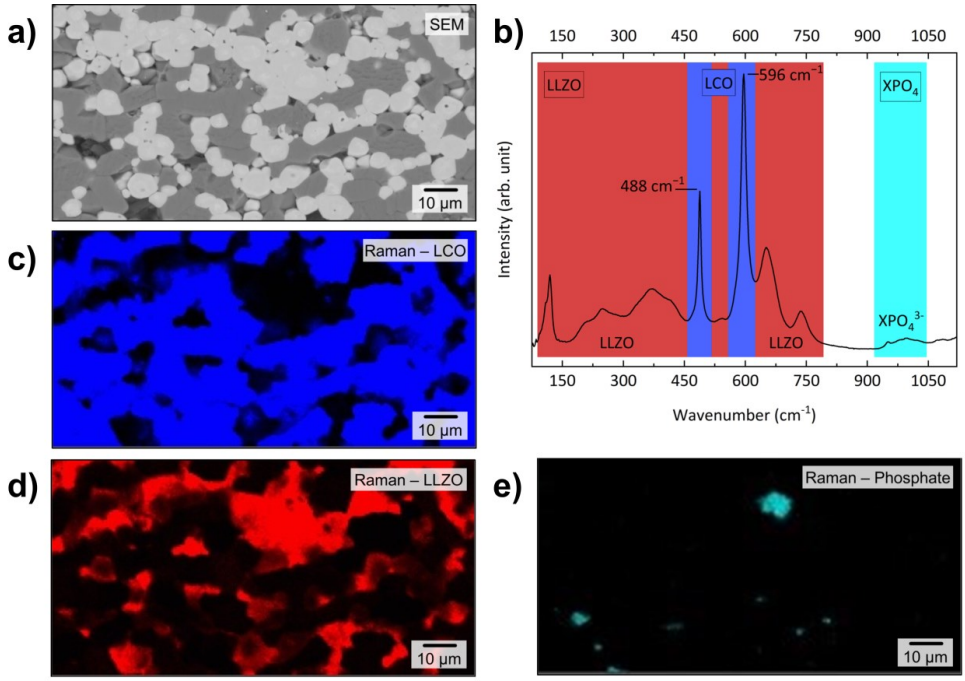

Figure 4.2.9: a) SEM image of the investigated area (equal to **Figure 4.2.8**), **b)** averaged Raman spectra with LLZO in red, LCO in blue, and a secondary signal of phosphate (XPO_4) in turquoise, and the corresponding Raman signal distribution of **c)** LCO, **d)** LLZO, and **e)** the secondary phase with phosphate (XPO_4), adapted from [218] is licensed under CC BY 4.0 (https://creativecommons.org/licenses/by/4.0/).

Figure 4.2.9 displays two main phases, LLZO (red) and LCO (blue), and an additional signal which may be the P residue visible in EDX. The small Zr secondary phase discernible in the EDX image in **Figure 4.2.8** is not visible in the Raman results, probably due to an overlap with LLZO signals. Focusing on the interdiffusion of the co-sintered composite cathode tape, only a secondary phase of the element P was observed in the EDX. This finding can be supported by Raman, as here at high wavenumbers a signal can be found that could belong to phosphate.[246,247] The two main phases, indicated in red and blue, belong to LLZO:Ta (space group $Ia\bar{3}d$) and rhombohedral LCO (space group R$\bar{3}$m),

respectively.[50,245,248–251] The LCO phase here has signals at 488 cm^{-1} (E_g) and 596 cm^{-1} (T_{2g}), which is remarkably close to the reference LCO wavenumber of 597 cm^{-1} [250,251]. As mentioned in 2.2.4, the most common interdiffusion known from literature are Al-ion diffusion from LLZO to LCO and Co-ion diffusion from LCO to LLZO. The diffusion of Al-ions into LCO leads to the formation of $LiAl_xCo_{1-x}O_2$ and normally results in a shift to higher wavenumbers.[161,250,251] Conversely, a shift in the opposite direction to lower wavenumbers would indicate a loss of Li.[252] The fact that a signal shift is not observed here means that either Al diffusion did not occur at all, or the wavelength impact of a potential Al diffusion is compensated exactly by the impact of the Li loss. Clearly, however, other signals from LLZO:Co (693 cm^{-1})[157,158,207] or $Li_{0.5}La_2Co_{0.5}O_4$ (685 cm^{-1})[207] cannot be found. These results contradict literature, where Co-ion interdiffusion is described as one of the major problems. Based on these new findings, ToF-SIMS measurements were performed to further verify the results of Raman and EDX.

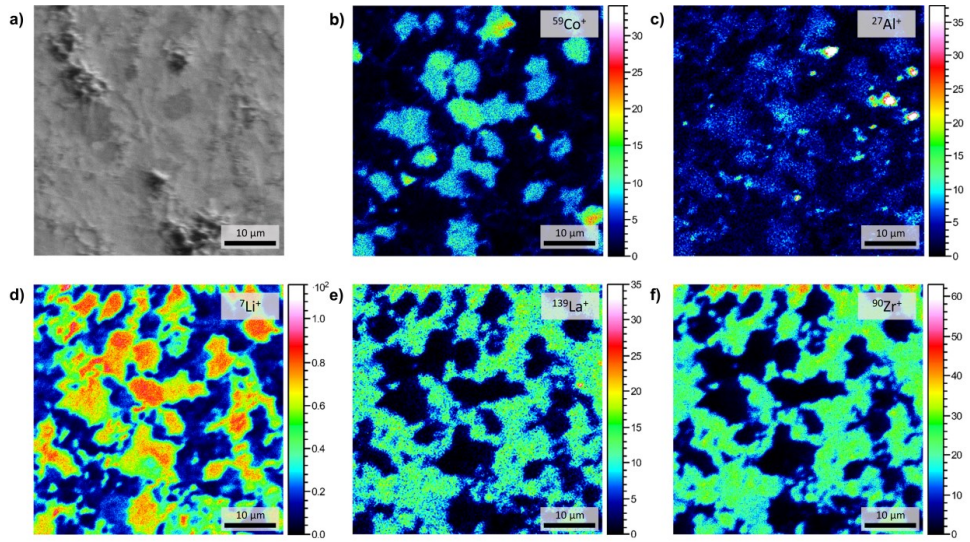

Figure 4.2.10: ToF-SIMS ion images and secondary electron image of the composite cathode tape (LLZO:LCO is 2:1). **a)** shows the microscope image, while **b)** Co, **c)** Al, **d)** Li, **e)** La, and **f)** Zr signals showing. The image scale is 50 µm × 50 µm, adapted from [218] is licensed under CC BY 4.0 (https://creativecommons.org/licenses/by/4.0/).

The analysis of the ToF-SIMS images clearly shows a match of La and Zr in the LLZO grains, while Co-ions are visible on the LCO grains only. Li is mainly visible in the LCO, because the Li concentration in LCO is higher than in LLZO, which directly corresponds to the intensities shown in the images. Contrary to EDX and Raman results, Al is found at the same location as LCO. This means that an Al-ion interdiffusion from LLZO to LCO took place during sintering, as is usually the case.[149,168] In addition this also means that the wavelength shift in the Raman measurements induced by the Al diffusion was indeed compensated exactly by the effect of a Li loss. The visible Al includes inhomogeneous, high-intensity spots, suggesting that the Al-ions are not well mixed during the milling. However, Co-ion interdiffusion into LLZO cannot be observed here, proving that indeed LLZO:Co is not formed, contrary

to the findings in literature. This proves that the *in-situ* synthesis so far is not only comparable to other synthesis methods, but even provides a higher purity in regard to suppressing the Co-ion interdiffusion.

Finally, electrochemical performance of the composite cathode tapes produced via the new *in-situ* route is measured in an All-Solid-State cells as described in chapter 3.1.4. The following parameters were used to calculate the capacity: a tape thickness of 85 µm, a cathode active material loading of 15 mg, and a tape diameter of 8.5 mm, resulting in a theoretical capacity of 2.1 mAh cm^{-2}.

The impedance is first measured at 60 °C before cycling the cell at the same temperature. The results are shown in a Nyquist plot in **Figure 4.2.11**. The solid-state cell was measured at higher temperature (60 °C) due to the low ionic conductivity of the polymer at room temperature.[253,254]

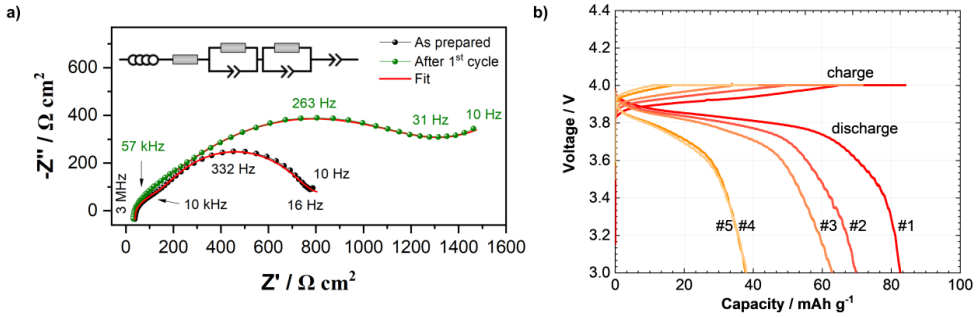

Figure 4.2.11: Electrochemical characterization of a Nyquist plot of the electrochemical impedance spectrum **a)** in a conventional liquid electrolyte-based cell at 30 µA cm^{-2} and **b)** in a solid-state cell at 35 µA cm^{-2} for five cycles for an ASB-cell, adapted from [218] is licensed under CC BY 4.0 (https://creativecommons.org/licenses/by/4.0/).

The analysis of the electrochemical cell performance in direct comparison of as-assembled state and after the first cycle allows to assess influences that occur during cycling. The Nyquist plot of the electrochemical impedance spectrum of the solid-state cell shows two semicircles, the first semicircle overlapping with the second one. The total resistance in the as-assembled state is less than 0.6 kΩ cm^2, which is much lower than comparable cell assemblies.[159] The fit values for each R-CPE element and the previous resistance are summarized in the table below:

Table 4-2: Values of the impedance fitting data for the solid-state cell as prepared and after its first cycle.

	as assembled	*1st cycle*
R1	25 Ω cm^2	23 Ω cm^2
R2	77 Ω cm^2	97 Ω cm^2
C2	10^{-8} F	10^{-7} F
R3	430 Ω cm^2	768 Ω cm^2
C3	10^{-7} F	10^{-7} F

Although a fitting of the semi-circles was performed it is difficult to determine, which resistance is attributed to the elements in the cell, due to the overlap of semi-circles. Therefore, only the total resistance should be considered. However, these values are still lower than previously reported values for composite cathodes of LCO-LLZO, prepared from different pre-synthesized LLZO powders using

different techniques.[103,149,154,158,159] It is hence possible that the suppression of the Co-ion interdiffusion and the *in-situ* formation of the LLZO particles lead to a cleaner grain boundary, resulting in a lower resistance. After the impedance measurement the cell was cycled between 3.0 and 4.0 V at a constant current density of 0.01 C (35 µA cm^{-2}) resulting in an initial discharge capacity of 82 mAh g^{-1} (59% of the theoretical capacity of LCO with 140 mAh g^{-2}). However, the cell reaches only a low initial discharge capacity. One reason for the low capacity could be the thickness of the composite cathode in combination with the ionic conductivity of the LLZO. Danner *et al.* assumed a theoretical limit of 50 µm thickness for this type of cathode morphology due to the limitations in the electron/ion transport.[48] The thickness of 85 µm in this study would explain the reduced capacity, especially without additional additive to increase the electronic conductivity, which is known to increase performance if homogeneously distributed.[255] The analysis also shows a high degradation immediately after the first cycle, not only in the impedance with an increase in the resistance attributed to the LCO-LLZO interface, but also in the discharge capacity (second cycle at 69 mAh g^{-1}). This is an expected result as it has been reported in literature that all-ceramic composite cathodes with LCO and LLZO show high degradation during cycling, making this effect one of the main focus areas in current research on All-Solid-State Batteries. A focused-ion-beam SEM image (FIB-SEM) (see **Figure 4.2.12**) shows cracks, indicated by arrows, already after the first few cycles, probably due to the volume change during intercalation/deintercalation.[140] These cracks lead to a contact loss (between LCO-LCO interfaces but also LCO-LLZO interfaces), resulting in capacity loss.[256,257]

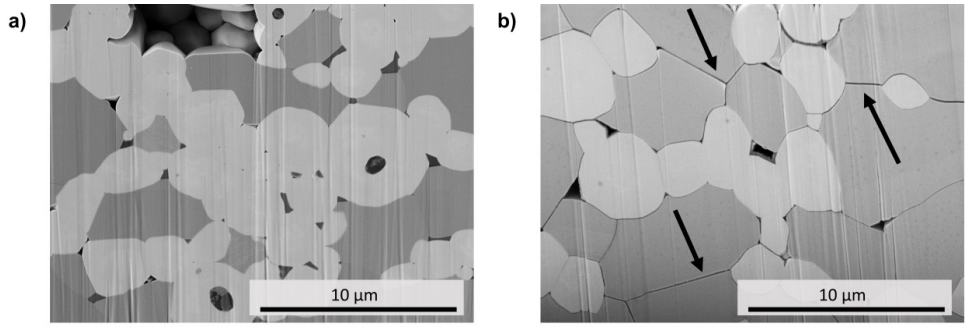

Figure 4.2.12: FIB-SEM micrographs were obtained using a Zeiss 1540 XB equipped with a Ga-ion source. Cross sections were milled using a beam current of 2 nA. The composite cathode tapes of **a)** before cycling and **b)** after 5 cycles are shown. Adapted from [218] is licensed under CC BY 4.0 (https://creativecommons.org/licenses/by/4.0/).

It can therefore be stated that the new *in-situ* synthesis route proved to be highly promising for composite cathode production. When testing it in a cell, its initial values ("as assembled") comply with the theoretical expectations and exceed reported values. Being an all-ceramic composite cathode, it still displays the typical shortcomings of capacity and resistance degradation when cycling in a cell. However, the resistance increase is lower than formerly observed.

Sub-section summary

The new *in-situ* process for the fabrication of composite cathodes was analyzed above and successfully demonstrated the *in-situ* synthesis of LLZO from precursors during a co-sintering step with LCO,

rendering the conventional heat-pretreatment steps obsolete. The resulting sintered tape obtained remarkably high densities and showed a successful suppression of Co-containing secondary phases[167,207,258] or Co-ion interdiffusion in LLZO[157,158,207], exceeding the results that are usually reported in literature. This resulted in a lower total resistance in a cell for an All-Solid-State battery, although the initial discharge capacity was lower than reported in the literature, reaching 59% of the theoretical capacity only.[157,158] The core problems of a high thickness versus low ionic conductivity of the solid electrolyte were discussed, as well as the formation of cracks at the LCO-LLZO interface, resulting in a high degradation and low discharge capacity in the cell. Whilst the first point will be addressed in the following chapters, the second provides opportunity for further research.

4.2.4 Variation of the $Li_7La_3Zr_2O_{12}$ dopants in composite cathodes

The composite cathodes produced by the new *in-situ* synthesis as demonstrated in the previous subchapter showed promising results compared to the conventional composite cathodes based on pre-synthesized LLZO. A central disadvantage of LLZO-LCO composite cathodes is the high degradation after a few cycles and the comparably low initial capacity of 59%. One of the reasons is the low ionic conductivity of LLZO in the composite cathode, which makes it impossible to use the active material over the full tape thickness.[48] The ionic conductivity will therefore be addressed in the following by adapting the LLZO dopants from Ta and Al to Ga. LLZO:Ga is reported to have a high ionic conductivity,[259] which would partially overcome the problems mentioned above.

Therefore, LiOH, La_2O_3, ZrO_2, and Ga_2O_5 precursors are used stoichiometrically to synthesize $Li_{6.4}La_3Zr_2Ga_{0.2}O_{12}$ with 5% of Li excess in the composite cathode. With the same procedure as described previously, the composite cathodes were tape cast and sintered at 1050 °C for 2 hours. The Li excess was reduced to 5% due to the side reaction of LLZO:Ga with higher Li excess.[61,260] As mentioned in chapter 2.2.3, LLZO:Ga is unstable to Li metal[260], the addition of SiO_2 particles, however, can stabilize LLZO:Ga by forming a glass phase.[61] This glass phase is formed by Li and SiO_2 and is located at the grain boundaries, allowing to insert Ga-ions more easily into the LLZO structure. This advantage is now assessed in the composite cathodes by comparing the sintered tapes of LLZO:Ga without additive, LLZO:Ga with additive and LLZO:Ta,Al without additive by XRD measurements.

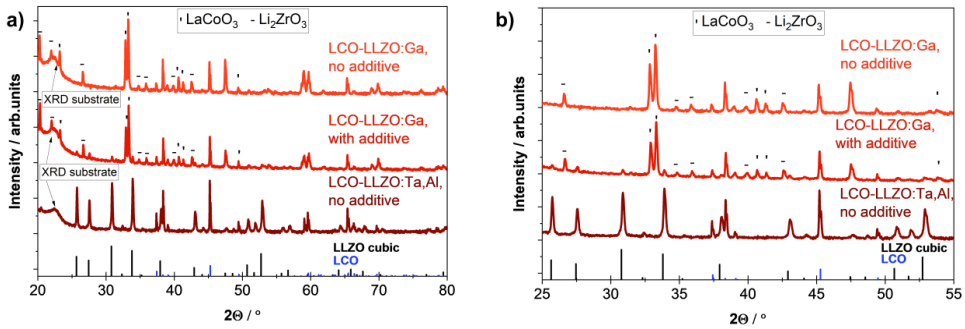

Figure 4.2.13: XRD pattern of composite cathode tapes of various dopants (Ga and Tal,Al) with and without additive with indication of side phases and the cubic LLZO structure (ICSD: 182312)[52] and LCO (ICSD: 29225) as references.

The analysis of the XRD measurement of the sintered tape with LLZO:Ta,Al has already been shown in the previous chapter: It showed the LCO phase next to a cubic LLZO phase. For LLZO:Ga, LCO phases are still visible in both cases, *i.e.* with and without additive. Here, the XRD measurements start at 20° 2Θ due to the high intensity of the LCO reflection at low angles. There are several other phases detected in the LLZO:Ga tape without additive, none of which, however, are consistent with the cubic LLZO structure. The existence of secondary phases such as $LaCoO_3$ and Li_2ZrO_3 suggests that LLZO is not formed during the sintering step. LLZO:Ga with additive (SiO_2 particles), however, shows a cubic LLZO phase, even if similar secondary phases as above can still be identified as well. This direct comparison reveals that the additive induces the formation of cubic LLZO from the precursors. Li *et al.* suggested that SiO_2 binds part of the Li to form a glass phase and subsequently Ga can be incorporated in the LLZO phase to form the cubic structure.[61] Given that the amount of Li needs to be reduced, it is assumed that without additive, the Li located in the LCO together with the Li excess leads to a large reservoir that prevents Ga incorporation and hence the formation of cubic LLZO. Due to the large amount of Li in the LCO, it is difficult to minimize the Li amount in the system. The different behavior between LLZO:Ta,Al and LLZO:Ga, both without additive, may be explained by the lattice sites that the respective dopants occupy: Ga is located on the Li site, and would therefore be replaced by an excess of Li. Al does occupy the Li site as well, however, it is typically present in much lower quantities. Ta on the other hand is located on the Zr site and is not affected by Li excess. Li excess therefore does affect LLZO:Ta,Al much less than LLZO:Ga, and the addition of SiO_2 particles reduces the excess Li sufficiently via the formation of a glass phase to stabilize the cubic structure.

4.2.5 *In-situ* synthesis route for $Li_7La_3Zr_2O_{12}$ separator

After having demonstrated the *in-situ* synthesis of LLZO of composite cathodes in the previous subchapter, a similar approach will now be employed to investigate the viability of using direct synthesis of LLZO precursors in separators.

The precursor powders with a stoichiometry of $Li_{6.6}La_3Zr_{1.6}Ta_{0.4}O_{12}$ and 10% Li excess was utilized in a slurry for tape-casting of a thin tape. The following XRD analysis assesses potential phase differences

comparing the green tape produced via precursors following the new *in-situ* synthesis route, and a conventional one based on pre-synthesized LLZO powder.

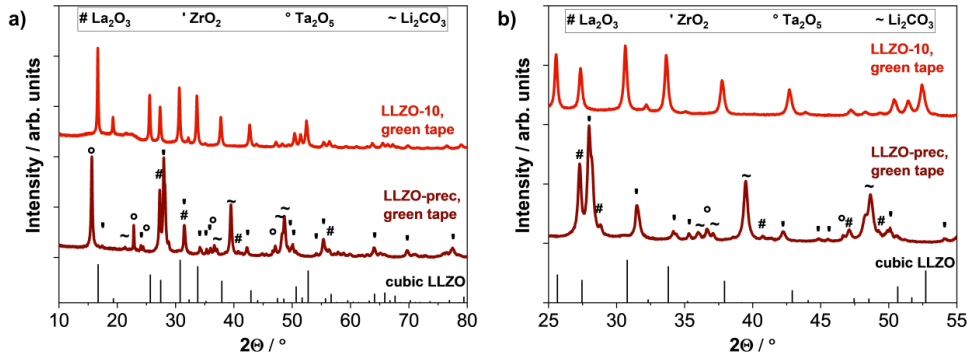

Figure 4.2.14: XRD patterns of LLZO-10 green tape and a precursor green tape. For analysis, the cubic LLZO reference (ICSD: 182312)[52] is given, while **a)** shows the total pattern, and **b)** is zoomed-in to show the impurity phase in a higher detail.

Other than in the green tape produced via the conventional process, the tape that is used for the new *in-situ* route does not contain pre-synthesized LLZO powder. The precursors, including LiOH, La_2O_3, ZrO_2, Al_2O_3, and Ta_2O_5, are expected to be present here in either their oxide or hydroxide form. Indeed, the reflections observed in the pattern in **Figure 4.2.14** can be attributed to the presence of LiOH, ZrO_2, and Ta_2O_5, while La_2O_3 has been identified as $La(OH)_3$, likely due to the influence of water impurities in the solvent during milling and in the solvent system within the slurry. The XRD result of the pre-synthesized LLZO green tape in **Figure 4.2.14** shows the expected cubic LLZO phase as it was already present in the powder.

The green tape produced above are then sintered with the optimized parameters (see **Figure 3.1.4**) at 1175 °C for 10 hours. As additional Al doping has led to abnormal grain growth, as previously documented, only LLZO:Ta was investigated in this experiment to mitigate the potential of the formation of liquid phases. The resulting sintered tapes are analyzed by XRD and are compared to LLZO-20 as-synthesized powder and the precursor green tape, as previously shown in chapter 4.2.2. The green tapes were synthesized in accordance to the scheme depicted in **Figure 4.2.1**.

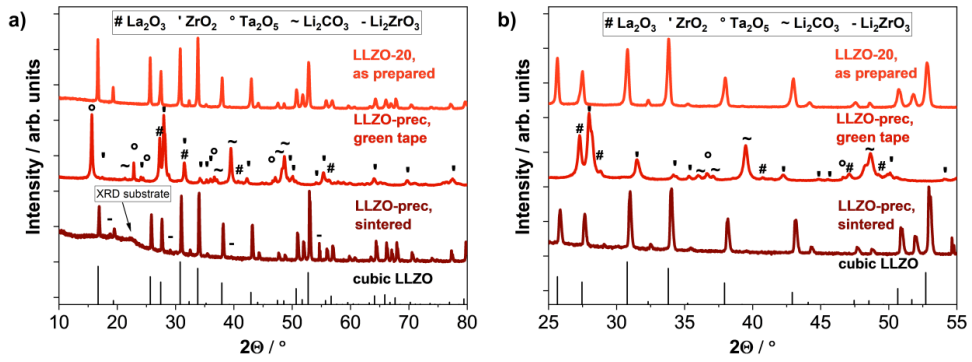

Figure 4.2.15: XRD patterns of LLZO-20 powder as prepared, and the LLZO green tape and sintered tape from precursor powder. For analysis, the cubic LLZO reference (ICSD: 182312)[52] is given, while **a)** shows the total pattern, and **b)** is zoomed-in to show the impurity phase in a higher detail.

The analysis of the XRD pattern indicates that some of the precursor phases remain in the sintered tape, either due to imprecise stoichiometry or to an incomplete formation of the LLZO phase. However, the pattern also clearly reveals the presence of a cubic LLZO structure as main phase in the sintered tape, which is not observed in the green tape. This successfully demonstrates that the precursors can form the cubic LLZO phase during sintering of the precursor green tape. Sintering occurs at higher temperatures and longer sintering times for the separator than for the solid electrolyte in composite cathodes, but cubic LLZO structure is still formed. To assess whether the additional requirements for a separator are met, the sintered tapes are analyzed microstructurally by SEM.

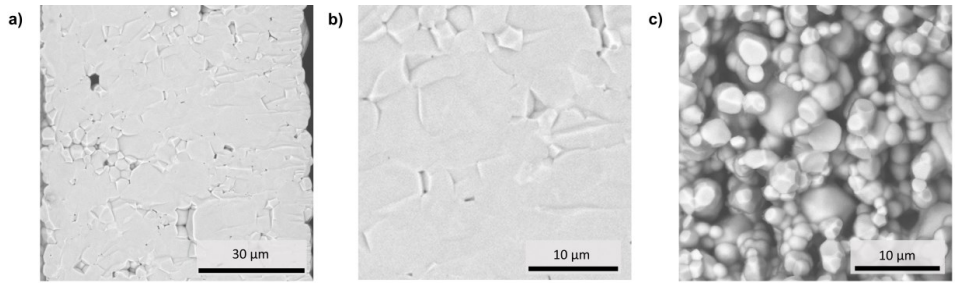

Figure 4.2.16: BSE-SEM images of a cross-section (fractured, un-polished) of LLZO:Ta, tapes sintered with from precursors powder at 1175 °C for 10 hours. **a)** shows a dense tape, **b)** zoom-in of the dense tape and **c)** shows a porous tape.

The BSE-SEM image depicts two tapes of vastly different density that were both obtained by the process above (**Figure 4.2.16 a-c**). The highly dense tape (theoretical density: 97%, **Figure 4.2.16 a+b**), exhibits intragranular fracture of the dense microstructure, while the highly porous tape (**Figure 4.2.16 c**) displays intergranular fracture of the porous microstructure. It should be noted that the high-density tape was achieved on a single occasion only. So far, the reproducible outcome is the low-density tape. The exact parameter causing the high density is still unknown. Numerous parameters were tested, indicating that the tape-casting process is influenced by factors that have yet to be identified or are beyond control. The high-density tape is presented here as a truly optimal sintering result and demonstrates that, by

understanding the tape-casting process and controlling all the parameters, highly dense tapes can actually be produced by this technique in the new *in-situ* synthesis route. Unfortunately, the tapes that were reproducible and obtained multiple times have a much lower density (relative density: <75%, by ImageJ analysis) which would be insufficient for dense separators. The grain sizes of the porous tapes are approximately 1 µm, with an isometric shape, which suggests that sintering barely occurred after the synthesis of LLZO, although temperatures of 1175 °C were used. Only a few grains show a good interface with neighboring grains, where they are in direct contact. One hypothesis for the low sintering activity of the grains is that the implementation of the LLZO synthesis into the green tape results in a decrease in density of the green tape. In addition to the organic material used in each green tape, the synthesis of LLZO releases more H_2O (25 wt%). This evaporation could lead to a low green tape density after the organic material is burnt, as the particles are too far apart for diffusion, preventing sintering. Another assumption is that the surface of the particles is modified by the *in-situ* formation of the LLZO. This is less likely though as the surface of the reacted particles should be pure LLZO, since it is formed only at high temperatures and impurities, such as carbonates should not exist to modify the surface.

The fact that the cubic structure was obtained for LLZO:Ta precursor tapes and yet the microstructure exhibits an insufficient density for use as a separator can be beneficial for another mixed cathode concept: The idea is to take advantage of the porous nature of the tape, for instance as a solid electrolyte scaffold and infiltrating the cathode active material. Due to the lower ionic conductivity of LLZO:Ta and the high ionic conductivity requirement for thick composite cathode design,[48] the doping was changed to LLZO:Ga for this experiment. LLZO:Ga is reported to have a high ionic conductivity due to a change of the cubic structure.[51] The precursors, with Ta_2O_5 replaced by Ga_2O_3, followed the stoichiometry $Li_{6.4}Ga_{0.2}La_3Zr_2O_{12}$ with 5% Li excess and were used to synthesize a tape similar to LLZO:Ta described above. The tape was sintered at 1175 °C for 10 hours, while the SiO_2 additive (0.1 wt%) discussed in section 4.2.4 was added to stabilize the LLZO:Ga against metallic Li, and to increase the density by adding an amorphous glass phase. The structure was analyzed by XRD and compared to as-synthesized LLZO:Ga powder as well as to LLZO-10 powder. The stoichiometry of the LLZO:Ga powder is $Li_{6.7}Ga_{0.1}La_3Zr_2O_{12}$, without Li excess.

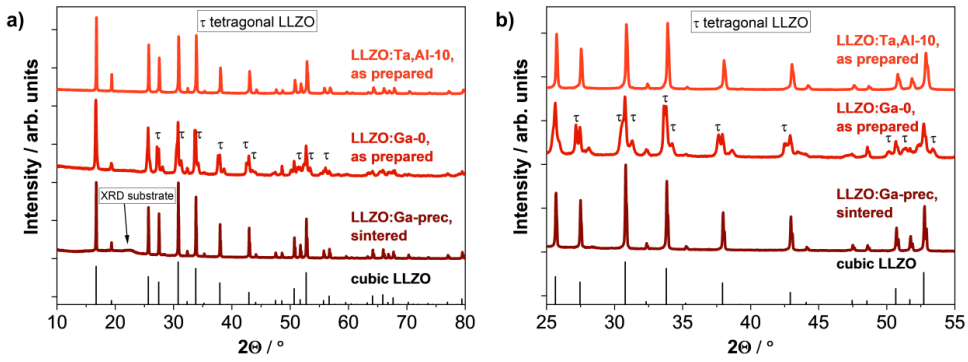

Figure 4.2.17: XRD patterns of LLZO-10 powder as prepared, LLZO:Ga powder as prepared, and a sintered tape of LLZO:Ga from precursor powder. For analysis, the cubic LLZO reference (ICSD: 182312)[52] is given, while **a)** shows the total pattern, and **b)** is zoomed-in to show the impurity phase in a higher detail.

The analysis of the XRD pattern of the sintered tapes produced from the precursor powder versus the LLZO-10 powder revealed a matching cubic LLZO phase, without any impurities. The LLZO:Ga powder, prepared by a solid-state reaction[261], exhibits a tetragonal LLZO phase in addition to the cubic LLZO phase. Due to its lower ionic conductivity, attempts are often made to suppress the tetragonal LLZO phase. Schwab *et al.* have highlighted the issues associated with LLZO:Ga with varying Li excess and its tendency to form the tetragonal LLZO phase with higher excess.[261] The XRD pattern exhibits a pure cubic LLZO structure, thus the sintered tapes were analyzed by SEM to investigate the sintering activity and the density.

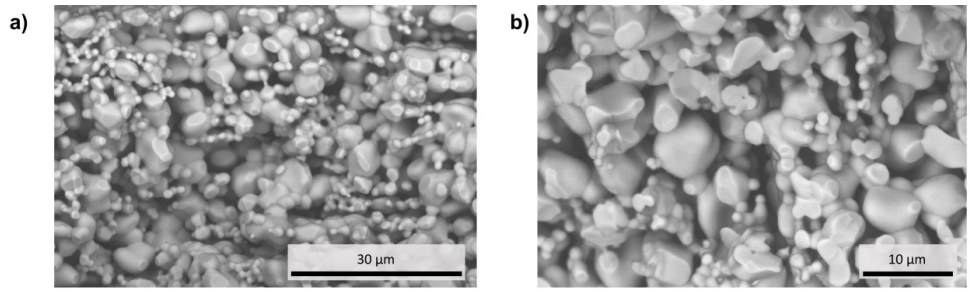

Figure 4.2.18: BSE-SEM images of a cross-section (fractured, un-polished) of sintered tapes of LLZO:Ga from precursor powder. **a)** shows a different area to **b)** shows a higher magnification.

BSE-SEM images demonstrate that the tapes sintered from LLZO:Ga precursor powder exhibit a porous structure comparable to that observed in the tapes sintered from LLZO:Ta precursor powder. The grain size distribution is inhomogeneous,. To overcome the sintering issue, which was not resolved by the SiO_2 glass phase, the strategy is to incorporate pre-synthesized LLZO particles into the green tape. This should trigger grain growth at the pre-synthesized particles acting as seeds, result in an increase in density, and provide the particles with a sufficiently dense green tape to enhance sintering activity. Consequently, pre-synthesized LLZO:Ga with a particle size > 2 µm was added to the slurry (without milling) prior to tape casting. The quantity of pre-synthesized LLZO:Ga particles (Ga-dopant 0.1, synthesized as stated elsewhere[261]) was set to 10 wt% and, 0.1 wt% of SiO_2 particles was also added. The slurry was then tape-cast according to the aforementioned process. The XRD results demonstrate that the Li excess was not sufficiently high, as proven by the presence of a secondary phase of $La_2Zr_2O_7$ in the tape (see **Figure 4.2.19**). The microstructure was then analyzed by SEM to clarify whether the incorporation of LLZO particles was able to enhance sintering activity.

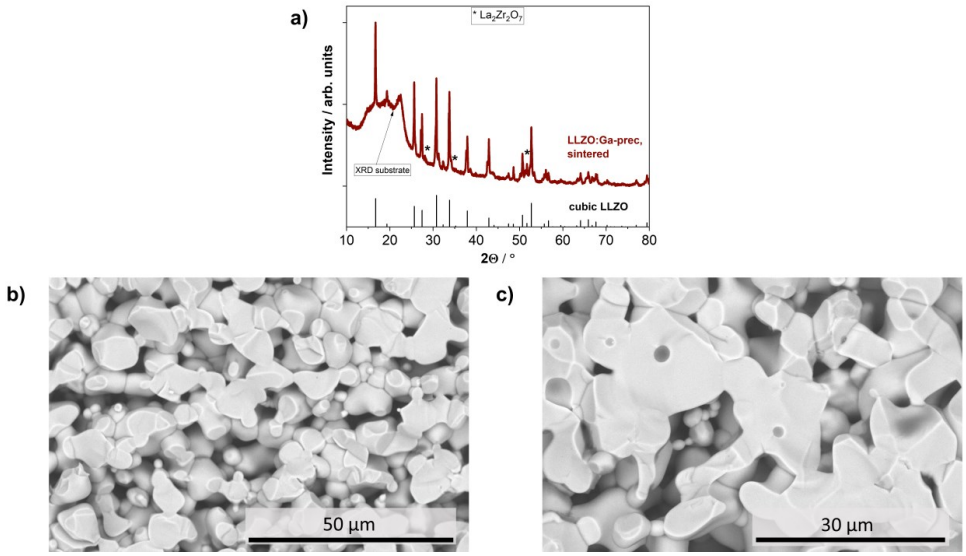

Figure 4.2.19: a) XRD patterns of sintered tape of LLZO:Ga from precursor powder with additionally pre-synthesized LLZO:Ga particles. For analysis, the cubic LLZO reference (ICSD: 182312)[52] is given. **b)** BSE-SEM images of a cross-section (fractured, un-polished) of sintered tapes of LLZO:Ga from precursor powder with additional pre-synthesized LLZO:Ga powder. **c)** shows a higher magnification image of a different area.

The analysis of the BSE-SEM images confirmed an increased sintering activity with larger grains than in the tape without additional LLZO:Ga pre-synthesized powder. Although the density of these tapes is low, the LLZO grains are well connected together, forming a porous but sintered LLZO structure. The increased density in the tape with the added LLZO grains compared to the tape without demonstrates that pre-synthesized LLZO particles can increase the density of the green tape, even if the optimal amount of LLZO particles required to achieve a highly dense structure has yet to be determined. This aligns well with the current trend in LLZO separator research to adopt porous-dense-porous structures. The goal would be to increase the surface area of the LLZO exposed to the active material in anode and cathodes by infiltrating the active materials into the LLZO framework. The above experiment now combines the novel *in-situ* process route to obtain a porous structure in LLZO:Ga, and shows that density can be further influenced. By optimizing the sintering additive, it may be possible to sinter a porous-dense-porous tape with LLZO:Ga in a single step, which should further be stable against Li metal anodes due to the SiO_2 additive. Other than in the new in-situ process for porous tapes, typically pore formers are used for sintering of porous tapes, such as Polymethylmethacrylat (PMMA).[262,263] The pore formers decompose during the sintering step, in case of PMMA already at 350 °C[262], leading to a porous structure with pore sizes related to the pore formers used. The new *in-situ* process allows to combine two advantages: On the one hand, it provides the opportunity to minimize the usage of additional chemicals, such as pore formers with a controlled pore volume, due to the varying addition of pre-synthesized LLZO particles, and on the other hand, it drastically reduces the time and energy requirement for the separator fabrication due to the direct *in-situ* route.

4.2.6 Recycled La_2O_3 as precursor material for $Li_7La_3Zr_2O_{12}$ separator synthesis

The novel process route is utilized with different precursors to form LLZO:Ta,Al. In the present subchapter, the combination of the direct *in-situ* process with recycled precursors shall be demonstrated. The used La_2O_3 precursor was derived from a LLZO recycling process in a hydrometallurgical approach. The LLZO powder was treated in sulfuric acid in a manner analogous to the process described by Schneider *et al.*[204] resulting in the formation of Li oxalate precipitate and subsequent calcination at 1000 °C[264]. Impurities of Al, Zr, and Ta were determined by ICP-OES, and their concentrations were considered in the calculation of the new synthesis batch with 20 % Li excess. The precursor amount was calculated after $Li_{6.45}Al_{0.05}La_3Zr_{1.6}Ta_{0.4}O_{12}$ stoichiometry. The tape-casting process was conducted as described earlier, with the addition of 10 wt% pre-synthesized LLZO-20 powder. Phase purity was checked by XRD.

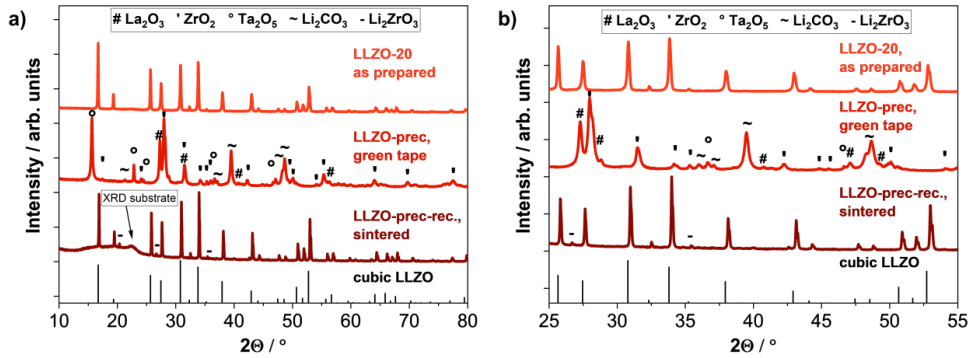

Figure 4.2.20: XRD patterns of LLZO-20 powder as prepared, LLZO green tape from precursor powder, and a sintered tape of LLZO from precursor powders with recycled La_2O_3. For analysis, the cubic LLZO reference (ICSD: 182312)[52] is given, while **a)** shows the total pattern, and **b)** is zoomed-in to show the impurity phase in a higher detail.

The analysis of the XRD pattern of the sintered tape with recycled La_2O_3 as a precursor confirms the expected presence of a cubic LLZO phase, accompanied by a single secondary phase. The high Li excess prevented the formation of the $La_2Zr_2O_7$ pyrochlore phase and instead a Li_2ZrO_3 phase was formed. This observation suggests that the LLZO stoichiometry was not met exactly, potentially due to the difficulty in obtaining ICP-OES results with a high reliability for LLZO powder. This would result in an insufficient La_2O_3 content, which would then lead to the formation of a secondary phase such as Li_2ZrO_3. This matter is related to the preceding ICP-OES assessment though, and not to the novel *in-situ* processing route. The tape was embedded and polished to investigate the presence of the secondary phase in the tape and to assess density and general grain size structure.

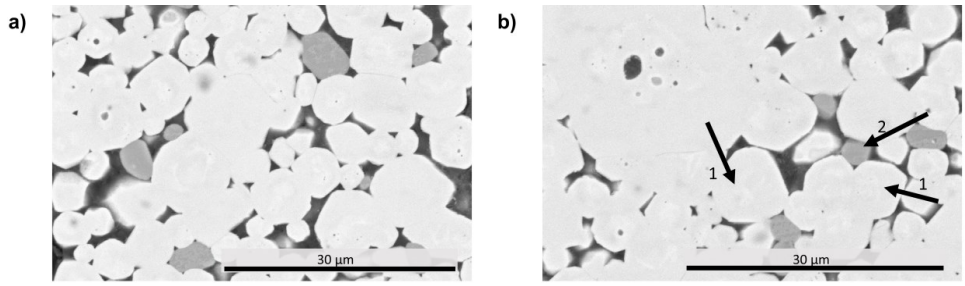

Figure 4.2.21: a) BSE-SEM images of a cross-section (embedded, polished) of sintered tapes of LLZO:Ta,Al from precursor powder with recycled La_2O_3. **b)** shows a higher magnification image of a different area.

The polished cross-sections in the BSE-SEM images show two distinct phases as expected based on the XRD results. The bright phase, which can be attributed to LLZO, exhibits additional Ta rings in the center of the LLZO grains. The Ta rings are indicated in **Figure 4.2.21 b** by arrows with the number 1. The Ta rings were previously observed in chapter 4.2.3, during the sintering of the composite cathodes. The LLZO grains are grown in a homogenous manner, with the tape reaching a relative density of 88% (by ImageJ, including the secondary phase). The relative density of the LLZO separator tapes is higher than that observed in previous studies of the *in-situ* process route. This phenomenon may correlate with the secondary phase or the impurities introduced into the process through the recycled La_2O_3. As demonstrated in chapter 4.2.5, the process is influenced by a parameter that is yet to be identified, which results in the formation of a high-density LLZO tape. The darker spots (arrow 2) can be attributed to the secondary phase, which is identified as Li_2ZrO_3 in the XRD pattern. Li_2ZrO_3 is a forming phase during the synthesis of LLZO and might have remained. It should be noted that even higher densities are required for a suitable dense separator. Due to the presence of the impurity phase, electrochemical testing was not conducted.

Section summary

A new *in-situ* synthesis route has been developed to improve an energy-efficient and cost-effective process for the synthesis of LLZO separator tapes and LCO-LLZO composite cathode tapes. The new process provides an opportunity to skip the costly and energy-intensive LLZO synthesis and particularly the heating steps, by using the precursors directly to form LLZO during the sintering of tapes themselves. LCO-LLZO composite cathodes doped with Ta and Al have been successfully fabricated by the new method. Here, the new tapes even go beyond the results reported in literature by suppressing Co-ion diffusion, which is highly disadvantageous during co-sintering of LCO and LLZO. Furthermore, separator tapes of LLZO:Ta and LLZO:Ga separator tapes have been fabricated successfully with LLZO cubic phases. Optimization could lead to a higher density in the tapes, the porosity that was found, however, allows to investigate the suitability of a porous-dense-porous LLZO tape for full cell assembly by infiltrating anode and cathode material into the LLZO framework. Finally, recycled La_2O_3 was used to form cubic LLZO, with a secondary phase in an 88% dense tape. This is the first time that recycled material has been successfully used to re-produce LLZO.

5 Conclusion and Outlook

All-Solid-State Batteries are seen as one of the most promising future battery technologies and are already entering the market. Among the various solid-state electrolytes, oxide-ceramic ion conductors are intensively researched, with LLZO garnet as the most promising material due to its stability against Li-metal. Nevertheless, industrial implementation of oxide ceramics still faces several challenges, mainly the high energy demand and production costs as well as the novel recycling strategies for oxide-ceramic based ASSBs. These challenges were addressed in the present work and shall be briefly summarized and concluded in the following.

From a recycling perspective, ceramics for solid-state batteries do not only hold a high embodied energy from the preceding synthesis steps but also contain several elements, which are on the list of critical raw materials. This makes them attractive for commercial recycling, but suitable recycling strategies need to be developed. In the present work, a direct recycling route of production waste material was successfully developed. The out-of-specification material, which cannot be used and is a high cost factor especially in early stage industry adaptation, was mimicked by using a degraded LLZO powder. A focus has been placed on malfunctions in synthesis of LLZO, which can lead to the Li-poor pyrochlore phase of $La_2Zr_2O_7$. It has been demonstrated successfully that LiOH and Li_2CO_3 are able to re-lithiate the degraded LLZO without additional process steps, allowing to incorporate the former reject material into the production process of a battery component. In the case of LiOH, the Li excess led to abnormal grain growth in the sintered tapes, independent of the step in which the additional Li was added. Abnormal grain growth started at a sintering time of 1 hour at 1175 °C, and at temperatures as low as 1025-1050 °C for 5 hours. The maximum grain size is independent of the temperature as long as formed, while it increases with increasing sintering time. Areas where no abnormal grain growth was observed, demonstrate increasing grain sizes over temperature with different growth rates. The reason for abnormal large grains was exhibited: Liquid phases, consisting of Li-Al-Mg-O and Li-Al-La-O formed at temperatures around 1050 °C. This observation led to the conclusion that without changing the doping in LLZO or reducing the Li excess, abnormal grain growth cannot easily be suppressed.

Due to the challenges of abnormal grain growth observed when using LiOH, the Li source was changed to Li_2CO_3 in lower quantities to assess the possibility of direct re-lithiation of real waste material. It was shown that LLZO powder waste and LLZO green tape waste both can be re-lithiated using the newly developed process to manufacture separator tapes. Particularly for separators from LLZO green tape waste, a case that is very close to industrial reality, the structure was re-lithiated completely from pyrochlore phase to pure cubic LLZO phase. Microstructural analyses exhibit tapes with <90% relative density, while ionic conductivity was comparable to LLZO separator tapes made from freshly synthesized LLZO powder. Critical current densities for the re-lithiated LLZO powder tapes did in fact exceed the values of freshly synthesized LLZO separator tapes. Even if further process parameter fine-tuning is recommended, the experiments clearly demonstrated for the first time that direct recycling is

possible for LLZO process waste material. This is a great step not only towards saving processing time, process complexity and raw materials, but also enables preservation of the energy embodied in the already synthesized ceramics.

The matter of high energy consumption and long processing times for LLZO component production, resulting in an elevated ecological footprint and high cost, were further addressed by the development of a direct, *in-situ* synthesis route. Typically, LLZO synthesis undergoes 2-3 calcination steps at temperatures of 900-1000 °C for 20 hours each, while sintering itself occurs at temperatures >1000 °C for 2-5 hours. It furthermore requires extensive preparatory steps, with the in-house milling taking 24 hours. The long processing times require large milling and oven capacities, hence inducing cost, and contribute significantly to the energy footprint in the case of heat treatment, further adding to the production cost. Within the scope of this work, the milling parameters were optimized such that a milling time of 15 minutes now suffices, reducing the milling time by nearly 99%. In addition, the novel *in-situ* process route uses the thermal activation during sintering to synthesize LLZO directly from precursors, which is possible for separator tapes as well as for composite cathodes with LCO. This means that all process steps that were formerly required to pre-synthesize LLZO can now be skipped, reducing the heat treatment steps from 2 x 20 hours + sintering (1 x 5 hours) to only sintering (1x 5 hours) in case for the separator. This results in a process time reduction of 80%, including temperatures >900 °C and hence also extremely decreasing the energy consumption. In the case of composite cathodes with a sintering time of only 2 hours, the process time reduction is as high as 85%.

During extensive testing and application of the new in-situ synthesis route, several known performance issues of LLZO separator tapes and composite cathodes were addressed. Most notably, the new route is able to successfully produce LCO-LLZO:Ta,Al composite cathodes while suppressing the Co-ion diffusion into LLZO, a widely reported and critical disadvantage in composite cathode fabrication, limiting theoretical capacities and resulting in a high degradation. Al-ion diffusion still needs to be addressed though. On the other hand, separators of LLZO:Ta and LLZO:Ga were successfully produced, demonstrating the cubic LLZO structure with the novel *in-situ* process. Here, a major challenge was the low density of the tapes, which is probably caused by the extra amount of water freed during reaction of the precursors, minimizing green tape density during the *in-situ* synthesis. Relative density can be tuned by adding a specific amount of pre-synthesized LLZO particles to the slurry, which is ideal for the fabrication of porous-dense-porous tapes that can be used for *e.g.* infiltrating anode or cathode active materials. Finally, it was also shown that recycled La_2O_3 from LLZO waste, obtained by a project partner via a hydrometallurgical approach, can be re-used in the novel *in-situ* process. Even if the resulting micro-structure of the tapes made from recycled material still requires further process optimization, the results represent a huge step towards an energy- and cost-efficient recycling procedure for oxide ceramic battery components based on LLZO.

In conclusion, the recycling of ceramic All-Solid-State Batteries on a material and component level have been successfully adapted and demonstrated. The application of a direct recycling route on LLZO production process waste material emerged as a highly promising approach to minimize both re-synthesis and overall recycling cost. Furthermore, the LLZO synthesis and component production process was optimized to such a degree that in total 65% of the process time could be saved, in single

steps even over 98% and during heat treatments 80-85%. This goes along with massive energy savings, resulting in an improved ecological footprint and great cost advantages, further supported by the massive reduction in oven and plant capacity and related investments.

Based on these insights, the following future research directions were identified to give the most benefit for fast ASSB performance improvement and industrial implementation:

- Application of the novel *in-situ* process route to optimize porous-dense-porous LLZO frameworks, which can be easily obtained by optimizing the amount of pre-synthesized particles in the slurry. This LLZO framework would open possibilities for cathode active material infiltration without an addition of pore fillers, resulting in a more simple process for battery component fabrication.
- Co-sintering of composite cathodes with separators to minimize process time even further by only a single sintering step. It was already shown that Co-ion diffusion into LLZO next to LCO in the composite cathode is suppressed by the novel *in-situ* process route. If this can be combined with co-sintering of a dense separator LLZO layer, it would result in a half-cell by conventional sintering in a single-heating step only, thanks to the *in-situ* synthesis of LLZO.
- Developing a direct recycling route for composite cathode active material to minimize cost due to embodied energy should also be investigated. The direct recycling possibility shown here for LLZO powder waste and LLZO green tape waste gives an idea of how to implement these into the composite cathode green tape waste.
- It should be also investigated to which extent impurities in the recycled material affect the LLZO synthesis. These insights will help with direct recycling of a full battery stack, which might be an attractive option for industry instead of separating ceramic materials for direct recycling.
- Possibilities of a full battery cell or even a battery stack recycling should be addressed. These may include completely different approaches comprising disassembling or mechanical shredding. A special focus should be placed on the recycling of the Li metal as one of the major challenges compared to liquid electrolyte batteries.

The foundation for LLZO-based battery component recycling, especially direct recycling, has been laid in this thesis. All of the research topics suggested above could now open up new possibilities in the development of ceramic battery components and recycling approaches, which have to be implemented by industry by EU Directive. Furthermore, optimization and development of the novel synthesis process would pave the way to industrial implementation, saving significant amounts of time, energy and cost, ultimately contributing to the overarching goal of an ecofriendly and affordable energy transition.

6 References

1. United Nations. Paris Agreement, 2015.

2. IEA, International Energy Agency. Global EV Outlook 2024 (2024).

3. IEA, International Energy Agency. Batteries and Secure Energy Transitions. *World Energy Outlook Special Report* (2024).

4. Janek, J. & Zeier, W. G. A solid future for battery development. *Nature Energy* **1**; 10.1038/nenergy.2016.141 (2016).

5. European Comission. Critical Raw Materials Resilience: Charting a Path towards greater Security and Sustainability, 2020.

6. *Regulation (EU) 2023/1542 of the European Parliament and of the Council of 12 July 2023 concerning batteries and waste batteries, amending Directive 2008/98/EC and Regulation (EU) 2019/1020 and repealing Directive 2006/66/EC (1)* (2023).

7. Diekmann, J. & Kwade, A. (eds.). *Recycling of Lithium-Ion Batteries. The LithoRec Way.* 1st ed. (Springer International Publishing; Imprint: Springer, Cham, 2018).

8. Kononova, N., Blömeke, S., Cerdas, F., Zellmer, S. & Herrmann, C. Identification of target materials for recycling of solid-state batteries from environmental and economic perspective using information theory entropy. *Procedia CIRP* **116,** 185–190; 10.1016/j.procir.2023.02.032 (2023).

9. Kiyek, V., Hilger, M., Rosen, M., Gross, J. P., Mann, M., Fattakhova-Rohlfing, D., Schwaiger, R., Finsterbusch, M. & Guillon, O. Waste minimization in all-solid-state battery production via re-lithiation of the garnet solid electrolyte LLZO. *Journal of Power Sources* **609,** 234709; 10.1016/j.jpowsour.2024.234709 (2024).

10. Xu, P., Dai, Q., Gao, H., Liu, H., Zhang, M., Li, M., Chen, Y., An, K., Meng, Y. S., Liu, P., Li, Y., Spangenberger, J. S., Gaines, L., Lu, J. & Chen, Z. Efficient Direct Recycling of Lithium-Ion Battery Cathodes by Targeted Healing. *Joule* **4,** 2609–2626; 10.1016/j.joule.2020.10.008 (2020).

11. Sloop, S., Crandon, L., Allen, M., Koetje, K., Reed, L., Gaines, L., Sirisaksoontorn, W. & Lerner, M. A direct recycling case study from a lithium-ion battery recall. *Sustainable Materials and Technologies* **25,** e00152; 10.1016/j.susmat.2020.e00152 (2020).

12. Wissel, K., Haben, A., Küster, K., Starke, U., Kautenburger, R., Ensinger, W. & Clemens, O. Direct Recycling of β-Li 3PS4 - Based All-Solid-State Li-Ion Batteries: Interactions of Electrode

Materials and Electrolyte in a Dissolution-Based Separation Process. *Advanced Energy and Sustainability Research*; 10.1002/aesr.202300280 (2024).

13. Armand, M. & Tarascon, J.-M. Building better batteries. *Nature* **451,** 652–657; 10.1038/451652a (2008).

14. IEA - International Energy Agency. Global EV Outlook 2023: Catching up with climate ambitions.

15. Kurzweil, P. *Angewandte Elektrochemie. Grundlagen, Messtechnik, Elektroanalytik, Energiewandlung, technische Verfahren* (Springer Vieweg, Wiesbaden, Heidelberg, 2020).

16. Hamann, C. H. & Vielstich, W. *Elektrochemie.* 4th ed. (Wiley-VCH, Weinheim, 2005).

17. Goodenough, J. B. & Park, K.-S. The Li-ion rechargeable battery: a perspective. *Journal of the American Chemical Society* **135,** 1167–1176; 10.1021/ja3091438 (2013).

18. Tarascon, J. M. & Armand, M. Issues and challenges facing rechargeable lithium batteries. *Nature* **414,** 359–367; 10.1038/35104644 (2001).

19. Logan, E. R. & Dahn, J. R. Electrolyte Design for Fast-Charging Li-Ion Batteries. *Trends in Chemistry* **2,** 354–366; 10.1016/j.trechm.2020.01.011 (2020).

20. Janek, J. & Adelhelm, P. Zukunftstechnologien. In *Handbuch Lithium-Ionen-Batterien,* edited by R. Korthauer (Springer Berlin Heidelberg, Berlin, Heidelberg, 2013), pp. 199–217.

21. Selinis, P. & Farmakis, F. Review—A Review on the Anode and Cathode Materials for Lithium-Ion Batteries with Improved Subzero Temperature Performance. *Journal of The Electrochemical Society* **169,** 10526; 10.1149/1945-7111/ac49cc (2022).

22. Chan, C. K., Peng, H., Liu, G., McIlwrath, K., Zhang, X. F., Huggins, R. A. & Cui, Y. High-performance lithium battery anodes using silicon nanowires. *Nature nanotechnology* **3,** 31–35; 10.1038/nnano.2007.411 (2008).

23. Wilson, A. M., Zank, G., Eguchi, K., Xing, W. & Dahn, J. R. Pyrolysed silicon-containing polymers as high capacity anodes for lithium-ion batteries. *Journal of Power Sources* **68,** 195–200; 10.1016/S0378-7753(96)02551-7 (1997).

24. Zhu, J., Ng, K. Y. S. & Da Deng. Hollow cocoon-like hematite mesoparticles of nanoparticle aggregates: structural evolution and superior performances in lithium ion batteries. *ACS Applied Materials & Interfaces* **6,** 2996–3001; 10.1021/am4055996 (2014).

25. Da Deng & Lee, J. Y. Meso-oblate spheroids of thermal-stabile linker-free aggregates with size-tunable subunits for reversible lithium storage. *ACS Applied Materials & Interfaces* **6,** 1173–1179; 10.1021/am404853n (2014).

26. Da Deng. Li-ion batteries: basics, progress, and challenges. *Energy Science & Engineering* **3,** 385–418; 10.1002/ese3.95 (2015).

27. Liu, B., Zhang, J.-G. & Xu, W. Advancing Lithium Metal Batteries. *Joule* **2,** 833–845; 10.1016/j.joule.2018.03.008 (2018).

28. Elias Holdenried. Hoffnungstechnologie Feststoffbatterie: Wann kommt die E-Auto-Revolution endlich in Serie? *Buisness Insider* **2021** (06:58, 2021).

29. Krauskopf, T., Mogwitz, B., Hartmann, H., Singh, D. K., Zeier, W. G. & Janek, J. The Fast Charge Transfer Kinetics of the Lithium Metal Anode on the Garnet-Type Solid Electrolyte Li6.25Al0.25La3Zr2O12. *Advanced Energy Materials* **10,** 2000945; 10.1002/aenm.202000945 (2020).

30. Betz, J., Bieker, G., Meister, P., Placke, T., Winter, M. & Schmuch, R. Theoretical versus Practical Energy: A Plea for More Transparency in the Energy Calculation of Different Rechargeable Battery Systems. *Advanced Energy Materials* **9,** 1803170; 10.1002/aenm.201803170 (2019).

31. Randau, S., Weber, D. A., Kötz, O., Koerver, R., Braun, P., Weber, A., Ivers-Tiffée, E., Adermann, T., Kulisch, J., Zeier, W. G., Richter, F. H. & Janek, J. Benchmarking the performance of all-solid-state lithium batteries. *Nature Energy* **5,** 259–270; 10.1038/s41560-020-0565-1 (2020).

32. Schwich, L., Küpers, M., Finsterbusch, M., Schreiber, A., Fattakhova-Rohlfing, D., Guillon, O. & Friedrich, B. Recycling Strategies for Ceramic All-Solid-State Batteries—Part I: Study on Possible Treatments in Contrast to Li-Ion Battery Recycling. *Metals* **10,** 1523; 10.3390/met10111523 (2020).

33. Yang, C., Fu, K., Zhang, Y., Hitz, E. & Hu, L. Protected Lithium-Metal Anodes in Batteries: From Liquid to Solid. *Advanced Materials* **29**; 10.1002/adma.201701169 (2017).

34. Monroe, C. & Newman, J. The Effect of Interfacial Deformation on Electrodeposition Kinetics. *Journal of The Electrochemical Society* **151,** A880; 10.1149/1.1710893 (2004).

35. Monroe, C. & Newman, J. The Impact of Elastic Deformation on Deposition Kinetics at Lithium/Polymer Interfaces. *Journal of The Electrochemical Society* **152,** A396; 10.1149/1.1850854 (2005).

36. Kim, M., Seo, J., Suba, J. P. D. & Cho, K. Y. A review of polymers in sulfide-based hybrid solid-state electrolytes for all-solid-state lithium batteries. *Materials Chemistry Frontiers* **7,** 5475–5499; 10.1039/D3QM00729D (2023).

37. Liu, Q., Geng, Z., Han, C., Fu, Y., Li, S., He, Y.-B., Kang, F. & Li, B. Challenges and perspectives of garnet solid electrolytes for all solid-state lithium batteries. *Journal of Power Sources* **389,** 120–134; 10.1016/j.jpowsour.2018.04.019 (2018).

38. Lu, W., Xue, M. & Zhang, C. Modified Li7La3Zr2O12 (LLZO) and LLZO-polymer composites for solid-state lithium batteries. *Energy Storage Materials* **39,** 108–129; 10.1016/j.ensm.2021.04.016 (2021).

39. Zhu, Y., Gonzalez-Rosillo, J. C., Balaish, M., Hood, Z. D., Kim, K. J. & Rupp, J. L. M. Lithium-film ceramics for solid-state lithionic devices. *Nature Reviews Materials* **6,** 313–331; 10.1038/s41578-020-00261-0 (2021).

40. Hou, M., Liang, F., Chen, K., Dai, Y. & Xue, D. Challenges and perspectives of NASICON-type solid electrolytes for all-solid-state lithium batteries. *Nanotechnology* **31,** 132003; 10.1088/1361-6528/ab5be7 (2020).

41. Stramare, S., Thangadurai, V. & Weppner, W. Lithium Lanthanum Titanates: A Review. *Chemistry of Materials* **15,** 3974–3990; 10.1021/cm0300516 (2003).

42. Deng, Z., Ni, D., Chen, D., Bian, Y., Li, S., Wang, Z. & Zhao, Y. Anti-perovskite materials for energy storage batteries. *InfoMat* **4**; 10.1002/inf2.12252 (2022).

43. Kamaya, N., Homma, K., Yamakawa, Y., Hirayama, M., Kanno, R., Yonemura, M., Kamiyama, T., Kato, Y., Hama, S., Kawamoto, K. & Mitsui, A. A lithium superionic conductor. *Nature materials* **10,** 682–686; 10.1038/nmat3066 (2011).

44. Suci, W. G., Aliwarga, H. K., Azinuddin, Y. R., Setyawati, R. B., Stulasti, K. N. R. & Purwanto, A. Review of various sulfide electrolyte types for solid-state lithium-ion batteries. *Open Engineering* **12,** 409–423; 10.1515/eng-2022-0043 (2022).

45. Wu, J., Liu, S., Han, F., Yao, X. & Wang, C. Lithium/Sulfide All-Solid-State Batteries using Sulfide Electrolytes. *Advanced materials (Deerfield Beach, Fla.)* **33,** e2000751; 10.1002/adma.202000751 (2021).

46. Kotobuki, M., Kanamura, K., Sato, Y. & Yoshida, T. Fabrication of all-solid-state lithium battery with lithium metal anode using Al2O3-added Li7La3Zr2O12 solid electrolyte. *Journal of Power Sources* **196,** 7750–7754; 10.1016/j.jpowsour.2011.04.047 (2011).

47. Doose, S., Mayer, J. K., Michalowski, P. & Kwade, A. Challenges in Ecofriendly Battery Recycling and Closed Material Cycles: A Perspective on Future Lithium Battery Generations. *Metals* **11,** 291; 10.3390/met11020291 (2021).

48. Finsterbusch, M., Danner, T., Tsai, C.-L., Uhlenbruck, S., Latz, A. & Guillon, O. High Capacity Garnet-Based All-Solid-State Lithium Batteries: Fabrication and 3D-Microstructure Resolved Modeling. *ACS applied materials & interfaces* **10,** 22329–22339; 10.1021/acsami.8b06705 (2018).

49. Murugan, R., Thangadurai, V. & Weppner, W. Schnelle Lithiumionenleitung in granatartigem Li7La3Zr2O12. *Angewandte Chemie* **119,** 7925–7928; 10.1002/ange.200701144 (2007).

50. Larraz, G., Orera, A. & Sanjuán, M. L. Cubic phases of garnet-type Li7La3Zr2O12: the role of hydration. *Journal of Materials Chemistry A* **1,** 11419; 10.1039/c3ta11996c (2013).

51. Wagner, R., Redhammer, G. J., Rettenwander, D., Senyshyn, A., Schmidt, W., Wilkening, M. & Amthauer, G. Crystal Structure of Garnet-Related Li-Ion Conductor Li7-3xGaxLa3Zr2O12: Fast Li-Ion Conduction Caused by a Different Cubic Modification? *Chemistry of Materials* **28,** 1861–1871; 10.1021/acs.chemmater.6b00038 (2016).

52. Awaka, J., Takashima, A., Kataoka, K., Kijima, N., Idemoto, Y. & Akimoto, J. Crystal Structure of Fast Lithium-ion-conducting Cubic Li7La3Zr2O12. *Chemistry Letters* **40,** 60–62; 10.1246/cl.2011.60 (2011).

53. van Wüllen, L., Echelmeyer, T., Meyer, H.-W. & Wilmer, D. The mechanism of Li-ion transport in the garnet Li5La3Nb2O12. *Physical chemistry chemical physics : PCCP* **9,** 3298–3303; 10.1039/B703179C (2007).

54. Thangadurai, V., Pinzaru, D., Narayanan, S. & Baral, A. K. Fast Solid-State Li Ion Conducting Garnet-Type Structure Metal Oxides for Energy Storage. *The journal of physical chemistry letters* **6,** 292–299; 10.1021/jz501828v (2015).

55. Baek, S.-W., Lee, J.-M., Kim, T. Y., Song, M.-S. & Park, Y. Garnet related lithium ion conductor processed by spark plasma sintering for all solid state batteries. *Journal of Power Sources* **249,** 197–206; 10.1016/j.jpowsour.2013.10.089 (2014).

56. Nagata, H. & Akimoto, J. Ionic Conductivity of Low-Crystalline Li4P2S6 and Li4P2S6–LiX (X=Cl, Br, and I) Systems and Their Role in Improved Positive Electrode Performance in All-Solid-State LiS Battery. *ChemistrySelect* **5,** 9926–9931; 10.1002/slct.202002308 (2020).

57. Awaka, J., Kijima, N., Hayakawa, H. & Akimoto, J. Synthesis and structure analysis of tetragonal Li7La3Zr2O12 with the garnet-related type structure. *Journal of Solid State Chemistry* **182,** 2046–2052; 10.1016/j.jssc.2009.05.020 (2009).

58. Bernstein, N., Johannes, M. D. & Hoang, K. Origin of the structural phase transition in Li7La3Zr2O12. *Physical review letters* **109,** 205702; 10.1103/PhysRevLett.109.205702 (2012).

59. Geiger, C. A., Alekseev, E., Lazic, B., Fisch, M., Armbruster, T., Langner, R., Fechtelkord, M., Kim, N., Pettke, T. & Weppner, W. Crystal chemistry and stability of "Li7La3Zr2O12" garnet: a fast lithium-ion conductor. *Inorganic chemistry* **50,** 1089–1097; 10.1021/ic101914e (2011).

60. Jin, Y. & McGinn, P. J. Al-doped Li7La3Zr2O12 synthesized by a polymerized complex method. *Journal of Power Sources* **196,** 8683–8687; 10.1016/j.jpowsour.2011.05.065 (2011).

61. Li, J., Luo, H., Liu, K., Zhang, J., Zhai, H., Su, X., Wu, J., Tang, X. & Tan, G. Excellent Stability of Ga-Doped Garnet Electrolyte against Li Metal Anode via Eliminating LiGaO2 Precipitates for

Advanced All-Solid-State Batteries. *ACS applied materials & interfaces* **15,** 7165–7174; 10.1021/acsami.2c21603 (2023).

62. Qin, S., Zhu, X., Jiang, Y., Ling, M., Hu, Z. & Zhu, J. Growth of self-textured Ga3+ -substituted Li7La3Zr2O12 ceramics by solid state reaction and their significant enhancement in ionic conductivity. *Applied Physics Letters* **112,** 113901; 10.1063/1.5019179 (2018).

63. El Shinawi, H. & Janek, J. Stabilization of cubic lithium-stuffed garnets of the type "Li7La3Zr2O12" by addition of gallium. *Journal of Power Sources* **225,** 13–19; 10.1016/j.jpowsour.2012.09.111 (2013).

64. Wolfenstine, J., Ratchford, J., Rangasamy, E., Sakamoto, J. & Allen, J. L. Synthesis and high Li-ion conductivity of Ga-stabilized cubic Li7La3Zr2O12. *Materials Chemistry and Physics* **134,** 571–575; 10.1016/j.matchemphys.2012.03.054 (2012).

65. Wu, J.-F., Chen, E.-Y., Yu, Y., Liu, L., Wu, Y., Pang, W. K., Peterson, V. K. & Guo, X. Gallium-Doped Li7La3Zr2O12 Garnet-Type Electrolytes with High Lithium-Ion Conductivity. *ACS Applied Materials & Interfaces* **9,** 1542–1552; 10.1021/acsami.6b13902 (2017).

66. Rettenwander, D., Wagner, R., Reyer, A., Bonta, M., Cheng, L., Doeff, M. M., Limbeck, A., Wilkening, M. & Amthauer, G. Interface Instability of Fe-Stabilized Li7La3Zr2O12 versus Li Metal. *The Journal of Physical Chemistry C* **122,** 3780–3785; 10.1021/acs.jpcc.7b12387 (2018).

67. Cao, W., Zhang, J. & Li, H. Batteries with high theoretical energy densities. *Energy Storage Materials* **26,** 46–55; 10.1016/j.ensm.2019.12.024 (2020).

68. Liu, M., Li, B., Zhang, S., Xie, W., Li, G., Wang, Y., Wen, Y., Qiu, J., Chen, J. & Zhao, P. Effect of Nb and Ta Simultaneous Substitution on Self-Consolidation Sintering of Li7La3Zr2O12. *ACS Applied Energy Materials* **5,** 7559–7570; 10.1021/acsaem.2c01018 (2022).

69. Buannic, L., Orayech, B., Del López Amo, J.-M., Carrasco, J., Katcho, N. A., Aguesse, F., Manalastas, W., Zhang, W., Kilner, J. & Llordés, A. Dual Substitution Strategy to Enhance Li + Ionic Conductivity in Li7La3Zr2O12 Solid Electrolyte. *Chemistry of Materials* **29,** 1769–1778; 10.1021/acs.chemmater.6b05369 (2017).

70. Abrha, L. H., Hagos, T. T., Nikodimos, Y., Bezabh, H. K., Berhe, G. B., Hagos, T. M., Huang, C.-J., Tegegne, W. A., Jiang, S.-K., Weldeyohannes, H. H., Wu, S.-H., Su, W.-N. & Hwang, B. J. Dual-Doped Cubic Garnet Solid Electrolytes with Superior Air Stability. *ACS Applied Materials & Interfaces* **12,** 25709–25717; 10.1021/acsami.0c01289 (2020).

71. Smart, L. E. & Moore, E. A. *Solid State Chemistry. An Introduction, Fourth Edition.* 4th ed. (CRC Press, 2012).

72. Mann, M., Küpers, M., Häuschen, G., Finsterbusch, M., Fattakhova-Rohlfing, D. & Guillon, O. Evaluation of Scalable Synthesis Methods for Aluminum-Substituted Li7La3Zr2O12 Solid Electrolytes. *Materials (Basel, Switzerland)* **14**; 10.3390/ma14226809 (2021).

73. Chen, R.-J., Huang, M., Huang, W.-Z., Shen, Y., Lin, Y.-H. & Nan, C.-W. Sol–gel derived Li–La–Zr–O thin films as solid electrolytes for lithium-ion batteries. *Journal of Materials Chemistry A* **2,** 13277; 10.1039/C4TA02289K (2014).

74. Tadanaga, K., Egawa, H., Hayashi, A., Tatsumisago, M., Mosa, J., Aparicio, M. & Duran, A. Preparation of lithium ion conductive Al-doped Li7La3Zr2O12 thin films by a sol–gel process. *Journal of Power Sources* **273,** 844–847; 10.1016/j.jpowsour.2014.09.164 (2015).

75. Yi, E., Wang, W., Kieffer, J. & Laine, R. M. Flame made nanoparticles permit processing of dense, flexible, Li + conducting ceramic electrolyte thin films of cubic-Li7La3Zr2O12 (c-LLZO). *Journal of Materials Chemistry A* **4,** 12947–12954; 10.1039/C6TA04492A (2016).

76. Yi, E., Wang, W., Kieffer, J. & Laine, R. M. Key parameters governing the densification of cubic-Li7La3Zr2O12 Li+ conductors. *Journal of Power Sources* **352,** 156–164; 10.1016/j.jpowsour.2017.03.126 (2017).

77. Djenadic, R., Botros, M., Benel, C., Clemens, O., Indris, S., Choudhary, A., Bergfeldt, T. & Hahn, H. Nebulized spray pyrolysis of Al-doped Li7La3Zr2O12 solid electrolyte for battery applications. *Solid State Ionics* **263,** 49–56; 10.1016/j.ssi.2014.05.007 (2014).

78. Murugan, R., Thangadurai, V. & Weppner, W. Fast lithium ion conduction in garnet-type Li(7)La(3)Zr(2)O(12). *Angewandte Chemie (International ed. in English)* **46,** 7778–7781; 10.1002/anie.200701144 (2007).

79. Imagawa, H., Ohta, S., Kihira, Y. & Asaoka, T. Garnet-type Li6.75La3Zr1.75Nb0.25O12 synthesized by coprecipitation method and its lithium ion conductivity. *Solid State Ionics* **262,** 609–612; 10.1016/j.ssi.2013.10.059 (2014).

80. Langer, F., Glenneberg, J., Bardenhagen, I. & Kun, R. Synthesis of single phase cubic Al-substituted Li7La3Zr2O12 by solid state lithiation of mixed hydroxides. *Journal of Alloys and Compounds* **645,** 64–69; 10.1016/j.jallcom.2015.03.209 (2015).

81. Geng, H., Chen, K., Di Yi, Mei, A., Huang, M., Lin, Y. & Nan, C. Formation Mechanism of Garnet-Like Li7La3Zr2O12 Powder Prepared by Solid State Reaction. *Rare Metal Materials and Engineering* **45,** 612–616; 10.1016/S1875-5372(16)30081-9 (2016).

82. Rao, R. P., Gu, W., Sharma, N., Peterson, V. K., Avdeev, M. & Adams, S. In Situ Neutron Diffraction Monitoring of Li7La3Zr2O12 Formation: Toward a Rational Synthesis of Garnet Solid Electrolytes. *Chemistry of Materials* **27,** 2903–2910; 10.1021/acs.chemmater.5b00149 (2015).

83. Chen, Y., Rangasamy, E., dela Cruz, C. R., Liang, C. & An, K. A study of suppressed formation of low-conductivity phases in doped Li7La3Zr2O12 garnets by in situ neutron diffraction. *Journal of Materials Chemistry A* **3,** 22868–22876; 10.1039/C5TA04902D (2015).

84. Košir, J., Mousavihashemi, S., Wilson, B. P., Rautama, E.-L. & Kallio, T. Comparative analysis on the thermal, structural, and electrochemical properties of Al-doped Li7La3Zr2O12 solid electrolytes through solid state and sol-gel routes. *Solid State Ionics* **380,** 115943; 10.1016/j.ssi.2022.115943 (2022).

85. Heinrich, J. G. Einführung in die Grundlagen der Keramischen Formgebung.

86. Reinacher, J., Berendts, S. & Janek, J. Preparation and electrical properties of garnet-type Li6BaLa2Ta2O12 lithium solid electrolyte thin films prepared by pulsed laser deposition. *Solid State Ionics* **258,** 1–7; 10.1016/j.ssi.2014.01.046 (2014).

87. Rawlence, M., Garbayo, I., Buecheler, S. & Rupp, J. L. M. On the chemical stability of post-lithiated garnet Al-stabilized Li7La3Zr2O12 solid state electrolyte thin films. *Nanoscale* **8,** 14746–14753; 10.1039/C6NR04162K (2016).

88. Kazyak, E., Chen, K.-H., Wood, K. N., Davis, A. L., Thompson, T., Bielinski, A. R., Sanchez, A. J., Wang, X., Wang, C., Sakamoto, J. & Dasgupta, N. P. Atomic Layer Deposition of the Solid Electrolyte Garnet Li7La3Zr2O12. *Chemistry of Materials* **29,** 3785–3792; 10.1021/acs.chemmater.7b00944 (2017).

89. Ye, R., Hamzelui, N., Ihrig, M., Finsterbusch, M. & Figgemeier, E. Water-Based Fabrication of a Li|Li7La3Zr2O12|LiFePO4 Solid-State Battery─Toward Green Battery Production. *ACS Sustainable Chemistry & Engineering* **10,** 7613–7624; 10.1021/acssuschemeng.2c01349 (2022).

90. Sastre, J., Priebe, A., Döbeli, M., Michler, J., Tiwari, A. N. & Romanyuk, Y. E. Lithium Garnet Li7La3Zr2O12 Electrolyte for All-Solid-State Batteries: Closing the Gap between Bulk and Thin Film Li-Ion Conductivities. *Advanced Materials Interfaces* **7,** 2000425; 10.1002/admi.202000425 (2020).

91. Gong, Y., Fu, K., Xu, S., Dai, J., Hamann, T. R., Zhang, L., Hitz, G. T., Fu, Z., Ma, Z., McOwen, D. W., Han, X., Hu, L. & Wachsman, E. D. Lithium-ion conductive ceramic textile: A new architecture for flexible solid-state lithium metal batteries. *Materials Today* **21,** 594–601; 10.1016/j.mattod.2018.01.001 (2018).

92. Hitz, G. T., McOwen, D. W., Zhang, L., Ma, Z., Fu, Z., Wen, Y., Gong, Y., Dai, J., Hamann, T. R., Hu, L. & Wachsman, E. D. High-rate lithium cycling in a scalable trilayer Li-garnet-electrolyte architecture. *Materials Today* **22,** 50–57; 10.1016/j.mattod.2018.04.004 (2019).

93. Mistler, R. E. & Twiname, E. R. *Tape casting. Theory and practice* (American Ceramic Society, Westerville, OH, 2000).

94. Jonson, R. A. & McGinn, P. J. Tape casting and sintering of Li7La3Zr1.75Nb0.25Al0.1O12 with Li3BO3 additions. *Solid State Ionics* **323,** 49–55; 10.1016/j.ssi.2018.05.015 (2018).

95. Howatt, G. N., Breckenridge, R. G. & Brownlow, J. M. Fabrication Of Thin Ceramic Sheets For Capacitors. *Journal of the American Ceramic Society* **30,** 237–242; 10.1111/j.1151-2916.1947.tb18889.x (1947).

96. Terpstra, R. A., Pex, P. P. A. C. & Vries, A. H. de. *Ceramic Processing* (Springer Netherlands, Dordrecht, 1995).

97. Castro, R. & Benthem, K. (eds.). *Sintering. Mechanisms of Convention Nanodensification and Field Assisted Processes* (Springer Berlin Heidelberg; Imprint; Springer, Berlin, Heidelberg, 2013).

98. Rahaman, M. N. *Sintering of Ceramics* (Taylor and Francis, Hoboken, 2007).

99. Telle, R., Salmang, H. & Scholze, H. (eds.). *Keramik.* 7th ed. (Springer, Berlin, 2007).

100. *Sintering of Advanced Materials* (Elsevier, 2010).

101. German, R. M. Thermodynamics of sintering. In *Sintering of Advanced Materials* (Elsevier2010), pp. 3–32.

102. German, R. M. *Liquid phase sintering* (Plenum Press, New York, 1985).

103. Ihrig, M., Finsterbusch, M., Tsai, C.-L., Laptev, A. M., Tu, C., Bram, M., Sohn, Y. J., Ye, R., Sevinc, S., Lin, S., Fattakhova-Rohlfing, D. & Guillon, O. Low temperature sintering of fully inorganic all-solid-state batteries – Impact of interfaces on full cell performance. *Journal of Power Sources* **482,** 228905; 10.1016/j.jpowsour.2020.228905 (2021).

104. Kim, Y., Jo, H. H., Allen, J. S., Choe, H., Wolfenstine, J. & Sakamoto, J. The Effect of Relative Density on the Mechanical Properties of Hot-Pressed Cubic $Li_7La_3Zr_2O_{12}$. *Journal of the American Ceramic Society*; 10.1111/jace.14084 (2016).

105. Wang, C., Ping, W., Bai, Q., Cui, H., Hensleigh, R., Wang, R., Brozena, A. H., Xu, Z., Dai, J., Pei, Y., Zheng, C., Pastel, G., Gao, J., Wang, X., Wang, H., Zhao, J.-C., Yang, B., Zheng, X. R., Luo, J., Mo, Y., Dunn, B. & Hu, L. A general method to synthesize and sinter bulk ceramics in seconds. *Science (New York, N.Y.)* **368,** 521–526; 10.1126/science.aaz7681 (2020).

106. Heywood, S., Lessmeier, M., Driscoll, D. & Sofie, S. Tailoring solid-state synthesis routes for high confidence production of phase pure, low impedance Al-LLZO. *Journal of the American Ceramic Society* **106,** 2786–2796; 10.1111/jace.18994 (2023).

107. Rosen, M., Ye, R., Mann, M., Lobe, S., Finsterbusch, M., Guillon, O. & Fattakhova-Rohlfing, D. Controlling the lithium proton exchange of LLZO to enable reproducible processing and

performance optimization. *Journal of Materials Chemistry A* **9,** 4831–4840; 10.1039/D0TA11096E (2021).

108. Ye, R., Tsai, C.-L., Ihrig, M., Sevinc, S., Rosen, M., Dashjav, E., Sohn, Y. J., Figgemeier, E. & Finsterbusch, M. Water-based fabrication of garnet-based solid electrolyte separators for solid-state lithium batteries. *Green Chemistry* **22,** 4952–4961; 10.1039/D0GC01009J (2020).

109. Weller, J. M., Whetten, J. A. & Chan, C. K. Nonaqueous Polymer Combustion Synthesis of Cubic Li7La3Zr2O12 Nanopowders. *ACS applied materials & interfaces* **12,** 953–962; 10.1021/acsami.9b19981 (2020).

110. Sakamoto, J., Rangasamy, E., Kim, H., Kim, Y. & Wolfenstine, J. Synthesis of nano-scale fast ion conducting cubic Li7La3Zr2O12. *Nanotechnology* **24,** 424005; 10.1088/0957-4484/24/42/424005 (2013).

111. Shao, C., Liu, H., Yu, Z., Zheng, Z., Sun, N. & Diao, C. Structure and ionic conductivity of cubic Li7La3Zr2O12 solid electrolyte prepared by chemical co-precipitation method. *Solid State Ionics* **287,** 13–16; 10.1016/j.ssi.2016.01.042 (2016).

112. Zhang, Y., Cai, J., Chen, F., Tu, R., Shen, Q., Zhang, X. & Zhang, L. Preparation of cubic Li7La3Zr2O12 solid electrolyte using a nano-sized core–shell structured precursor. *Journal of Alloys and Compounds* **644,** 793–798; 10.1016/j.jallcom.2015.05.085 (2015).

113. Botros, M., Djenadic, R., Clemens, O., Möller, M. & Hahn, H. Field assisted sintering of fine-grained Li7−3La3Zr2AlO12 solid electrolyte and the influence of the microstructure on the electrochemical performance. *Journal of Power Sources* **309,** 108–115; 10.1016/j.jpowsour.2016.01.086 (2016).

114. Guo, J., Weller, J. M., Yang, S., Bhat, M. H. & Chan, C. K. Reactive sintering of garnet-type Li6.4La3Zr1.4Ta0.6O12 (LLZTO) from pyrochlore precursors prepared using a non-aqueous sol–gel method. *Ionics*; 10.1007/s11581-022-04837-4 (2022).

115. Sharafi, A., Kazyak, E., Davis, A. L., Yu, S., Thompson, T., Siegel, D. J., Dasgupta, N. P. & Sakamoto, J. Surface Chemistry Mechanism of Ultra-Low Interfacial Resistance in the Solid-State Electrolyte Li7La3Zr2O12. *Chemistry of Materials* **29,** 7961–7968; 10.1021/acs.chemmater.7b03002 (2017).

116. Sharafi, A., Yu, S., Naguib, M., Lee, M., Ma, C., Meyer, H. M., Nanda, J., Chi, M., Siegel, D. J. & Sakamoto, J. Impact of air exposure and surface chemistry on Li–Li7La3Zr2O12 interfacial resistance. *Journal of Materials Chemistry A* **5,** 13475–13487; 10.1039/c7ta03162a (2017).

117. Liu, C., Rui, K., Shen, C., Badding, M. E., Zhang, G. & Wen, Z. Reversible ion exchange and structural stability of garnet-type Nb-doped Li7La3Zr2O12 in water for applications in lithium batteries. *Journal of Power Sources* **282,** 286–293; 10.1016/j.jpowsour.2015.02.050 (2015).

118. Yang, Y.-N., Li, Y.-X., Li, Y.-Q. & Zhang, T. On-surface lithium donor reaction enables decarbonated lithium garnets and compatible interfaces within cathodes. *Nature Communications* **11,** 5519; 10.1038/s41467-020-19417-1 (2020).

119. Grissa, R., Payandeh, S., Heinz, M. & Battaglia, C. Impact of Protonation on the Electrochemical Performance of Li7La3Zr2O12 Garnets. *ACS Applied Materials & Interfaces* **13,** 14700–14709; 10.1021/acsami.0c23144 (2021).

120. Chen, C., Sun, Y., He, L., Kotobuki, M., Hanc, E., Chen, Y., Zeng, K. & Lu, L. Microstructural and Electrochemical Properties of Al- and Ga-Doped Li7La3Zr2O12 Garnet Solid Electrolytes. *ACS Applied Energy Materials* **3,** 4708–4719; 10.1021/acsaem.0c00347 (2020).

121. Yamazaki, Y., Miyake, S., Akimoto, K. & Inada, R. Effect of Ga2O3 Addition on the Properties of Garnet-Type Ta-Doped Li7La3Zr2O12 Solid Electrolyte. *Batteries* **8,** 158; 10.3390/batteries8100158 (2022).

122. Kim, K. H., Iriyama, Y., Yamamoto, K., Kumazaki, S., Asaka, T., Tanabe, K., Fisher, C. A., Hirayama, T., Murugan, R. & Ogumi, Z. Characterization of the interface between LiCoO2 and Li7La3Zr2O12 in an all-solid-state rechargeable lithium battery. *Journal of Power Sources* **196,** 764–767; 10.1016/j.jpowsour.2010.07.073 (2011).

123. Kim, A., Kang, J.-H., Song, K. & Kang, B. Simultaneously Improved Cubic Phase Stability and Li-Ion Conductivity in Garnet-Type Solid Electrolytes Enabled by Controlling the Al Occupation Sites. *ACS Applied Materials & Interfaces* **14,** 12331–12339; 10.1021/acsami.2c01361 (2022).

124. Xu, L., Tang, S., Cheng, Y., Wang, K., Liang, J., Liu, C., Cao, Y.-C., Wei, F. & Mai, L. Interfaces in Solid-State Lithium Batteries. *Joule* **2,** 1991–2015; 10.1016/j.joule.2018.07.009 (2018).

125. Porz, L., Swamy, T., Sheldon, B. W., Rettenwander, D., Frömling, T., Thaman, H. L., Berendts, S., Uecker, R., Carter, W. C. & Chiang, Y.-M. Mechanism of Lithium Metal Penetration through Inorganic Solid Electrolytes. *Advanced Energy Materials* **7**; 10.1002/aenm.201701003 (2017).

126. Tsai, C.-L., Roddatis, V., Chandran, C. V., Ma, Q., Uhlenbruck, S., Bram, M., Heitjans, P. & Guillon, O. Li7La3Zr2O12 Interface Modification for Li Dendrite Prevention. *ACS Applied Materials & Interfaces* **8,** 10617–10626; 10.1021/acsami.6b00831 (2016).

127. Zhu, Y., Connell, J. G., Tepavcevic, S., Zapol, P., Garcia-Mendez, R., Taylor, N. J., Sakamoto, J., Ingram, B. J., Curtiss, L. A., Freeland, J. W., Fong, D. D. & Markovic, N. M. Dopant-Dependent Stability of Garnet Solid Electrolyte Interfaces with Lithium Metal. *Advanced Energy Materials* **9,** 1803440; 10.1002/aenm.201803440 (2019).

128. Wang, M., Wolfenstine, J. B. & Sakamoto, J. Temperature dependent flux balance of the Li/Li7La3Zr2O12 interface. *Electrochimica Acta* **296,** 842–847; 10.1016/j.electacta.2018.11.034 (2019).

129. Kim, M., Ahn, H., Choi, J. & Kim, W. B. A Rational Design of Silicon-Based Anode for All-Solid-State Lithium-Ion Batteries: A Review. *Energy Technology* **11**; 10.1002/ente.202201321 (2023).

130. Fu, K. K., Gong, Y., Liu, B., Zhu, Y., Xu, S., Yao, Y., Luo, W., Wang, C., Lacey, S. D., Dai, J., Chen, Y., Mo, Y., Wachsman, E. & Hu, L. Toward garnet electrolyte-based Li metal batteries: An ultrathin, highly effective, artificial solid-state electrolyte/metallic Li interface. *Science advances* **3,** e1601659; 10.1126/sciadv.1601659 (2017).

131. Ouyang, C., Shi, S., Wang, Z., Huang, X. & Chen, L. First-principles study of Li ion diffusion in LiFePO4. *Physical Review B* **69**; 10.1103/PhysRevB.69.104303 (2004).

132. Bazito, F. F. C. & Torresi, R. M. Cathodes for lithium ion batteries: the benefits of using nanostructured materials. *Journal of the Brazilian Chemical Society* **17,** 627–642; 10.1590/S0103-50532006000400002 (2006).

133. Julien, C. M. & Mauger, A. Review of 5-V electrodes for Li-ion batteries: status and trends. *Ionics* **19,** 951–988; 10.1007/s11581-013-0913-2 (2013).

134. Ren, Y., Liu, T., Shen, Y., Lin, Y. & Nan, C.-W. Chemical compatibility between garnet-like solid state electrolyte Li6.75La3Zr1.75Ta0.25O12 and major commercial lithium battery cathode materials. *Journal of Materiomics* **2,** 256–264; 10.1016/j.jmat.2016.04.003 (2016).

135. Kim, Y., Kim, D., Bliem, R., Vardar, G., Waluyo, I., Hunt, A., Wright, J. T., Katsoudas, J. P. & Yildiz, B. Thermally Driven Interfacial Degradation between Li7La3Zr2O12 Electrolyte and LiNi0.6Mn0.2Co0.2O2 Cathode. *Chemistry of Materials* **32,** 9531–9541; 10.1021/acs.chemmater.0c02261 (2020).

136. Wakasugi, J., Munakata, H. & Kanamura, K. Thermal Stability of Various Cathode Materials against Li6.25Al0.25La3Zr2O12 Electrolyte. *Electrochemistry* **85,** 77–81; 10.5796/electrochemistry.85.77 (2017).

137. Zhang, N., Long, X., Wang, Z., Yu, P., Han, F., Fu, J., Ren, G., Wu, Y., Zheng, S., Huang, W., Wang, C., Li, H. & Liu, X. Mechanism Study on the Interfacial Stability of a Lithium Garnet-Type Oxide Electrolyte against Cathode Materials. *ACS Applied Energy Materials* **1,** 5968–5976; 10.1021/acsaem.8b01035 (2018).

138. Padhi, A. K., Nanjundaswamy, K. S. & Goodenough, J. B. Phospho-olivines as Positive-Electrode Materials for Rechargeable Lithium Batteries. *Journal of The Electrochemical Society* **144,** 1188–1194; 10.1149/1.1837571 (1997).

139. Yoon, W.-S., Chung, K. Y., McBreen, J. & Yang, X.-Q. A comparative study on structural changes of LiCo1/3Ni1/3Mn1/3O2 and LiNi0.8Co0.15Al0.05O2 during first charge using in situ XRD. *Electrochemistry Communications* **8,** 1257–1262; 10.1016/j.elecom.2006.06.005 (2006).

140. Reimers, J. N. & Dahn, J. R. Electrochemical and In Situ X-Ray Diffraction Studies of Lithium Intercalation in Li x CoO2. *Journal of The Electrochemical Society* **139,** 2091–2097; 10.1149/1.2221184 (1992).

141. Mizushima, K., Jones, P. C., Wiseman, P. J. & Goodenough, J. B. LixCoO2 (0<x<-1): A new cathode material for batteries of high energy density. *Materials Research Bulletin* **15,** 783–789; 10.1016/0025-5408(80)90012-4 (1980).

142. Nazri, G.-A. & Pistoia, G. (eds.). *Lithium Batteries. Science and Technology* (Springer US, Boston, MA, 2003).

143. Wang, H., Jang, Y.-I., Huang, B., Sadoway, D. R. & Chiang, Y.-M. TEM Study of Electrochemical Cycling-Induced Damage and Disorder in LiCoO2 Cathodes for Rechargeable Lithium Batteries. *Journal of The Electrochemical Society* **146,** 473–480; 10.1149/1.1391631 (1999).

144. Tsai, Y. W., Hwang, B. J., Ceder, G., Sheu, H. S., Liu, D. G. & Lee, J. F. In-Situ X-ray Absorption Spectroscopic Study on Variation of Electronic Transitions and Local Structure of LiNi1/3Co1/3Mn1/3O2 Cathode Material during Electrochemical Cycling. *Chemistry of Materials* **17,** 3191–3199; 10.1021/cm048027v (2005).

145. Ohzuku, T. & Ueda, A. Solid-State Redox Reactions of LiCoO2 (R3m) for 4 Volt Secondary Lithium Cells. *Journal of The Electrochemical Society* **141,** 2972–2977; 10.1149/1.2059267 (1994).

146. Botelho Junior, A. B., Stopic, S., Friedrich, B., Tenório, J. A. S. & Espinosa, D. C. R. Cobalt Recovery from Li-Ion Battery Recycling: A Critical Review. *Metals* **11,** 1999; 10.3390/met11121999 (2021).

147. Indu, M. S., Alexander, G. V., Sreejith, O. V., Abraham, S. E. & Murugan, R. Lithium garnet-cathode interfacial chemistry: inclusive insights and outlook toward practical solid-state lithium metal batteries. *Materials Today Energy* **21,** 100804; 10.1016/j.mtener.2021.100804 (2021).

148. Sastre, J., Chen, X., Aribia, A., Tiwari, A. N. & Romanyuk, Y. E. Fast Charge Transfer across the Li7La3Zr2O12 Solid Electrolyte/LiCoO2 Cathode Interface Enabled by an Interphase-Engineered All-Thin-Film Architecture. *ACS Applied Materials & Interfaces* **12,** 36196–36207; 10.1021/acsami.0c09777 (2020).

149. Ihrig, M., Finsterbusch, M., Laptev, A. M., Tu, C., Tran, N. T. T., Lin, C.-A., Kuo, L.-Y., Ye, R., Sohn, Y. J., Kaghazchi, P., Lin, S., Fattakhova-Rohlfing, D. & Guillon, O. Study of LiCoO2/Li7La3Zr2O12:Ta Interface Degradation in All-Solid-State Lithium Batteries. *ACS Applied Materials & Interfaces* **14,** 11288–11299; 10.1021/acsami.1c22246 (2022).

150. Kim, K. J. & Rupp, J. L. M. All ceramic cathode composite design and manufacturing towards low interfacial resistance for garnet-based solid-state lithium batteries. *Energy & Environmental Science* **13,** 4930–4945; 10.1039/D0EE02062A (2020).

151. Morozov, A. V., Paik, H., Boev, A. O., Aksyonov, D. A., Lipovskikh, S. A., Stevenson, K. J., Rupp, J. L. M. & Abakumov, A. M. Thermodynamics as a Driving Factor of LiCoO2 Grain Growth on Nanocrystalline Ta-LLZO Thin Films for All-Solid-State Batteries. *ACS Applied Materials & Interfaces* **14,** 39907–39916; 10.1021/acsami.2c07176 (2022).

152. Kato, T., Hamanaka, T., Yamamoto, K., Hirayama, T., Sagane, F., Motoyama, M. & Iriyama, Y. In-situ Li7La3Zr2O12/LiCoO2 interface modification for advanced all-solid-state battery. *Journal of Power Sources* **260,** 292–298; 10.1016/j.jpowsour.2014.02.102 (2014).

153. Vardar, G., Bowman, W. J., Lu, Q., Wang, J., Chater, R. J., Aguadero, A., Seibert, R., Terry, J., Hunt, A., Waluyo, I., Fong, D. D., Jarry, A., Crumlin, E. J., Hellstrom, S. L., Chiang, Y.-M. & Yildiz, B. Structure, Chemistry, and Charge Transfer Resistance of the Interface between Li7La3Zr2O12 Electrolyte and LiCoO2 Cathode. *Chemistry of Materials* **30,** 6259–6276; 10.1021/acs.chemmater.8b01713 (2018).

154. Ren, Y. & Wachsman, E. D. All Solid-State Li/LLZO/LCO Battery Enabled by Alumina Interfacial Coating. *Journal of The Electrochemical Society* **169,** 40529; 10.1149/1945-7111/ac644f (2022).

155. Park, K., Yu, B.-C., Jung, J.-W., Li, Y., Zhou, W., Gao, H., Son, S. & Goodenough, J. B. Electrochemical Nature of the Cathode Interface for a Solid-State Lithium-Ion Battery: Interface between LiCoO2 and Garnet-Li7La3Zr2O12. *Chemistry of Materials* **28,** 8051–8059; 10.1021/acs.chemmater.6b03870 (2016).

156. Tsai, C.-L., Yu, S., Tempel, H., Kungl, H. & Eichel, R.-A. All-ceramic Li batteries based on garnet structured Li7La3Zr2O12. *Materials Technology* **35,** 656–674; 10.1080/10667857.2020.1746539 (2020).

157. Scheld, W. S., Lobe, S., Dellen, C., Ihrig, M., Häuschen, G., Hoff, L. C., Finsterbusch, M., Uhlenbruck, S., Guillon, O. & Fattakhova-Rohlfing, D. Rapid thermal processing of garnet-based composite cathodes. *Journal of Power Sources* **545,** 231872; 10.1016/j.jpowsour.2022.231872 (2022).

158. Tsai, C.-L., Ma, Q., Dellen, C., Lobe, S., Vondahlen, F., Windmüller, A., Grüner, D., Zheng, H., Uhlenbruck, S., Finsterbusch, M., Tietz, F., Fattakhova-Rohlfing, D., Buchkremer, H. P. & Guillon, O. A garnet structure-based all-solid-state Li battery without interface modification: resolving incompatibility issues on positive electrodes. *Sustainable Energy & Fuels* **3,** 280–291; 10.1039/C8SE00436F (2019).

159. Rosen, M., Finsterbusch, M., Guillon, O. & Fattakhova-Rohlfing, D. Free standing dual phase cathode tapes – scalable fabrication and microstructure optimization of garnet-based ceramic cathodes. *Journal of Materials Chemistry A* **10,** 2320–2326; 10.1039/D1TA07194G (2022).

160. Tsai, C.-L., Dashjav, E., Hammer, E.-M., Finsterbusch, M., Tietz, F., Uhlenbruck, S. & Buchkremer, H. P. High conductivity of mixed phase Al-substituted Li7La3Zr2O12. *Journal of Electroceramics* **35,** 25–32; 10.1007/s10832-015-9988-7 (2015).

161. Amdouni, N., Zarrouk, H., Soulette, F. & Julien, C. LiAlyCo1−yO2 (0.0≤y≤0.3) intercalation compounds synthesized from the citrate precursors. *Materials Chemistry and Physics* **80,** 205–214; 10.1016/S0254-0584(02)00491-1 (2003).

162. Mücke, R., Finsterbusch, M., Kaghazchi, P., Fattakhova-Rohlfing, D. & Guillon, O. Modelling electro-chemical induced stresses in all-solid-state batteries: Anisotropy effects in cathodes and cell design optimisation. *Journal of Power Sources* **489,** 229430; 10.1016/j.jpowsour.2020.229430 (2021).

163. Feng, L., Li, L., Zhang, Y., Peng, H. & Zou, Y. Low temperature synthesis and ion conductivity of Li7La3Zr2O12 garnets for solid state Li ion batteries. *Solid State Ionics* **310,** 129–133; 10.1016/j.ssi.2017.08.016 (2017).

164. Yan, X., Li, Z., Wen, Z. & Han, W. Li/Li7La3Zr2O12 /LiFePO4 All-Solid-State Battery with Ultrathin Nanoscale Solid Electrolyte. *The Journal of Physical Chemistry C* **121,** 1431–1435; 10.1021/acs.jpcc.6b10268 (2017).

165. Zhu, Y., He, X. & Mo, Y. First principles study on electrochemical and chemical stability of solid electrolyte–electrode interfaces in all-solid-state Li-ion batteries. *Journal of Materials Chemistry A* **4,** 3253–3266; 10.1039/C5TA08574H (2016).

166. Kotobuki, M., Munakata, H., Kanamura, K., Sato, Y. & Yoshida, T. Compatibility of Li7La3Zr2O12 Solid Electrolyte to All-Solid-State Battery Using Li Metal Anode. *Journal of The Electrochemical Society* **157,** A1076; 10.1149/1.3474232 (2010).

167. Uhlenbruck, S., Dornseiffer, J., Lobe, S., Dellen, C., Tsai, C.-L., Gotzen, B., Sebold, D., Finsterbusch, M. & Guillon, O. Cathode-electrolyte material interactions during manufacturing of inorganic solid-state lithium batteries. *Journal of Electroceramics* **38,** 197–206; 10.1007/s10832-016-0062-x (2017).

168. Ihrig, M., Kuo, L.-Y., Lobe, S., Laptev, A. M., Lin, C.-A., Tu, C., Ye, R., Kaghazchi, P., Cressa, L., Eswara, S., Lin, S., Guillon, O., Fattakhova-Rohlfing, D. & Finsterbusch, M. Thermal Recovery of the Electrochemically Degraded LiCoO2/Li7La3Zr2O12:Al,Ta Interface in an All-Solid-State Lithium Battery. *ACS Applied Materials & Interfaces* **15,** 4101–4112; 10.1021/acsami.2c20004 (2023).

169. Huo, H., Chen, Y., Li, R., Zhao, N., Luo, J., Da Pereira Silva, J. G., Mücke, R., Kaghazchi, P., Guo, X. & Sun, X. Design of a mixed conductive garnet/Li interface for dendrite-free solid lithium metal batteries. *Energy & Environmental Science* **13,** 127–134; 10.1039/C9EE01903K (2020).

170. Alexander, G. V., Patra, S., Sobhan Raj, S. V., Sugumar, M. K., Ud Din, M. M. & Murugan, R. Electrodes-electrolyte interfacial engineering for realizing room temperature lithium metal battery based on garnet structured solid fast Li+ conductors. *Journal of Power Sources* **396,** 764–773; 10.1016/j.jpowsour.2018.06.096 (2018).

171. Han, F., Yue, J., Chen, C., Zhao, N., Fan, X., Ma, Z., Gao, T., Wang, F., Guo, X. & Wang, C. Interphase Engineering Enabled All-Ceramic Lithium Battery. *Joule* **2,** 497–508; 10.1016/j.joule.2018.02.007 (2018).

172. Ohta, S., Seki, J., Yagi, Y., Kihira, Y., Tani, T. & Asaoka, T. Co-sinterable lithium garnet-type oxide electrolyte with cathode for all-solid-state lithium ion battery. *Journal of Power Sources* **265,** 40–44; 10.1016/j.jpowsour.2014.04.065 (2014).

173. Kushnir, D. & Sandén, B. A. The time dimension and lithium resource constraints for electric vehicles. *Resources Policy* **37,** 93–103; 10.1016/j.resourpol.2011.11.003 (2012).

174. Gruber, P. W., Medina, P. A., Keoleian, G. A., Kesler, S. E., Everson, M. P. & Wallington, T. J. Global Lithium Availability. *Journal of Industrial Ecology* **15,** 760–775; 10.1111/j.1530-9290.2011.00359.x (2011).

175. Delucchi, M. A., Yang, C., Burke, A. F., Ogden, J. M., Kurani, K., Kessler, J. & Sperling, D. An assessment of electric vehicles: technology, infrastructure requirements, greenhouse-gas emissions, petroleum use, material use, lifetime cost, consumer acceptance and policy initiatives. *Philosophical transactions. Series A, Mathematical, physical, and engineering sciences* **372,** 20120325; 10.1098/rsta.2012.0325 (2014).

176. Schirmer, T., Qiu, H., Goldmann, D., Stallmeister, C. & Friedrich, B. Influence of P and Ti on Phase Formation at Solidification of Synthetic Slag Containing Li, Zr, La, and Ta. *Minerals* **12,** 310; 10.3390/min12030310 (2022).

177. Takacova, Z., Orac, D., Klimko, J. & Miskufova, A. Current Trends in Spent Portable Lithium Battery Recycling. *Materials (Basel, Switzerland)* **16**; 10.3390/ma16124264 (2023).

178. Qiu, H., Goldmann, D., Stallmeister, C., Friedrich, B., Tobaben, M., Kwade, A., Peschel, C., Winter, M., Nowak, S., Lyon, T. & Peuker, U. A. The InnoRec Process: A Comparative Study of Three Mainstream Routes for Spent Lithium-ion Battery Recycling Based on the Same Feedstock. *Sustainability* **16,** 3876; 10.3390/su16093876 (2024).

179. Georgi-Maschler, T., Friedrich, B., Weyhe, R., Heegn, H. & Rutz, M. Development of a recycling process for Li-ion batteries. *Journal of Power Sources* **207,** 173–182; 10.1016/j.jpowsour.2012.01.152 (2012).

180. Pistoia, G. & Liaw, B. Y. *Behaviour of Lithium-Ion Batteries in Electric Vehicles. Battery Health, Performance, Safety, and Cost* (Springer International Publishing, Basel, 2018).

181. Diekmann, J., Hanisch, C., Froböse, L., Schälicke, G., Loellhoeffel, T., Fölster, A.-S. & Kwade, A. Ecological Recycling of Lithium-Ion Batteries from Electric Vehicles with Focus on Mechanical Processes. *Journal of The Electrochemical Society* **164,** A6184-A6191; 10.1149/2.0271701jes (2017).

182. Harper, G. D. J., Kendrick, E., Anderson, P. A., Mrozik, W., Christensen, P., Lambert, S., Greenwood, D., Das, P. K., Ahmeid, M., Milojevic, Z., Du, W., Brett, D. J. L., Shearing, P. R., Rastegarpanah, A., Stolkin, R., Sommerville, R., Zorin, A., Durham, J. L., Abbott, A. P., Thompson, D., Browning, N. D., Mehdi, B. L., Bahri, M., Schanider-Tontini, F., Nicholls, D., Stallmeister, C., Friedrich, B., Sommerfeld, M., Driscoll, L. L., Jarvis, A., Giles, E. C., Slater, P. R., Echavarri-Bravo, V., Maddalena, G., Horsfall, L. E., Gaines, L., Dai, Q., Jethwa, S. J., Lipson, A. L., Leeke, G. A., Cowell, T., Farthing, J. G., Mariani, G., Smith, A., Iqbal, Z., Golmohammadzadeh, R., Sweeney, L., Goodship, V., Li, Z., Edge, J., Lander, L., Nguyen, V. T., Elliot, R. J. R., Heidrich, O., Slattery, M., Reed, D., Ahuja, J., Cavoski, A., Lee, R., Driscoll, E., Baker, J., Littlewood, P., Styles, I., Mahanty, S. & Boons, F. Roadmap for a sustainable circular economy in lithium-ion and future battery technologies. *Journal of Physics: Energy* **5,** 21501; 10.1088/2515-7655/acaa57 (2023).

183. Hanisch, C., Diekmann, J., Stieger, A., Haselrieder, W. & Kwade, A. Recycling of Lithium-Ion Batteries. In *Handbook of clean energy systems,* edited by R. F. Boehm, H. Yang & J. Yan (John Wiley & Sons, Inc, Chichester, West Sussex, 2015-), pp. 1–24.

184. Brückner, L., Frank, J. & Elwert, T. Industrial Recycling of Lithium-Ion Batteries—A Critical Review of Metallurgical Process Routes. *Metals* **10,** 1107; 10.3390/met10081107 (2020).

185. Vanderbruggen, A., Sygusch, J., Rudolph, M. & Serna-Guerrero, R. A contribution to understanding the flotation behavior of lithium metal oxides and spheroidized graphite for lithium-ion battery recycling. *Colloids and Surfaces A: Physicochemical and Engineering Aspects* **626,** 127111; 10.1016/j.colsurfa.2021.127111 (2021).

186. Lain, M. J. Recycling of lithium ion cells and batteries. *Journal of Power Sources* **97-98,** 736–738; 10.1016/S0378-7753(01)00600-0 (2001).

187. Bi, H., Zhu, H., Zu, L., He, S., Gao, Y. & Gao, S. Pneumatic separation and recycling of anode and cathode materials from spent lithium iron phosphate batteries. *Waste management & research : the journal of the International Solid Wastes and Public Cleansing Association, ISWA* **37,** 374–385; 10.1177/0734242X18823939 (2019).

188. Li, L., Dunn, J. B., Zhang, X. X., Gaines, L., Chen, R. J., Wu, F. & Amine, K. Recovery of metals from spent lithium-ion batteries with organic acids as leaching reagents and environmental assessment. *Journal of Power Sources* **233,** 180–189; 10.1016/j.jpowsour.2012.12.089 (2013).

189. C. K. Gupta, T. K. Mukherjee. *Hydrometallurgy in Extraction Processes, Volume II* (Routledge, 2017).

190. Nasser, O. A. & Petranikova, M. Review of Achieved Purities after Li-ion Batteries Hydrometallurgical Treatment and Impurities Effects on the Cathode Performance. *Batteries* **7,** 60; 10.3390/batteries7030060 (2021).

191. Schwich, L., Schubert, T. & Friedrich, B. Early-Stage Recovery of Lithium from Tailored Thermal Conditioned Black Mass Part I: Mobilizing Lithium via Supercritical CO2-Carbonation. *Metals* **11,** 177; 10.3390/met11020177 (2021).

192. Munchen, D. D., Milicevic Neumann, K., Öner, I. E. & Friedrich, B. Transfer of Early-Stage Lithium Recovery from Laboratory-Scale Water Leaching to Upscale Challenges. *Metals* **14,** 67; 10.3390/met14010067 (2024).

193. Gaines, L. & Wang, Y. How to Maximize the Value Recovered from Li-Ion Batteries: Hydrometallurgical or Direct Recycling? *The Electrochemical Society Interface* **30,** 51–54; 10.1149/2.F07213F (2021).

194. Gaines, L., Sullivan, J., Burnham, A. & Belharouak, I. Life-Cycle Analysis of Production and Recycling of Lithium Ion Batteries. *Transportation Research Record: Journal of the Transportation Research Board* **2252,** 57–65; 10.3141/2252-08 (2011).

195. Ganter, M. J., Landi, B. J., Babbitt, C. W., Anctil, A. & Gaustad, G. Cathode refunctionalization as a lithium ion battery recycling alternative. *Journal of Power Sources* **256,** 274–280; 10.1016/j.jpowsour.2014.01.078 (2014).

196. Cao, Y., Li, J., Ji, H., Wei, X., Zhou, G. & Cheng, H.-M. A review of direct recycling methods for spent lithium-ion batteries. *Energy Storage Materials* **70,** 103475; 10.1016/j.ensm.2024.103475 (2024).

197. Nie, H., Xu, L., Song, D., Song, J., Shi, X., Wang, X., Zhang, L. & Yuan, Z. LiCoO 2 : recycling from spent batteries and regeneration with solid state synthesis. *Green Chemistry* **17,** 1276–1280; 10.1039/C4GC01951B (2015).

198. Yang, T., Lu, Y., Li, L., Ge, D., Yang, H., Leng, W., Zhou, H., Han, X., Schmidt, N., Ellis, M. & Li, Z. An Effective Relithiation Process for Recycling Lithium-Ion Battery Cathode Materials. *Advanced Sustainable Systems* **4,** 1900088; 10.1002/adsu.201900088 (2020).

199. Yang, Y., Liu, Z., Zhang, J., Chen, Y. & Wang, C. Economical and low-carbon regeneration of spent LiFePO4 materials by hydrothermal relithiation. *Journal of Alloys and Compounds* **947,** 169660; 10.1016/j.jallcom.2023.169660 (2023).

200. Tran, M. K., Rodrigues, M.-T. F., Kato, K., Babu, G. & Ajayan, P. M. Deep eutectic solvents for cathode recycling of Li-ion batteries. *Nature Energy* **4,** 339–345; 10.1038/s41560-019-0368-4 (2019).

201. Li, X., Liu, S., Yang, J., He, Z., Zheng, J. & Li, Y. Electrochemical methods contribute to the recycling and regeneration path of lithium-ion batteries. *Energy Storage Materials* **55,** 606–630; 10.1016/j.ensm.2022.12.022 (2023).

202. Azhari, L., Bong, S., Ma, X. & Wang, Y. Recycling for All Solid-State Lithium-Ion Batteries. *Matter* **3,** 1845–1861; 10.1016/j.matt.2020.10.027 (2020).

203. Ahuis, M., Doose, S., Vogt, D., Michalowski, P., Zellmer, S. & Kwade, A. Recycling of solid-state batteries. *Nature Energy* **9,** 373–385; 10.1038/s41560-024-01463-4 (2024).

204. Schneider, K., Kiyek, V., Finsterbusch, M., Yagmurlu, B. & Goldmann, D. Acid Leaching of Al- and Ta-Substituted Li7La3Zr2O12 (LLZO) Solid Electrolyte. *Metals* **13,** 834; 10.3390/met13050834 (2023).

205. Shi, Y., Chen, G. & Chen, Z. Effective regeneration of LiCoO2 from spent lithium-ion batteries: a direct approach towards high-performance active particles. *Green Chemistry* **20,** 851–862; 10.1039/C7GC02831H (2018).

206. Sloop, S. E., Trevey, J. E., Gaines, L., Lerner, M. M. & Xu, W. Advances in Direct Recycling of Lithium-Ion Electrode Materials. *ECS Transactions* **85,** 397–403; 10.1149/08513.0397ecst (2018).

207. Scheld, W. S., Kim, K., Schwab, C., Moy, A. C., Jiang, S.-K., Mann, M., Dellen, C., Sohn, Y. J., Lobe, S., Ihrig, M., Danner, M. G., Chang, C.-Y., Uhlenbruck, S., Wachsman, E. D., Hwang, B. J., Sakamoto, J., Wan, L. F., Wood, B. C., Finsterbusch, M. & Fattakhova-Rohlfing, D. The Riddle of Dark LLZO: Cobalt Diffusion in Garnet Separators of Solid-State Lithium Batteries. *Advanced Functional Materials*; 10.1002/adfm.202302939 (2023).

208. Seeck, O. H. *X-ray Diffraction: Modern Experimental Techniques* (CRC Press, 2015).

209. Sardela, M. (ed.). *Practical materials characterization* (Springer, New York NY, 2014).

210. Bruker AXS. TOPAS - General profile and structure analysis software for powder diffraction data. Bruker AXS, 2008.

211. Radamson, H. H., Hallén, A., Sychugov, I. & Azarov, A. *Analytical Methods and Instruments for Micro- and Nanomaterials.* 1st ed. (Springer International Publishing; Imprint Springer, Cham, 2023).

212. Okano, Y. Scanning Electron Microscopy. In *Compendium of Surface and Interface Analysis,* edited by T. S. S. S. o. Japa (Springer Singapore, Singapore, 2018), pp. 563–569.

213. Fu, S., Arinicheva, Y., Hüter, C., Finsterbusch, M. & Spatschek, R. Grain Boundary Characterization and Potential Percolation of the Solid Electrolyte LLZO. *Batteries* **9,** 222; 10.3390/batteries9040222 (2023).

214. Schindelin, J., Arganda-Carreras, I., Frise, E., Kaynig, V., Longair, M., Pietzsch, T., Preibisch, S., Rueden, C., Saalfeld, S., Schmid, B., Tinevez, J.-Y., White, D. J., Hartenstein, V., Eliceiri, K., Tomancak, P. & Cardona, A. Fiji: an open-source platform for biological-image analysis. *Nature methods* **9,** 676–682; 10.1038/nmeth.2019 (2012).

215. Mallick, P. K. *Fundamentals of Molecular Spectroscopy* (Springer Nature Singapore, Singapore, 2023).

216. Saletnik, A., Saletnik, B. & Puchalski, C. Overview of Popular Techniques of Raman Spectroscopy and Their Potential in the Study of Plant Tissues. *Molecules (Basel, Switzerland)* **26**; 10.3390/molecules26061537 (2021).

217. Fearn, S. *An introduction to time-of-flight secondary ion mass spectrometry (ToF-SIMS) and its application to materials science* (Morgan & Claypool Publishers; Morgan & Claypool, San Rafael, CA, San Rafael, Calif., 2015).

218. Kiyek, V., Schwab, C., Scheld, W. S., Roitzheim, C., Lindner, A., Menesklou, W., Finsterbusch, M., Fattakhova-Rohlfing, D. & Guillon, O. Direct Precursor Route for the Fabrication of LLZO Composite Cathodes for Solid-State Batteries. *Advanced science (Weinheim, Baden-Wurttemberg, Germany)* **11,** e2404682; 10.1002/advs.202404682 (2024).

219. Buschmann, H., Berendts, S., Mogwitz, B. & Janek, J. Lithium metal electrode kinetics and ionic conductivity of the solid lithium ion conductors “Li7La3Zr2O12” and Li7−La3Zr2−Ta O12 with garnet-type structure. *Journal of Power Sources* **206,** 236–244; 10.1016/j.jpowsour.2012.01.094 (2012).

220. Irvine, J. T. S., Sinclair, D. C. & West, A. R. Electroceramics: Characterization by Impedance Spectroscopy. *Advanced Materials* **2,** 132–138; 10.1002/adma.19900020304 (1990).

221. Philipp, M., Gadermaier, B., Posch, P., Hanzu, I., Ganschow, S., Meven, M., Rettenwander, D., Redhammer, G. J. & Wilkening, H. M. R. The Electronic Conductivity of Single Crystalline Ga-Stabilized Cubic Li7La3Zr2O12 : A Technologically Relevant Parameter for All-Solid-State Batteries. *Advanced Materials Interfaces* **7**; 10.1002/admi.202000450 (2020).

222. Zhang, C., Hu, Q., Shen, Y. & Liu, W. Fast-Charging Solid-State Lithium Metal Batteries: A Review. *Advanced Energy and Sustainability Research* **3**; 10.1002/aesr.202100203 (2022).

223. Jim Motavalli. Battery Plant Scrap Rates Can Hit 90% at Ramp Up, but the Situation is Improving. It can take a company years to make up for the massive costs of starting up a battery plant. *Autoweek* **2024** (2024).

224. Anderson, E., Jonderian, A., Khaliullin, R. Z. & McCalla, E. Combinatorial study of the Li-La-Zr-O system. *Solid State Ionics* **388,** 116087; 10.1016/j.ssi.2022.116087 (2022).

225. Paolella, A., Zhu, W., Bertoni, G., Savoie, S., Feng, Z., Demers, H., Gariepy, V., Girard, G., Rivard, E., Delaporte, N., Guerfi, A., Lorrmann, H., George, C. & Zaghib, K. Discovering the Influence of Lithium Loss on Garnet Li 7 La 3 Zr 2 O 12 Electrolyte Phase Stability. *ACS Applied Energy Materials* **3,** 3415–3424; 10.1021/acsaem.9b02401 (2020).

226. Yang, L., Dai, Q., Liu, L., Shao, D., Luo, K., Jamil, S., Liu, H., Luo, Z., Chang, B. & Wang, X. Rapid sintering method for highly conductive Li7La3Zr2O12 ceramic electrolyte. *Ceramics International* **46,** 10917–10924; 10.1016/j.ceramint.2020.01.106 (2020).

227. Rawlence, M., Filippin, A. N., Wäckerlin, A., Lin, T.-Y., Cuervo-Reyes, E., Remhof, A., Battaglia, C., Rupp, J. L. M. & Buecheler, S. Effect of Gallium Substitution on Lithium-Ion Conductivity and Phase Evolution in Sputtered Li7-3 xGa xLa3Zr2O12 Thin Films. *ACS Applied Materials & Interfaces* **10,** 13720–13728; 10.1021/acsami.8b03163 (2018).

228. Vandermeulen, W. & Bosch, R.-W. Stress-Induced Degradation of 5 mol% Yttria–zirconia in Water at 300 °C. *Sn Applied Sciences*; 10.1007/s42452-019-0967-5 (2019).

229. Reed, J. S. *Principles of ceramics processing.* 2nd ed. (Wiley, New York, 1995).

230. Cheng, L., Chen, W., Kunz, M., Persson, K., Tamura, N., Chen, G. & Doeff, M. Effect of surface microstructure on electrochemical performance of garnet solid electrolytes. *ACS Applied Materials & Interfaces* **7,** 2073–2081; 10.1021/am508111r (2015).

231. Knudsen, F. P. Dependence of Mechanical Strength of Brittle Polycrystalline Specimens on Porosity and Grain Size. *Journal of the American Ceramic Society* **42,** 376–387; 10.1111/j.1151-2916.1959.tb13596.x (1959).

232. Huang, X., Liu, C., Lu, Y., Xiu, T., Jin, J., Badding, M. E. & Wen, Z. A Li-Garnet composite ceramic electrolyte and its solid-state Li-S battery. *Journal of Power Sources* **382,** 190–197; 10.1016/j.jpowsour.2017.11.074 (2018).

233. Guo, J. & Chan, C. K. Lithium Dendrite Propagation in Ta-Doped Li7La3Zr2O12 (LLZTO): Comparison of Reactively Sintered Pyrochlore-to-Garnet vs LLZTO by Solid-State Reaction and Conventional Sintering. *ACS Applied Materials & Interfaces* **16,** 4519–4529; 10.1021/acsami.3c11421 (2024).

234. Müller, M., Schmieg, J., Dierickx, S., Joos, J., Weber, A., Gerthsen, D. & Ivers-Tiffée, E. Reducing Impedance at a Li-Metal Anode/Garnet-Type Electrolyte Interface Implementing Chemically Resolvable In Layers. *ACS Applied Materials & Interfaces* **14,** 14739–14752; 10.1021/acsami.1c25257 (2022).

235. Xu, C., Uahengo, G., Rudnicki, C., Hung, C., Huang, A., Xu, Q., Chen, Y., Halaney, D. L., Garay, J. E., Mangolini, L., Aguilar, G. & Liu, H. H. Nanocrystalline Yttria-Stabilized Zirconia Ceramics for Cranial Window Applications. *ACS applied bio materials* **5,** 2664–2675; 10.1021/acsabm.2c00119 (2022).

236. Green, D. J., Guillon, O. & Rödel, J. Constrained sintering: A delicate balance of scales. *Journal of the European Ceramic Society* **28,** 1451–1466; 10.1016/j.jeurceramsoc.2007.12.012 (2008).

237. Zhou, H. Li_5AlO_4-Assisted Low-Temperature Sintering of Dense $Li_7La_3Zr_2O_{12}$ Solid Electrolyte With High Critical Current Density. *ACS Applied Materials & Interfaces*; 10.1021/acsami.3c17606 (2024).

238. Skokan, A. Phase staility investigations in the ceramic breeder systems Li2O-Al2O3 and Li2O-ZrO2. In *Fusion technology 1990. Vol. 1-2. Proceedings. 16th SOFT 1990,* edited by R. Hemsworth, M. Huguet & B. E. Keen (North-Holland, Amsterdam, 1991), pp. 772–776.

239. Konar, B., van Ende, M.-A. & Jung, I.-H. Critical Evaluation and Thermodynamic Optimization of the Li2O-Al2O3 and Li2O-MgO-Al2O3 Systems. *Metallurgical and Materials Transactions B* **49,** 2917–2944; 10.1007/s11663-018-1349-x (2018).

240. Aksay, I. A., Hoge, C. E. & Pask, J. A. Wetting under chemical equilibrium and nonequilibrium conditions. *The Journal of Physical Chemistry* **78,** 1178–1183; 10.1021/j100605a009 (1974).

241. Navrotsky, A. & Ushakov, S. V. Thermodynamics of Oxide Systems Relevant to Alternative Gate Dielectrics. In *Materials Fundamentals of Gate Dielectrics,* edited by A. A. Demkov & A. Navrotsky (Springer-Verlag, Berlin/Heidelberg, 2005), pp. 57–108.

242. Hoinkis, N., Schuhmacher, J., Fuchs, T., Leukel, S., Loho, C., Roters, A., Richter, F. H. & Janek, J. Amorphous Phase Induced Lithium Dendrite Suppression in Glass-Ceramic Garnet-Type Solid Electrolytes. *ACS Applied Materials & Interfaces* **15,** 28692–28704; 10.1021/acsami.3c01667 (2023).

243. Touidjine, K., Finsterbusch-Rosen, M., Kiyek, V., Ganapathy, S., Finsterbusch, M., Guillon, O., Huijben, M., Kelder, E., Wagemaker, M. & Fattakhova-Rohlfing, D. The impact of lithium carbonate on tape cast LLZO battery separators: a balanced interplay between lithium loss and relithiation. *Energy Storage Materials,* 103487; 10.1016/j.ensm.2024.103487 (2024).

244. Mann, M., Küpers, M., Häuschen, G., Finsterbusch, M., Fattakhova-Rohlfing, D. & Guillon, O. The influence of hafnium impurities on the electrochemical performance of tantalum substituted Li7La3Zr2O12 solid electrolytes. *Ionics* **28,** 53–62; 10.1007/s11581-021-04300-w (2022).

245. Tietz, F., Wegener, T., Gerhards, M. T., Giarola, M. & Mariotto, G. Synthesis and Raman micro-spectroscopy investigation of Li7La3Zr2O12. *Solid State Ionics* **230,** 77–82; 10.1016/j.ssi.2012.10.021 (2013).

246. Gupta, R., Saha, S., Tomar, M., Sachdev, V. K. & Gupta, V. Effect of manganese doping on conduction in olivine LiFePO4. *Journal of Materials Science: Materials in Electronics* **28,** 5192–5199; 10.1007/s10854-016-6175-9 (2017).

247. Frost, R. L., Martens, W., Williams, P. A. & Kloprogge, J. T. Raman and infrared spectroscopic study of the vivianite-group phosphates vivianite, baricite and bobierrite. *Mineralogical Magazine* **66,** 1063–1073; 10.1180/0026461026660077 (2002).

248. Uhlenbruck, S., Dellen, C., Möller, S., Lobe, S., Tsai, C.-L., Finsterbusch, M., Bram, M. & Guillon, O. Reactions of garnet-based solid-state lithium electrolytes with water — A depth-resolved study. *Solid State Ionics* **320,** 259–265; 10.1016/j.ssi.2018.03.004 (2018).

249. Thompson, T., Wolfenstine, J., Allen, J. L., Johannes, M., Huq, A., David, I. N. & Sakamoto, J. Tetragonal vs. cubic phase stability in Al – free Ta doped Li 7 La 3 Zr 2 O 12 (LLZO). *Journal of Materials Chemistry A* **2,** 13431–13436; 10.1039/C4TA02099E (2014).

250. Gross, T. & Hess, C. Raman diagnostics of LiCoO2 electrodes for lithium-ion batteries. *Journal of Power Sources* **256,** 220–225; 10.1016/j.jpowsour.2014.01.084 (2014).

251. Freitas, B., Siqueira Jr., J., Da Costa, L., Ferreira, G. & Resende, J. Synthesis and Characterization of LiCoO2 from Different Precursors by Sol-Gel Method. *Journal of the Brazilian Chemical Society*; 10.21577/0103-5053.20170077 (2017).

252. Nishi, T., Nakai, H. & Kita, A. Visualization of the State-of-Charge Distribution in a LiCoO 2 Cathode by In Situ Raman Imaging. *Journal of The Electrochemical Society* **160,** A1785-A1788; 10.1149/2.061310jes (2013).

253. Ohta, S., Kobayashi, T., Seki, J. & Asaoka, T. Electrochemical performance of an all-solid-state lithium ion battery with garnet-type oxide electrolyte. *Journal of Power Sources* **202,** 332–335; 10.1016/j.jpowsour.2011.10.064 (2012).

254. Wan, J., Xie, J., Kong, X., Liu, Z., Liu, K., Shi, F., Pei, A., Chen, H., Chen, W., Chen, J., Zhang, X., Zong, L., Wang, J., Chen, L.-Q., Qin, J. & Cui, Y. Ultrathin, flexible, solid polymer composite electrolyte enabled with aligned nanoporous host for lithium batteries. *Nature nanotechnology* **14,** 705–711; 10.1038/s41565-019-0465-3 (2019).

255. Dominko, R., Gaberscek, M., Drofenik, J., Bele, M., Pejovnik, S. & Jamnik, J. The role of carbon black distribution in cathodes for Li ion batteries. *Journal of Power Sources* **119-121,** 770–773; 10.1016/S0378-7753(03)00250-7 (2003).

256. Barai, P., Rojas, T., Narayanan, B., Ngo, A. T., Curtiss, L. A. & Srinivasan, V. Investigation of Delamination-Induced Performance Decay at the Cathode/LLZO Interface. *Chemistry of Materials* **33,** 5527–5541; 10.1021/acs.chemmater.0c04656 (2021).

257. Clausnitzer, M., Ihrig, M., Cressa, L., Hein, S., Finsterbusch, M., Eswara, S., Kuo, L.-Y., Danner, T., Kaghazchi, P., Fattakhova-Rohlfing, D., Guillon, O. & Latz, A. Impact of degradation mechanisms at the cathode/electrolyte interface of garnet-based all-solid-state batteries. *Energy Storage Materials* **67,** 103262; 10.1016/j.ensm.2024.103262 (2024).

258. Scheld, W. S., Hoff, L. C., Vedder, C., Stollenwerk, J., Grüner, D., Rosen, M., Lobe, S., Ihrig, M., Seok, A.-R., Finsterbusch, M., Uhlenbruck, S., Guillon, O. & Fattakhova–Rohlfing, D. Enabling metal substrates for garnet-based composite cathodes by laser sintering. *Applied Energy* **345,** 121335; 10.1016/j.apenergy.2023.121335 (2023).

259. Birkner, N., Li, C., Estes, S. L. & Brinkman, K. S. Gallium-Doping Effects on Structure, Lithium-Conduction, and Thermochemical Stability of Li7-3x Gax La3 Zr2 O12 Garnet-Type Electrolytes. *ChemSusChem* **14,** 2621–2630; 10.1002/cssc.202100526 (2021).

260. Tsai, C., Thuy Tran, N. T., Schierholz, R., Liu, Z., Windmüller, A., Lin, C.-A., Xu, Q., Lu, X., Yu, S., Tempel, H., Kungl, H., Lin, S. & Eichel, R.-A. Instability of Ga-substituted Li 7 La 3 Zr 2 O 12 toward metallic Li. *Journal of Materials Chemistry A* **10,** 10998–11009; 10.1039/D1TA10215J (2022).

261. Schwab, C., Häuschen, G., Mann, M., Roitzheim, C., Guillon, O., Fattakhova-Rohlfing, D. & Finsterbusch, M. Towards economic processing of high performance garnets – case study on zero Li excess Ga-substituted LLZO. *Journal of Materials Chemistry A* **11,** 5670–5680; 10.1039/D2TA09250F (2023).

262. Zhang, H., Okur, F., Cancellieri, C., Jeurgens, L. P. H., Parrilli, A., Karabay, D. T., Nesvadba, M., Hwang, S., Neels, A., Kovalenko, M. V. & Kravchyk, K. V. Bilayer Dense-Porous Li7 La3 Zr2 O12 Membranes for High-Performance Li-Garnet Solid-State Batteries. *Advanced science (Weinheim, Baden-Wurttemberg, Germany)* **10,** e2205821; 10.1002/advs.202205821 (2023).

263. Parascos, K., Watts, J. L., Alarco, J. A. & Talbot, P. C. Fabrication of Li7La3Zr2O12 films with controlled porosity and fast Li+ transport. *Journal of Energy Storage* **92,** 111996; 10.1016/j.est.2024.111996 (2024).

264. Dollimore, D. & Tinsley, D. The thermal decomposition of oxalates. Part XII. The thermal decomposition of lithium oxalate. *Journal of the Chemical Society A: Inorganic, Physical, Theoretical,* 3043; 10.1039/J19710003043 (1971).

Acknowledgements

First of all, I would like to thank RWTH Aachen University and Forschungszentrum Jülich for giving me the opportunity to work on my Ph.D. at these institutions. I would also like to thank the S2taR project for funding my work. I would like to thank my professor and 'Doktorvater' and head of the institute, Prof. Dr.-Ing. Olivier Guillon, for his support and feedback, especially during the cases of memorizing old papers where someone had already solved similar sintering problems. Furthermore, I would like to thank Prof. Dr. Jesus Gonzalez-Julian for being my second examiner, as well as Prof. Dr. rer. nat. Robert Spatschek as exam chairman.

I am also grateful to Dr. Martin Finsterbusch, as my scientific advisor, for his guidance in daily laboratory work, taking care of problems in the laboratory, supervising and correcting a lot of written work, including manuscripts, abstracts, project reports and work reports. I would also like to thank Prof. Dr. Dina Fattakhova-Rohlfing for supervising and correcting the work reports and for teaching me how to write a manuscript.

I am also grateful to several other people who have been involved in my work and I would like to thank them for their support. I would like to thank Adrian Lindner for µCT measurements, Andrea Hilgers for PSD measurements, Dr. Jürgen Gross for SEM measurements, Dr. Doris Sebold for SEM, EDX and EBSD measurements, Michael Xhonneux for help with metallography, Dr. Christian Schwab for SIMS measurements, Dr. Yoo Jung Sohn for the XRD measurements and Rietveld analysis, Volker Bader and Philipp Hecker for putting my samples in the oven each time, Grit Häuschen, Tobias Lammert and Kevin Walther for their synthesis of LLZO and Ralf Kauert for his support and sharing his knowledge of the tape casting process.

I have had the pleasure of working with so many of my colleagues, too many to name here, but I am grateful for every floor discussion, every office discussion, every coffee break with and without discussion, our various outside activities, our strategic planning, our lunch breaks, our making and pasting of every mountain and wave to come, the tea, the office conversations, and everyone who answered every question I had, and finally your moral support in every situation and throughout my time here.

Finally, I would be remiss if I did not mention my friends and family, especially my parents and sister, who have made this long journey possible. My biggest thanks and gratitude goes to my partner, without you I would never have started a PhD again, I would not have made it the whole way and I am very grateful for your daily support and believing in every night session I had to master during my thesis. Your belief in me kept me strong so that I could succeed.

The presented work has been edited grammatically with the software DeepL Write (Cologne, Germany).

List of Tables

List of Figures

Publications

Journal Articles

Kiyek, V.; Schwab, C.; Scheld, W. S.; Roitzheim, C.; Lindner, A.; Menesklou, W.; Finsterbusch, M.; Fattakhova-Rohlfing, D.; Guillon, O.: Direct precursor route for the fabrication of LLZO composite cathodes for solid-state batteries, *Advanced Science*, **11** (42), 2404682 (2024). https://doi.org/10.1002/advs.202404682

Kiyek, V.; Hilger, M.; Rosen, M.; Gross, J. P.; Mann, M.; Fattakhova-Rohlfi ng, D.; Schwaiger, R.; Finsterbusch, M.; Guillon, O.: Waste minimization in all-solid-state battery production via re-lithiation of the garnet solid electrolyte LLZO, *Journal of Power Sources* **609**, 234709 (2024). https://doi.org/10.1016/j.jpowsour.2024.234709

Yao, K.; Scheld, W. S.; Ma, Q.; Zeng, Y.; Ganapathy, S.; Ye, R.; Meng, M.; **Kiyek, V.**; Guillon, O.; Huijben, M.; ten Elshof, J. E.; Finsterbusch, M.; Fattakhova-Rohlfi ng, D.: Holistic View on Cation Interdiff usion during Processing and Operaion of Garnet All-Solid-State Batteries, *Energy Storage Materials*, **71**, 103662 (2024).
https://doi.org/10.1016/j.ensm.2024.103662

Touidjine, K.; Finsterbusch-Rosen, M.; **Kiyek, V.;** Ganapathy, S.; Finsterbusch, M.; Guillon, O.; Huijben, M.; Kelder, E.; Wagemaker, M.; Fattakhova-Rohlfi ng, D.: The impact of lithium carbonate on tape cast LLZO battery separators: a balanced interplay between lithium loss and relithiation, *Energy Storage Materials*, **71**, 103487 (2024).
https://doi.org/10.1016/j.ensm.2024.103487

Schneider, K.; **Kiyek, V.**; Finsterbusch, M.; Yagmurlu, B.; Goldmann, D.: Acid Leaching of Al- and Ta-Substituted Li7La3Zr2O12 (LLZO) Solid Electrolyte, *Metals*, **13** (5), 834 (2023).
https://doi.org/10.3390/met13050834

Conference Contributions

Kiyek, V., Schwab, C., Finsterbusch, M., Fattakhova-Rohlfing, D., Guillon, O., A new, energy-saving precursor route for synthesizing Li7La3Zr2O12 & LiCoO2 mixed cathodes for solid-state batteries, *48th International Conference and Expo on Advanced Ceramic and Composites (ICACC2024)*,(2024)

Kiyek, V., Hilger, M., Rosen, M., Häuschen, G., Fattakhova-Rohlfing, D., Finsterbusch, M., Guillon, O., Relithiation of aged LI6.4La3Zr1.6Ta0.4O12 LLZO for All-Solid-State Battery separators, *21st International Meeting on Lithium Batteries (IMLB22)*, online (2022)

Band / Volume 642
Development of Iridium-based Nanostructures for Oxygen Evolution Reaction in PEM Water Electrolysis
S. Park (2024), 135 pp
ISBN: 978-3-95806-779-0

Band / Volume 643
Multi-dimensional GPR full-waveform inversion for small-scale hydrogeophysical soil characterization
D. Hoven (2024), IX, 163 pp
ISBN: 978-3-95806-781-3

Band / Volume 644
Analyse des Gastransports in komplexen Membransystemen durch Modellierung und multiskalige Simulation
K. Wilkner (2024), VIII, 122 pp
ISBN: 978-3-95806-784-4

Band / Volume 645
Deployment of Fuel Cell Vehicles in Road Transport and the Expansion of the Hydrogen Refueling Station Network: 2024 Update
T. Grube; M. Rex (2024), iii, 26 pp
ISBN: 978-3-95806-786-8

Band / Volume 646
Modellgestützte Analyse treibhausgasneutraler Transformationsstrategien für Deutschland
T. F. Schöb (2024), XII, 228 pp
ISBN: 978-3-95806-789-9

Band / Volume 647
Future Distribution Grids Using Geo-Referenced Synthetic Network Topologies
A. Bandam (2024), ix, 237 pp
ISBN: 978-3-95806-790-5

Band / Volume 648
Multi-scenario, high-resolution Lagrangian transport modeling for the analysis of the Asian tropopause aerosol layer
J. H. Clemens (2024), 143 pp
ISBN: 978-3-95806-792-9

Band / Volume 649
Prospektive Lebenszyklusanalysen von Power-to-Gas-Optionen
J. C. Koj (2024), XVIII, 197 pp
ISBN: 978-3-95806-794-3

Band / Volume 650
Assimilation of groundwater level and cosmic-ray neutron sensor soil moisture measurements into integrated terrestrial system models for better predictions
F. Li (2024), xvii, 172 pp
ISBN: 978-3-95806-796-7

Band / Volume 651
Integration of a rib-channel design to improve air-side contacting in solid oxide cell (SOC) stacks
Y. S. Ayhan (2024), 82 pp
ISBN: 978-3-95806-797-4

Band / Volume 652
Modelling Secondary Circulation in Convective Boundary Layer Using Large Eddy Simulation
L. Zhang (2024), 84 pp
ISBN: 978-3-95806-799-8

Band / Volume 653
Optionen zur Umsetzung der Klimaschutzziele im Verkehrssektor
S. Kraus (2025), XI, 317 pp
ISBN: 978-3-95806-802-5

Band / Volume 654
Modellierung der flächendifferenzierten Grundwasserneubildung für Schleswig-Holstein im Beobachtungszeitraum 1961 – 2021 und für Klimaszenarien bis 2100
I. McNamara, B. Tetzlaff, F. Wendland, T. Wolters (2025), 191 pp
ISBN: 978-3-95806-803-2

Band / Volume 655
Entwicklung alternativer Brenngaselektroden für die Hochtemperatur-Elektrolyse
F. E. Winterhalder (2025), vii, 161 pp
ISBN: 978-3-95806-805-6

Band / Volume 656
Oxide-based All-Solid-State Batteries for and from Recycling Processes
V. M. Kiyek (2025), viii, 128 pp, xix
ISBN: 978-3-95806-806-3

Weitere ***Schriften des Verlags im Forschungszentrum Jülich*** unter
http://wwwzb1.fz-juelich.de/verlagextern1/index.asp

Energie & Umwelt / Energy & Environment
Band / Volume 656
ISBN 978-3-95806-806-3

Mitglied der Helmholtz-Gemeinschaft

JÜLICH
Forschungszentrum